All Theses and Dissertations (ETDs)

Winter 1-1-2012

Foot Deformity and Bone Strength in Charcot Neuropathic Osteoarthropathy

David Joseph Gutekunst
Washington University in St. Louis

Follow this and additional works at: https://openscholarship.wustl.edu/etd

Recommended Citation

Gutekunst, David Joseph, "Foot Deformity and Bone Strength in Charcot Neuropathic Osteoarthropathy" (2012). *All Theses and Dissertations (ETDs)*. 1005.
https://openscholarship.wustl.edu/etd/1005

WASHINGTON UNIVERSITY IN ST. LOUIS

Program in Movement Science

Dissertation Examination Committee:

David R. Sinacore, Chair
Guy M. Genin
Michael J. Mueller
Matthew J. Silva
Michael J. Strube
Dequan Zou

Foot Deformity and Bone Strength in Charcot Neuropathic Osteoarthropathy

by

David Joseph Gutekunst

A dissertation presented to the
Graduate School of Arts and Sciences
of Washington University in
partial fulfillment of the
requirements for the degree
of Doctor of Philosophy

December 2012

St. Louis, Missouri

TABLE OF CONTENTS

LIST OF FIGURES

LIST OF TABLES

ABBREVIATIONS

DM	diabetes mellitus
PN	peripheral neuropathy
CN	Charcot neuropathic osteoarthropathy
BMD	bone mineral density
vQCT	volumetric quantitative computed tomography
SF	stress fracture
DXA	dual-energy X-ray absorptiometry
QUS	quantitative ultrasound
Met2	second metatarsal
Met3	third metatarsal
Met5	fifth metatarsal
HU	Hounsfield unit
HA	hydroxyapatite
HR-pQCT	high-resolution peripheral quantitative computed tomography
Ct.Th	average cortical thickness
BR	buckling ratio
Tt.Ar	total cross-sectional area
Ct.Ar	cortical cross-sectional area
I	moment of inertia
I_{min}	minimum moment of inertia
S	section modulus
S_{min}	minimum section modulus
μCT	micro-computed tomography

ACKNOWLEDGMENTS

I express my deepest thanks and appreciation to the following individuals and groups:

For Sarah: skilled editor, thoughtful partner, and my best friend

CHAPTER 1

Introduction

1.1 Overview: Lower-extremity complications of diabetes mellitus

Diabetes mellitus (DM) is a major health issue worldwide, with more than 346 million people affected based on recent estimates by the World Health Organization (World Health Organization, 2011). In the U.S., there were 25.8 million people with diabetes in 2011, with an estimated 1.9 million new cases every year in people 20 years and older (Centers for Disease Control, 2011). More than 60% of non-traumatic lower-limb amputations that are performed in the U.S. occur in individuals with diabetes, which amounted to more than 65,000 non-traumatic lower-limb amputations in 2006 (Centers for Disease Control, 2011). Lower-limb amputation in individuals with diabetes is strongly related to the development and progression of diabetic foot disease, a group of related lower-extremity conditions that includes peripheral neuropathy (PN), plantar ulceration, and Charcot neuropathic osteoarthropathy (CN).

1.2 Charcot neuropathic osteoarthropathy

Acute CN is suspected when an individual with DM and PN presents clinically with a warm, inflamed, erythematous foot (Chantelau, 2005). Existence of CN is generally confirmed by X-ray evidence of pedal bone fracture or pronounced joint subluxation or dislocation. Unfortunately, plain radiographs are often unable to detect incipient Charcot development due to difficulty visualizing the injured bony region or subtle articular mal-alignment (Yu and Hudson, 2002). As a result, progression of CN often continues until more serious events occur.

Mal-alignment and degradation of the bony components of a denervated, inflamed joint are the hallmark symptoms of CN (Frykberg and Belczyk, 2008). Though CN has been found in a variety of patient populations – e.g. leprosy, syphilis, multiple sclerosis, poliomyelitis, and rheumatoid arthritis – DM with concomitant PN is the most common cause of CN (Sanders and Fryberg, 2005). The incidence of CN has been reported to be as low as 1 in 680 diabetic patients (Sinha *et al.*, 1972) though CN occurs eventually in up to 29% of diabetics with PN (Cofield *et al.*, 1983).

Individuals with DM and PN have an elevated risk of plantar ulceration due to a distal polyneuropathy that includes an absence of protective sensation (Rogers *et al.*, 2011). In a sensate individual, pain and inflammation would typically lead to a self-reduction in weight-bearing activity, but an individual with DM and PN can cause plantar soft tissue damage due to continued repetitive loading (Sinacore *et al.*, 2008). Still, whether or not an individual develops the superficial skin and soft tissue breakdown characteristic of plantar ulceration, the combined effects of DM and PN – sensory and motor neural decrements, atrophied pedal musculature, ligament laxity, and pedal bone degradation – can lead to the types of joint subluxation, dislocation, and pedal bone fractures that characterize CN (Crews and Wrobel, 2008). These CN symptoms, in turn, can put the diabetic neuropathic patient at further risk for ulceration and more serious sequelae of diabetic foot disease, including infection and amputation (Wukich and Sung, 2009; Wukich *et al.*, 2011).

1.3   Bone degradation in CN

Herbst and colleagues (Herbst *et al.*, 2004) hypothesized that the clinical manifestation of CN depends upon bone mineral density (BMD): pedal fractures predominate in individuals with low BMD, whereas pedal bone subluxations and dislocations are more common in those with normal or high BMD. The authors prospectively assessed 55 consecutive individuals with DM and a newly-diagnosed CN of the foot or ankle. Of the 55 patients, there was an equal representation of fractures and subluxations/dislocations: 23 had fractures, 23 had subluxations/dislocations, and 9 had both. The contralateral (non-CN) femoral neck was scanned using dual-energy X-ray absorptiometry (DXA) to assess BMD, and the results showed an odds ratio of 9.5 for having a fracture rather than subluxation/dislocation among individuals with BMD levels classified as osteopenic by World Health Organization standards.

However, it is possible that pedal bone BMD could be dissociated from femoral neck BMD in the distal polyneuropathy common in individuals with DM and PN, and thus it would be useful to determine whether pedal BMD and strength-related geometric properties are reduced in those with a fracture pattern of CN. Evidence of focal reductions in pedal BMD following CN diagnosis and subsequent off-loading has been shown recently (Sinacore *et al.*, 2008). The authors sought to assess the relationship between acute inflammation and tarsal BMD. Thirty-two individuals with DM, PN, and CN and 64 age-, sex-, and race-matched controls were assessed by measuring foot temperatures at 7 plantar locations and calcaneal BMD via quantitative ultrasound (QUS). The amount of focal inflammation – assessed as the temperature difference between feet – mirrored reductions in calcaneal BMD as measured by QUS. The involved

feet of the DM+PN+CN subjects were warmer than the uninvolved feet (average

difference 3.8 °C) while the control subjects had no temperature difference. Calcaneal

BMD averaged 384, 467, and 545 mg/cm^2, respectively for the involved, uninvolved, and

control feet. Thus, the inflammation seen in CN is associated with a focal reduction in

pedal BMD, though the observed reduction in BMD for the uninvolved foot makes it

unclear whether the focal bone loss is the cause or effect of the incipient CN (Sinacore *et

al.*, 2008).

1.4   *Image-based bone strength indices*

Recent advances have provided a means to measure BMD of individual bones of

the foot using volumetric quantitative computed tomography (vQCT) rather than less

precise methods such as QUS or DXA (Commean *et al.*, 2009; Hastings *et al.*, 2008).

Commean et al (Commean *et al.*, 2009) used a semiautomatic bone segmentation

technique to separate the 7 tarsals and 5 metatarsals from each other and from the

surrounding soft tissue before computing whole-bone and subregional bone volumes and

BMD. Results showed high reproducibility and low measurement error, with root-mean

square coefficients of variation (RMS-CV) equal to 0.8% and 0.9% for whole-bone

volume and BMD, respectively. Hastings et al. (Hastings *et al.*, 2008) applied this vQCT-

based BMD assessment to a case study of a young healthy female recovering from an

ankle injury and showed that marked increases in bone-specific BMD were related to

locations of higher peak pressures during gait. Thus the vQCT-based BMD measures are

not only reproducible, but also responsive to changes in loading pattern.

Though the ability to assess BMD of individual foot bones is a significant advancement, the role of BMD as a prospective risk factor for acute or overuse-related fracture is unclear. Numerous studies suggest that a reduction in BMD alone may not lead to an increased risk of fracture, and that strength-related bone geometric properties provide an improved index of fracture risk (Brudvig *et al.*, 1983; Pester and Smith, 1992; Evans *et al.*, 2008; Warden *et al.*, 2005; Silva *et al.*, 2009). For example, while female military recruits have a 2 to 6 times higher risk of developing a tibial stress fracture (SF) than males (Brudvig *et al.*, 1983; Pester and Smith, 1992) a recent study comparing bone strength parameters showed that females had 2.0% to 2.7% *higher* cortical BMD in the tibia than males (Evans *et al.*, 2008). The higher SF incidence can be explained by females' significantly lower values for cross-sectional diameter, area, and cross-sectional second moment of area (Evans *et al.*, 2008). Cross-sectional moment of area, a measure of the distribution of a bone's mass around its centroid, is an index of structural rigidity, especially for loading that involves bending moments, as evidenced by rodent studies linking minimum cross-sectional moment of area to fracture strength (Warden *et al.*, 2005; Silva *et al.*, 2009).

Bone geometric parameters have also been related to tibial SF in male runners and military recruits. In a study matching 23 male runners with prior tibial SF to 23 non-SF matched controls, tibial cross-sectional area measured using either vQCT or DXA was significantly lower in the SF cohort than in the non-SF group after adjusting for height and weight (Crossley *et al.*, 1999). These results support earlier findings using tibial X-rays (Milgrom *et al.*, 1989) and DXA scans (Beck *et al.*, 1996). Milgrom et al (Milgrom *et al.*, 1989) computed cross-sectional bone-width, area, and second moment of area (the

binary analog of mass moment of inertia) based on X-ray scans of the tibial mid-diaphysis of 295 Israeli infantry recruits. Recruits who developed tibial SF had significantly narrower tibias (corroborating earlier findings by Giladi et al (Giladi *et al.*, 1987)), lower cross-sectional area, and lower second moment of area. The moment of area around an anterior-posterior axis had the greatest predictive capacity for development of tibial SF. This high predictive capacity is possibly explained by the fact that for the human tibia, the anterior-posterior axis is roughly collinear with both the minimum second moment of area and the axis of greatest bending during compressive loading. In rodent studies, the minimum cross-sectional moment of area has been shown to have the highest predictive capacity for both monotonic fracture force (Silva *et al.*, 2009; Robling *et al.*, 2002; Turner and Robling, 2003) and resistance to fatigue fracture (Warden *et al.*, 2005; Silva *et al.*, 2009).

Cadaver specimens have been used to assess geometric properties of individual pedal bones (Largey *et al.*, 2007) and bone orientation angles (Camacho *et al.*, 2002). Largey et al (Largey *et al.*, 2007) performed individual high-resolution vQCT scans on excised metatarsals from 7 cadaver specimens, with the scan slice plane perpendicular to the longitudinal axis of each metatarsal. The authors used the resulting stack of planar vQCT images to measure bone lengths, cross-sectional diameter, intrinsic bone torsion, and cross-sectional area in the proximal, mid-diaphysis, and distal regions of each bone. For comparison, bone dimensions and torsion angles were also assessed manually. While the in vitro nature of the vQCT scans prevented assessment of the bone-to-bone orientation angles, and the authors elected to not measure some relevant strength-related geometric properties (such as MOI), the authors did report high ICC values ($\geq$0.98) for

their vQCT-derived measures, exceeding the ICC values for all of their manual measures (Largey *et al.*, 2007). These high ICC values suggest utility as a research and clinical tool for vQCT-derived measures of pedal bone dimensions.

1.5   *Radiographic measures of foot deformity*

Computed tomography scans have been used increasingly to measure foot morphology. Non-weight bearing CT scans have shown that diabetic subjects exhibit hyperextension at the first, second, and third metatarso-phalangeal joints, defined clinically as hammer toe deformity (Robertson *et al.*, 2002). In a related study, Mueller et al (Mueller *et al.*, 2003) showed that hammer toe deformity had the highest predictive capacity for peak plantar pressures under the metatarsal heads. Thus, not only is CT capable of providing important morphological information about the bones of the diabetic foot, but altered joint orientations are related to known biomechanical risk factors (such as hammer toe deformity) for soft tissue damage leading to plantar ulceration. However, one weakness of these studies is that both relied on planar representations of CT data in order to make the joint angle calculations. The measurement of three-dimensional (3D) bone-to-bone orientation angles will provide a more complete and accurate assessment of foot morphology in diabetic subjects.

Camacho et al (Camacho *et al.*, 2002) described an assessment of selected bone-to-bone orientation angles using a 3D reconstruction of a single human cadaver foot. Each tarsal and metatarsal was segmented from the raw CT images, and the principal axes of each bone were calculated using PCA. Bone-to-bone orientation angles were defined using Euler rotation sequences of the principal axes for bones of interest

(Camacho *et al.*, 2002). Following on the work of Camacho et al, Ledoux et al (Ledoux *et al.*, 2006) conducted 3D CT scans on 65 live subjects in order to compare pedal orientation angles to each subject's clinical foot type classification (e.g. pes planus, neutral, or pes cavus). The authors utilized Cardan angles to define 24 bone-to-bone orientation angles for the 65 feet, then conducted a classification tree analysis to determine orientation angles that best discriminated among the foot type classifications (Ledoux *et al.*, 2006).

In summary, vQCT provides a means to detect early signs of CN before fracture, bone resorption, or subluxation is evident on X-ray. Earlier diagnosis of CN will facilitate appropriate off-loading strategies to minimize fracture risk, bony degradation, and joint deformity that would otherwise lead to significant morbidity and risk of further diabetic foot disease sequelae.

1.6   *Specific Aims, Hypotheses, and Rationale*

The goal of this dissertation research is to use vQCT to assess foot bone strength and foot deformity as indices of CN development and progression. Aim 1 relates to method development and validation of BMD and geometric bone strength indices for the metatarsals. Aim 2 provides group comparisons of vQCT-derived bone strength indices between CN and non-CN individuals. Aim 3 presents method development and reliability assessment of novel 3D methods to assess foot deformities. Aim 4 is a comparison of vQCT-derived foot deformity measures in CN and non-CN individuals.

SPECIFIC AIM 1:

To assess the ability of vQCT-derived BMD and bone geometric strength indices to predict *ex vivo* ultimate loads in metatarsals excised from cadavers using maximal monotonic three-point loading in materials-testing apparatus.

AIM 1 HYPOTHESES:

.BMD and geometric strength indices will be directly and significantly correlated to ultimate loads, and geometric strength indices will be retained in the final regression model predicting ultimate force.

SPECIFIC AIM 2:

To compare vQCT-derived geometric strength indices of subjects with diabetes mellitus (DM), peripheral neuropathy (PN), and Charcot neuropathic osteoarthropathy (CN) to subjects with DM and PN but without CN.

AIM 2 HYPOTHESES:

For the metatarsals, individuals with CN will exhibit reduced BMD and lower values for geometric strength indices in the mid-diaphysis in the involved foot compared to the uninvolved foot and compared to individuals with DM+PN.

SPECIFIC AIM 3:

To develop an anatomic landmark-based method of defining 3D bone orientation axes for foot bones using segmented vQCT surface images, and to assess intra-tester and inter-tester reliability for 3D bone-to-bone orientation angle.

AIM 3 HYPOTHESES:

An anatomic landmark-based method to define 3D foot bone orientation axes will have equivalent intra- and inter-tester reliability as uni-planar measures from X-ray.

SPECIFIC AIM 4:

To use the atlas-based, automated vQCT methods to characterize 3D bone and joint mal-alignments in subjects with acute CN compared to two control cohorts: a matched group of non-CN individuals with DM and PN, and an unimpaired control (UC) group without DM, PN, CN, or pathology of the foot and ankle.

AIM 4 HYPOTHESES:

(1) Atlas-based, automated vQCT technique will confirm mal-alignments observed in CN using uni-planar (lateral) X-rays. Specifically, sagittal plane bone orientation angles of CN subjects will have decreased cuboid height, decreased calcaneal pitch, and increased talar declination angle.

(2) There will be additional group differences in hindfoot bones and hindfoot:forefoot coupling, including frontal plane mal-alignments undetectable using X-rays.

Predicting *ex vivo* failure loads in human metatarsals using bone strength indices derived from volumetric quantitative computed tomography

Status of resulting manuscript: in review, *Journal of Biomechanics*

Authors: David J. Gutekunst, Tarpit K. Patel, Kirk E. Smith, Paul K. Commean, Matthew J. Silva, and David R. Sinacore.

2.1   ABSTRACT

The purpose of this study was to investigate whether bone mineral density and bone geometric strength indices predict ultimate force in the human second metatarsal (Met2) and third metatarsal (Met3). Intact lower extremity cadaver samples were measured using clinical vQCT with positioning and parameters applicable to *in vivo* scanning. During processing, raw voxel data (0.4mm isotropic voxels) were converted from Hounsfield units (HU) to apparent BMD using hydroxyapatite (HA) calibration phantoms to allow direct volumetric assessment of whole-bone and subregional metatarsal BMD. Voxel data were realigned to produce cross-sectional slices perpendicular to the longitudinal axes of the metatarsals. Average mid-diaphyseal BMD, bone thickness, and buckling ratio were measured using an optimized threshold to distinguish bone from non-bone material. Minimum and maximum moments of inertia and section moduli were measured in the mid-diaphysis region using both a binary threshold for areal, unit-density measures and a novel technique for density-weighted measures.

BMD and geometric strength indices were strongly correlated to ultimate force measured by *ex vivo* 3-point bending. Geometric indices were more highly correlated to ultimate force than was BMD; bone thickness and density-weighted minimum section modulus had the highest individual correlations to ultimate force. Density-weighted geometric indices explained more variance than their binary analogs. Multiple regression analyses defined models that predicted 83-89% of variance in ultimate force in Met2 and Met3 using bone thickness and minimum section modulus in the mid-diaphysis. These

results have implications for future *in vivo* imaging to non-invasively assess bone strength and metatarsal fracture risk.

2.2 INTRODUCTION

The metatarsals are a frequent site of foot fracture, particularly stress fractures (SF) occurring without an acute traumatic event. In athletes, roughly 20% of SF occur in the metatarsals, with the majority (14-18%) occurring in either Met2 or Met3 (Hulkko and Orava, 1987; McBryde, Jr., 1985). Additionally, diabetes mellitus with concomitant peripheral neuropathy has been linked to focal osteopenia in the feet and an increased risk of metatarsal fracture (Cundy *et al.*, 1985; Gill *et al.*, 1997) and "silent" bone stress injuries (Chantelau *et al.*, 2007).

BMD in the metatarsal mid-diaphysis correlates with *ex vivo* bone strength measured via mechanical testing (Courtney *et al.*, 1997; Muehleman *et al.*, 2000). Image-based, *in vivo* assessment of BMD is more challenging in the metatarsals than in other long bones (e.g. femur or tibia) due to the smaller size, numerous articulations, and obstructed views of foot bones. As a result, previous investigations of metatarsal BMD and bone dimensions (Courtney *et al.*, 1997; Fleischli *et al.*, 1998; Muehleman *et al.*, 2000) have utilized cadaver bones that were excised before making measurements. Recent work by our group allows *in vivo* measurement of BMD of all foot bones using vQCT (Commean *et al.*, 2009; Hastings *et al.*, 2008; Commean *et al.*, 2011). The vQCT method uses a semiautomatic bone segmentation technique to separate the tarsals and

metatarsals from each other and the surrounding soft tissue to compute whole-bone and subregional bone volumes and BMD (Commean *et al.*, 2009).

Though the ability to assess volumetric BMD of foot bones *in vivo* is a significant technical advancement, the role of BMD as a prospective risk factor for acute or overuse-related pedal fracture is unclear. Research in the tibia and femur suggests a reduction in BMD alone may not lead to increased fracture risk, and that bone geometric strength indices provide an improved index of fracture risk (Brudvig *et al.*, 1983; Evans *et al.*, 2008; Pester and Smith, 1992). For example, while female military recruits have a 2 to 6 times higher risk of developing a tibial SF than males (Pester and Smith, 1992; Brudvig *et al.*, 1983) a recent study showed that females had 2.0% to 2.7% *higher* cortical BMD in the tibia than males (Evans *et al.*, 2008). The disproportionately higher SF incidence despite higher cortical BMD may be explained by females' significantly lower values for indices of compressive and bending strength: cross-sectional diameter, area, and minimum moment of inertia (I_{min}) (Evans *et al.*, 2008).

To offset a general age-related decline in BMD, long bones minimize reductions in bending strength by adding bone material to the periosteal surface while a concomitant, larger expansion of the endosteal surface leads to reductions in cortical thickness (Ct.Th) (Sigurdsson *et al.*, 2006; Ward *et al.*, 2011). This *homeostatic expansion* leaves bones at elevated risk for focal cortical shell weakness and fractures (Beck, 2007; Kaptoge *et al.*, 2008). Both decreased Ct.Th and increased buckling ratio (BR = periosteal radius/Ct.Th) in the femoral neck have been related to an increased risk of hip fracture (LaCroix *et al.*, 2010; Melton, III *et al.*, 2005; Szulc *et al.*, 2006).

The purpose of this study was to develop geometric strength indices as predictors of *ex vivo* failure loads in human Met2 and Met3 samples using techniques directly applicable to *in vivo* clinical imaging by collecting vQCT data from intact cadaver lower-extremity specimens before excising metatarsals and subjecting the bones to failure testing. We hypothesized that BMD and geometric indices would correlate to metatarsal strength, and that geometric strength indices would be retained in stepwise regression models predicting metatarsal strength.

2.3   MATERIALS AND METHODS

Measuring BMD and bone geometric strength indices in the metatarsals using a method applicable to *in vivo* scanning poses unique challenges. Whereas the femur and tibia can easily be aligned axially within an imaging modality such as high resolution peripheral quantitative computed tomography (HR-pQCT) to produce cross-sectional slices, the metatarsals cannot be simultaneously aligned in true axial position within a vQCT scanner. Using excised cadaver metatarsal samples obviates the need for segmentation or axis realignment but limits clinical relevance. Any method capable of assessing bone geometry in human metatarsals *in vivo* requires bone segmentation and realignment of image data along the primary axis of each metatarsal in order to produce anatomically relevant cross-sectional image slices.

2.3.1 Cadaver preparation and vQCT testing

Ten unpaired fresh-frozen cadaver lower limbs were received from the Human Body Donation Program at the Washington University School of Medicine. All samples

were right limbs. After thawing (24-36 hours), limbs were disarticulated at the knee and transported to the Center for Clinical Imaging Research for clinical vQCT scans. Cadaver samples were placed in a radiolucent Styrofoam holding apparatus to ensure consistent positioning. The ankle joint was held in a neutral position (90°) with the foot and shank both 45° above the horizontal (Figure 2.1). This position kept the metatarsals as close to horizontal as possible while allowing clearance of the proximal tibia within the vQCT scanner tube. Additionally, the cadaver positioning closely matches the standard orientation of the lower limb for patients and research subjects at our institution (Commean *et al.*, 2011; Commean *et al.*, 2009). Table height was adjusted so the volume isocenter was approximately at the height of the mid-diaphyseal region of the metatarsals. A QCT Bone Mineral™ HA calibration phantom (Image Analysis Inc., Columbia, KY, USA) was placed in series with each sample at the same height as the scanner isocenter to allow conversion of HU to apparent BMD (mg/cm^3 of HA). (Smith *et al.*, 2011)

Figure 2.1: Position and orientation of lower extremity sample in Styrofoam fixture during vQCT scanning. Hydroxyapatite calibration phantom is shown in front of the foot, at the height of the talus.

Foot images were acquired using a Siemens SOMATOM Definition CT scanner (Siemens Medical Systems, Malvern, PA, USA) with acquisition parameters of 220 mA·s, 120 kVp, pitch = 1, rotation time 0.33s, and a 512x512 matrix. Raw data were reconstructed at 0.4mm slice reconstruction intervals using a B70f kernel to create vQCT images. Prior to reconstruction, the in-plane field of view was cropped to roughly 200mm x 200mm, resulting in an in-plane resolution of approximately 0.4mm x 0.4mm.

2.3.2 Bone Segmentation Processing

Reconstructed vQCT images were loaded in Digital Imaging and Communications in Medicine (DICOM) format into Analyze® software (Biomedical Imaging Resource, Mayo Clinic, Rochester, MN). Image data were interpolated to isotropic voxels with 0.4mm dimension using a cubic spline function. Full details of the

17

bone segmentation process are described elsewhere (Liu *et al.*, 2008; Commean *et al.*, 2011). In brief, bones were segmented from the surrounding soft tissue using density-based filtering algorithms employed as custom ImageJ plugins (NIH Research Services Branch, rsbweb.nih.gov), Analyze® software to further segment bones from soft tissue (e.g. high density tissues such as tendon and ligament), and a custom graph-cut method to segment bones at their articulating surfaces and create volume-filled object maps (Liu *et al.*, 2008) as shown in Figure 2.2. Following segmentation, bone object maps were overlaid on the original grayscale volumetric data so that the Met2 and Met3 voxel datasets could be exported for further analysis.
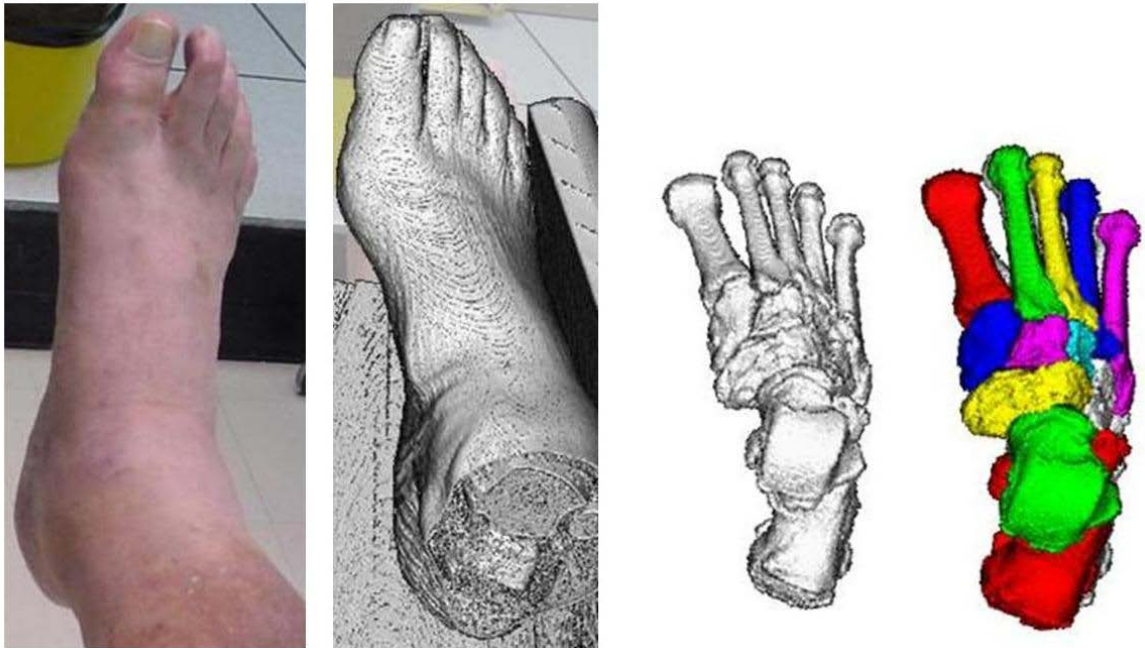
Figure 2.2: Bone segmentation processing. (A) photograph of cadaver sample; (B) raw vQCT image; (C) filtered vQCT image to remove soft tissue; (D) segmented, filled bone object maps for tarsals and metatarsals.

2.3.3 Bone Axis Realignment

Grayscale voxel data for each bone produced during bone segmentation were exported to ImageJ, where the BoneJ plugin (Doube *et al.*, 2010) was used to compute a density-weighted principal components analysis and realign the voxel data perpendicular to each bone's longitudinal axis. This transformation realigned voxel data from the vQCT scanner coordinate axes into anatomically relevant cross-sectional slices perpendicular to each metatarsal's longitudinal axis. Realigned data retained 0.4mm isotropic voxel dimensions. Subsequent calculations of BMD and bone geometric strength indices were completed with BoneJ and custom macros in Excel (Microsoft) using the voxel data (XYZ positions and HU values) from realigned cross-sectional slices.

2.3.4 Bone Geometric Strength Indices

HU values were converted to equivalent BMD using the cadaver-specific HA calibration coefficients. For each realigned slice, total equivalent bone mineral content (mg) was computed as the product of all positive voxel BMD values multiplied by each voxel's volume. Total bone mineral content was then divided by the total volume within the periosteal window, *i.e.* the volume of the positive BMD voxels and the volume of any negative voxels (representing marrow tissue) within the medullary cavity, meaning that the BMD values reported here represent the average BMD over the total tissue volume.

Measuring Ct.Th and BR requires a threshold-based binary definition of bone and non-bone material, and Otsu thresholding (Otsu, 1979) of the 20 metatarsals revealed optimal thresholds between 150 and 300 mg/cm^3. To maintain consistency across specimens and also reduce the likelihood of overestimating bone material by choosing an

erroneously low bone threshold (Hangartner, 2007), a universal threshold of 300 mg/cm^3 was applied to all bones to distinguish between bone and non-bone material. The spatial resolution of vQCT scanning limits the ability to distinguish trabecular and cortical bone material due to spatial averaging. In lieu of measuring Ct.Th directly, average Ct.Th and BR were computed using an assumption that the metatarsal mid-diaphysis is roughly a circular annulus. Total cross-sectional area (Tt.Ar) was computed by summing the entire area (including the medullary cavity) and cortical bone area (Ct.Ar) was computed by summing the area of voxels with BMD $\geq$ 300 mg/cm^3. Ct.Th and BR were then calculated based on the outer (R$_o$) and inner (R$_i$) radii, as follows:

$$Tt.Ar = \pi * R_o^2$$

$$Tt.Ar - Ct.Ar = \pi * R_i^2$$

$$Ct.Th = R_o - R_i$$

$$BR = R_o/Ct.Th$$

Minimum and maximum moments of inertia (I) and section moduli (S) were computed as indices of bending strength using the BoneJ plugin (Doube *et al.*, 2010) in ImageJ. BoneJ computes I and S as areal measures (I$_{Area.min}$, I$_{Area.max}$, S$_{Area.min}$, S$_{Area.max}$) using an assumption of unit density and a threshold-based binary definition of bone and non-bone material, as has been done previously using other analysis software (Courtney *et al.*, 1997; Evans *et al.*, 2008; Muehleman *et al.*, 2000). This binary definition of bone material can be problematic if the threshold is suboptimal (Hangartner, 2007), especially for clinical scanning of small bones such as metatarsals. A density-weighted approach may lessen the effects of limited spatial resolution by improving the density resolution.

Thus, in addition to the standard area-based bending strength indices, we also computed novel density-weighted measures ($I_{\rho.min}$, $I_{\rho.max}$, $S_{\rho.min}$, and $S_{\rho.max}$) using all voxel data exceeding the 300 mg/cm^3 threshold. Computations of the areal and density-weighted measures are provided in Appendix A. It should be noted that the density-weighted measures of I and S require a bone volume rather than a cross-sectional area; to allow future comparison to imaging data with differing voxel thickness, all I and S measures are expressed relative to a 1mm axial thickness.

2.3.5 Bone Fracture Testing

After vQCT scanning, Met2 and Met3 were excised from the cadaver limbs, taking care to avoid damage to the periosteal surface while denuding the bones of surrounding soft tissue. The metatarsals were wrapped in gauze that had been soaked in 0.9% NaCl solution, then stored in 75mL specimen tubes at -20°C until being thawed prior to fracture testing. Samples were loaded monotonically to failure in three-point bending using an Instron 8841 materials testing machine (Instron, Canton, MA, USA). The span length (L) of 33mm was chosen because it was the longest distance that ensured the vertical loading posts would be located within the metatarsal shaft for all bones tested. The central force was applied at the span midpoint on the (inverted) dorsal side of the metatarsal; the two other forces were applied at equal distances from the midpoint on the plantar side of the metatarsal to mimic the predominant loading mode during push-off (Arndt *et al.*, 2002; Donahue and Sharkey, 1999) as shown in Figure 2.3. Fixture posts for 3-point bending were machined to have a rounded tip with 3mm diameter to minimize the effect of local cortical buckling at the fixture sites and thus help ensure that failure would occur due to bending loads rather than local contact stress.
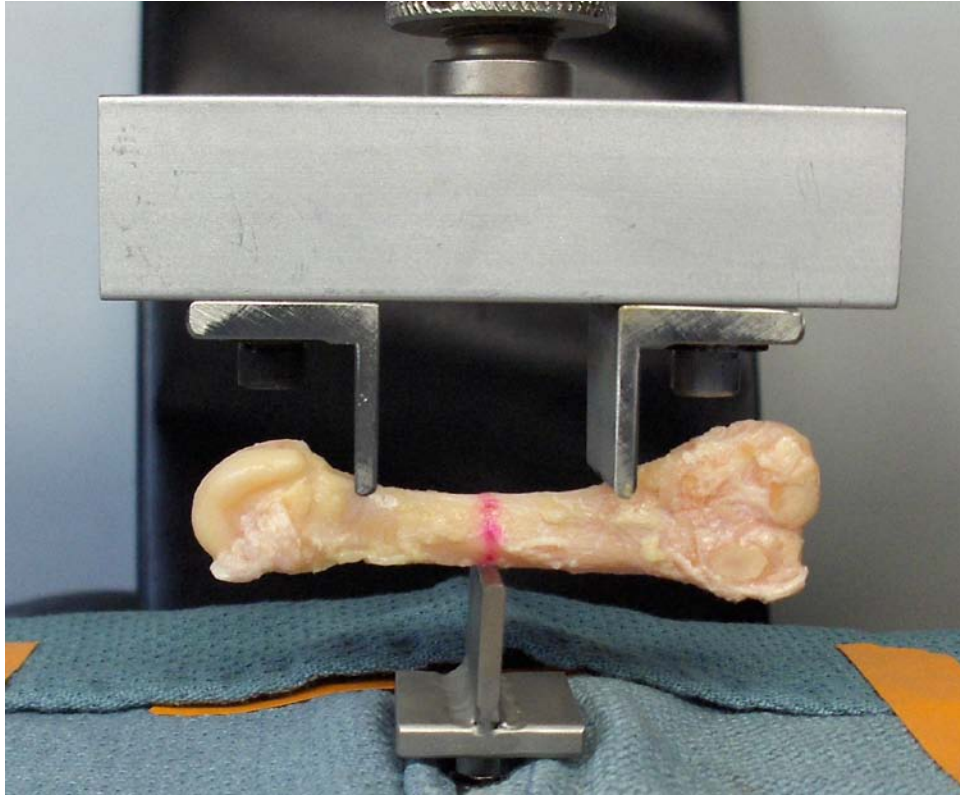
Figure 2.3: Cadaver Met2 sample in 3-point loading configuration. Red line denotes the mid-diaphysis as determined from caliper measurements.

Pre-load was 10N, displacement rate was 0.1 mm/s, and force-displacement data were sampled at 60 Hz. The ultimate force ($\mathbf{F}_{ult}$, in N) was defined as the maximum force registered between the onset of loading and fracture. To allow for comparison to other loading modes (e.g. 4-point bending or cantilever loading) or differing span lengths, we also report the ultimate bending moment ($\mathbf{M}_{ult}$ in N·m), computed using the equation for bending moment in a 3-point configuration with loading at the mid-diaphysis:

$$M_{ult} = \frac{F_{ult} * L}{4}$$

2.3.6 Statistical Analysis

All statistical analyses were completed using IBM SPSS Statistics 20.0 [IBM, Chicago, IL]. A linear regression comparing the $\mathbf{F}_{ult}$ between Met2 and Met3 showed that bones from the same individual were highly correlated. Therefore we report separate regression analyses for Met2 and Met3. Linear regression analyses were performed between $\mathbf{F}_{ult}$ and the independent variables: BMD; Ct.Th; BR; and areal ($I_{Area.min}$, $I_{Area.max}$, $S_{Area.min}$, and $S_{Area.max}$) and density-weighted ($I_{\rho.min}$, $I_{\rho.max}$, $S_{\rho.min}$, and $S_{\rho.max}$) indices of bending strength. Lastly, a stepwise multiple regression analysis ($\alpha \leq 0.05$ for inclusion, $\alpha \geq 0.10$ for removal) was performed to assess the relative roles of potential strength indices in determining $\mathbf{F}_{ult}$.

2.4   RESULTS

Cadaver specimens came from 7 females and 3 males who had an average age of 83 years (SD 13, range 56-99) at death. Table 2.1 shows the average values for ultimate loads, bone quantity, size, and distribution parameters for Met2 and Met3. Univariate correlation coefficients with $\mathbf{F}_{ult}$ are also reported. For both Met2 and Met3, Ct.Th was the highest correlate of $\mathbf{F}_{ult}$, and the density-weighted geometric indices of bending strength accounted for a higher proportion of the variance in $\mathbf{F}_{ult}$ than did the unit density analogs of bending strength.

Table 2.1: Bone quantity, size, and bending strength parameters. R values represent correlation coefficient with ultimate loads (F_{ult} or M_{ult}).

	Units	Met2 Mean ± SD	R	Met3 Mean ± SD	R
Ultimate loads					
F_{ult}	N	572 ± 299	n/a	406 ± 244	n/a
M_{ult}	N*m	4.72 ± 2.47	n/a	3.36 ± 2.01	n/a
Bone quantity parameters					
Whole-bone BMD	mg/cm^3	403 ± 91	0.77	367 ± 91	0.73
Mid-diaphysis BMD	mg/cm^3	806 ± 205	0.71	725 ± 195	0.62
Mid-diaphysis size parameters					
Total Area (Tt.Ar)	mm^2	50.9 ± 11.5	0.46	49.0 ± 9.5	0.71
Buckling Ratio (BR)	unitless	2.29 ± 0.54	-0.80	2.50 ± 0.55	-0.62
Average thickness (Ct.Th)	mm	1.84 ± 0.49	0.92	1.64 ± 0.40	0.83
Areal, unit density bending strength parameters					
$I_{Area.min}$	mm^4	156.7 ± 70.0	0.72	133.6 ± 65.3	0.79
$I_{Area.max}$	mm^4	253.3 ± 143.8	0.40	236.1 ± 92.5	0.70
$S_{Area.min}$	mm^3	39.9 ± 13.9	0.70	35.2 ± 13.2	0.82
$S_{Area.max}$	mm^3	50.4 ± 20.9	0.44	47.3 ± 14.1	0.70
Density-weighted bending strength parameters					
$I_{\rho.min}$	mg·mm^2	73.7 ± 35.2	0.76	58.9 ± 34.3	0.85
$I_{\rho.max}$	mg·mm^2	119.7 ± 71.6	0.43	108.5 ± 47.0	0.72
$S_{\rho.min}$	mg·mm	17.8 ± 6.7	0.82	14.5 ± 6.9	0.87
$S_{\rho.max}$	mg·mm	28.7 ± 13.4	0.46	27.0 ± 10.1	0.68

For Met2, all bone quantity and geometric strength parameters except for mid-diaphysis area and bending strength maxima (I_{max} and S_{max}) were significantly correlated with F_{ult}. The strongest individual predictor was mid-diaphysis Ct.Th ($r^2 = 0.85$). Two other variables (BR and $S_{\rho.min}$) had univariate values of $r^2 > 0.64$. The stepwise multiple

regression analysis for Met2 yielded a model that included only mid-diaphysis Ct.Th (Table 2.2).

For Met3, all bone quantity and geometric strength parameters were significantly correlated with $\mathbf{F}_{ult}$. Univariate regression analyses revealed that $I_{\rho.min}$ and $S_{\rho.min}$ explained 72% and 75% of variance in $\mathbf{F}_{ult}$, respectively; mid-diaphysis Ct.Th explained 69%. The final stepwise model for $\mathbf{F}_{ult}$ included $S_{\rho.min}$ and mid-diaphysis Ct.Th and predicted a total of 89% of the variance in $\mathbf{F}_{ult}$ (Table 2.2).

Table 2.2: Results of stepwise multiple regressions for $\mathbf{F}_{ult}$ in Met2 and Met3. SEE = standard error of estimate.

$\mathbf{F}_{ult}$ regression equation	R^2	Adjusted R^2	SEE (in N)
Met 2			
Model 1: $\mathbf{F}_{ult} = 559 * Ct.Th - 458$ N	0.852	0.834	122
Met3			
Model 1: $\mathbf{F}_{ult} = 30.5 * S_{\rho.min} - 34$ N	0.752	0.721	129
Model 2: $\mathbf{F}_{ult} = 20.5 * S_{\rho.min} + 302 * Ct.Th - 386$ N	0.914	0.889	81

2.5   *DISCUSSION*

Using vQCT scanning and processing methods directly applicable to *in vivo* testing, we produced findings that compare favorably with previous investigations using excised bones to predict bending strength in human metatarsals. To our knowledge, this is the first attempt to implement bone axis realignment of human vQCT image data, as well as the first use of buckling ratio and density-weighted bending strength indices in foot bones.

In contrast to previous research using metatarsals (Courtney *et al.*, 1997; Muehleman *et al.*, 2000), we found that geometric bending strength indices ($I_{\rho.min}$ and $S_{\rho.min}$) were more predictive of *ex vivo* ultimate force than BMD. Courtney *et al* used DXA to compute areal BMD at the mid-diaphysis in 11 pairs of excised Met2 and Met3 samples, then conducted fracture testing in a 4-point loading configuration. $\mathbf{F}_{ult}$ values for 3-point and 4-point loading are not directly comparable, but computing $\mathbf{M}_{ult}$ allows comparison between the testing techniques. Our results for $\mathbf{M}_{ult}$ (Met2 = 4.72 ± 2.47 N*m, Met3 = 3.36 ± 2.01 N*m for Met3) are roughly 30% lower for Met2 and 40% lower for Met3 than values computed based on $\mathbf{F}_{ult}$ data in Courtney *et al* (Met2 = 6.5 ± 3.8 N*m, Met3 = 5.5 ± 3.0 N*m), which can attributed in part to the older age of our cadaver samples (83 ± 13 yrs) compared to an average age of 63 yrs in Courtney *et al*. The authors also computed areal bone geometric measures (thickness, $I_{Area.min}$, and $I_{Area.max}$) using a binary definition of bone and non-bone material based on a digital photograph of a single cross-section near the mid-diaphysis. BMD was a strong predictor of metatarsal strength (r^2 = 0.81-0.83) whereas geometric properties neither correlated significantly with strength nor contributed additional significance in stepwise multiple

regression (Courtney *et al.*, 1997). Another study (Muehleman *et al.*, 2000) compared DXA and pQCT measures of BMD and bone geometry as predictors of failure strength of excised Met2 samples in a cantilever loading configuration and found similar results: BMD was the strongest correlate of failure load for both DXA ($r^2 = 0.40$) and pQCT ($r^2 = 0.46$), and geometric strength indices did not correlate significantly to bone failure strength.

These previous analyses used areal measures of bending strength based on an assumption of unit density in bone material. Our findings suggest that density-weighted geometric bending parameters were more highly correlated to F_{ult} than areal measures. A density-weighted approach may lessen the effects of suboptimal spatial resolution by improving the density resolution. Additionally, both papers utilized cadaver metatarsals that were excised before imaging. It is not clear that similar accuracy and precision of BMD and geometric indices would be achieved using *in vivo* techniques. Future clinical utility of DXA or pQCT rests on the ability to replicate findings using a technique applicable to *in vivo* testing. Our novel technique allows measurement of cross-sectional strength properties using vQCT scanning and post-processing bone axis realignment.

Numerous bone quantity and geometric strength parameters measured with the novel vQCT method relate strongly to $\mathbf{F}_{ult}$. For both bones, vQCT-based indices of bending strength accounted for more variance in $\mathbf{F}_{ult}$ than BMD, and density-weighted indices of bending strength were superior to areal unit density indices. Some caution should be taken regarding the findings from the regression analyses, as correlation coefficients are potentially volatile with such a small number of samples relative to the number of independent variables included. The single highest correlate of $\mathbf{F}_{ult}$ in Met2

27

and Met3 was mid-diaphysis Ct.Th. The strong relationship between mid-diaphysis Ct.Th and F_{ult} is highly relevant to changes that occur due to aging, as bones maintain measures of bending strength (despite age-related loss in BMD) through a process of homeostatic expansion that leaves bones at elevated risk for focal cortical shell weakness and fractures (Beck, 2007). Future analyses may assess whether the strong relationship between Ct.Th and F_{ult} persists for younger or athletic populations.

One limitation of this study is that clinical vQCT spatial resolution (0.4mm isotropic) leads to partial volume effects that limit the ability to determine Ct.Th directly (Beck, 2007). To adequately distinguish cortical and trabecular bone would require voxel spatial resolution of roughly 100 μm (0.1 mm) (Beck, 2007) which is currently limited to HR-pQCT and micro-computed tomography (μCT) and thus not applicable to *in vivo* scanning of foot bones. Future investigations using cadaver samples may validate the vQCT-based methods using high resolution μCT (spatial resolution 10-30 μm) as a gold standard to optimize vQCT thresholds and study changes in cortical porosity (Zebaze *et al.*, 2010). Similarly, μCT validation of vQCT measures could be used in future research to assess bone quality and fracture risk in tarsal bones, which have predominantly trabecular bone and are subjected to different loading modes than the metatarsals (Diederichs *et al.*, 2009).

A potential future direction using vQCT-based assessment of metatarsal strength indices is to relate the predicted ultimate loading capacity to *in vivo* loading calculated using plantar pressure measurement. Stokes *et al* (Stokes *et al.*, 1979) estimated compressive force, shear force, and bending moments in metatarsals using plantar pressure mapping, videographic assessment, and cadaver-based estimates of bone

geometry. The methods we report here could be used as direct measures of bone quantity and geometry, in lieu of the estimated geometry calculated by Stokes *et al.* Furthermore, vQCT-based assessment of metatarsal strength indices could be combined with direct *in vivo* assessment of metatarsal strain (Arndt *et al.*, 2002) to provide a full representation of the interplay among bone structure, loading, and deformation.

In conclusion, this study represents the novel development and *ex vivo* validation of a clinically applicable vQCT-based method to assess human metatarsal strength. The methods can be used for *in vivo* imaging to non-invasively estimate bone strength and fracture risk by providing direct, volumetric measurement of BMD and bone geometric strength indices. Our findings suggest that average mid-diaphysis bone thickness, buckling ratio, minimal moment of inertia and minimal section modulus may be important indices of metatarsal strength in future *in vivo* studies.

CHAPTER 3

Impact of Charcot neuropathic osteoarthropathy on metatarsal

bone mineral density and geometric strength indices

Status of resulting manuscript: in review, *Bone*

Authors: David J. Gutekunst, Kirk E. Smith, Paul K. Commean, Kathryn L. Bohnert, Fred W. Prior, and David R. Sinacore

3.1 ABSTRACT

Charcot neuropathic osteoarthropathy (CN), an inflammatory condition characterized by rapid and progressive destruction of pedal bones and joints, is a common precursor to deformity and ulceration in individuals with diabetes mellitus (DM) and peripheral neuropathy (PN). Repetitive, unperceived joint trauma may trigger initial CN damage, leading to a proinflammatory cascade that can result in osteolysis and contribute to subsequent neuropathic fracture. The purpose of this study was to characterize osteolytic changes related to development and progression of CN by comparing BMD and bone geometric strength indices derived from volumetric quantitative computed tomography in twenty individuals with DM+PN to twenty age-, sex-, and race-matched individuals with DM+PN and acute CN. We hypothesized that individuals with acute CN would have decreased BMD and decreased Tt.Ar, Ct.Ar, S_{min}, and Ct.Th in the proximal, central, and distal diaphyseal regions of Met2 and the fifth metatarsal (Met5). Results showed that bone mineral density was lower at all diaphyseal regions in both involved and uninvolved feet of CN participants compared to DM+PN participants, with greater reductions in involved CN feet compared to uninvolved CN feet. There was a non-significant increase in total area and cortical area in the CN metatarsals, which helps explain the finding of similar minimum section modulus in DM+PN and CN subjects despite the CN group's significantly lower BMD. Larger cortical area and minimum section modulus are typically considered signs of greater bone strength due to higher resistance to compressive and bending loads, respectively. In CN metatarsals, however, these findings may reflect periosteal woven bone apposition, i.e. a hypertrophic response to injury rather than increased fracture resistance.

3.2 INTRODUCTION

Diabetes mellitus (DM) and peripheral neuropathy (PN) are the most common precursors of Charcot neuropathic osteoarthropathy (CN) (Lee *et al.*, 2003), a progressive, inflammation-mediated destruction of bones and joints leading to fracture, subluxation, and dislocation, which in turn result in progressive foot deformities that increase the risk of plantar ulceration, infection, and ultimately amputation (Frykberg and Belczyk, 2008; Rogers *et al.*, 2011; Thompson, Jr. and Clohisy, 1993). The etiology of CN remains incompletely understood, though previous research suggests that development and progression of CN are related to elevated biomechanical loading (Armstrong and Lavery, 1998), joint mal-alignment (Sinacore *et al.*, 2008; Armstrong *et al.*, 1997; Cavanagh *et al.*, 1994; Chantelau, 2005) and focal bone loss (Sinacore *et al.*, 2008; Bem *et al.*, 2010; Chantelau, 2005). BMD may also affect the clinical manifestation of CN: a clinical presentation of pedal fracture is more common in individuals classified as osteopenic or osteoporotic using DXA at the hip, whereas pedal subluxations and dislocations are more common in those with normal or high BMD (Herbst *et al.*, 2004). Acute CN patients have reduced DXA-derived BMD in the lower leg compared to control subjects with neuropathy (Young *et al.*, 1995). Sinacore *et al.* used quantitative ultrasound and found lower estimated calcaneal BMD in CN patients compared to matched non-diabetic controls (Sinacore *et al.*, 2008), though Petrova *et al.* found lower BMD only in CN patients with Type 1 but not Type 2 DM (Petrova *et al.*, 2005).

The metatarsals are the most frequent site of foot fracture (Cundy *et al.*, 1985; Weinfeld *et al.*, 1997; Wolf, 1998), and a link has been suggested between focal

osteopenia in the feet and an increased risk of metatarsal fracture (Cundy *et al.*, 1985; Gill *et al.*, 1997) and "silent" bone stress injuries (Chantelau *et al.*, 2007) in individuals with DM and PN. However, neither DXA nor calcaneal QUS provides a direct, quantitative assessment of BMD in the pedal bones most prone to fracture. A semi-automated bone segmentation technique using vQCT to compute bone volumes and BMD for the tarsals and metatarsals has been recently developed (Commean *et al.*, 2009; Commean *et al.*, 2011), though the importance of BMD as a predictor of acute or overuse metatarsal fracture remains unclear. In other long bones, geometric strength indices have been more highly correlated to fracture risk than has BMD alone. For example, in the tibia, the strongest predictors of fracture include geometric indices that reflect resistance to compression, such as Ct.Ar, and resistance to bending loads, such as minimum moment of inertia (I_{min}) and minimum section modulus (S_{min}) (Evans *et al.*, 2008; Brudvig *et al.*, 1983; Kontulainen *et al.*, 2008; Liu *et al.*, 2007; Manske *et al.*, 2006). In the femoral neck, cortical shell weakness plays a larger role in fracture risk. Increased hip fracture risk is associated with decreased Ct.Th and increased BR (LaCroix *et al.*, 2010; Melton, III *et al.*, 2005; Szulc *et al.*, 2006), thought to be caused by an age-related *homeostatic expansion* of the periosteal surface with a concomitant larger expansion of the endosteal cavity (Sigurdsson *et al.*, 2006; Ward *et al.*, 2011) which helps to maintain bending strength despite declining bone mineral content (Beck, 2007; LaCroix *et al.*, 2010). The relationship between fracture risk and bone geometry has not been studied in detail in human metatarsals, though cadaver studies have shown strong relationships between *ex vivo* ultimate bending loads and BMD (Courtney *et al.*, 1997; Muehleman *et*

al., 2000) and indices of bending strength (I_{min}, S_{min}) and cortical shell integrity (Ct.Th) (Gutekunst *et al.*, 2012).

The purpose of this study was to characterize bony changes that may lead to increased fracture risk due to CN by comparing BMD and bone geometric strength indices in the metatarsals of individuals with DM, PN, and acute CN to a matched group with DM and PN. Bone geometric strength indices reflect resistance to fracture in compressive (Tt.Ar, Ct.Ar), bending (S_{min}), and local buckling (Ct.Th) fracture loading modes. Met2 and Met5 were chosen because they are representative medial and lateral column bones, as well as common sites of neuropathic fracture (Cundy *et al.*, 1985; Chantelau *et al.*, 2007). Since Met2 and Met5 may be prone to highly focal inflammation-mediated osteolysis, BMD and geometric strength indices were assessed in discrete locations representing the proximal, central, and distal diaphyseal regions.

3.3   MATERIALS AND METHODS

3.3.1   Subjects

Subjects were recruited from the clinical population receiving orthopedic and physical therapy treatment for foot and ankle complications at Barnes-Jewish Hospital and the Washington University School of Medicine in St Louis, Missouri. Twenty individuals with acute onset CN and twenty individuals with DM and PN who did not have CN agreed to participate and provided written informed consent in accordance with the guidelines of the Institutional Review Board and the Human Research Protection Office. Three individuals in the CN group (2 females, 1 male) were excluded from the analysis due to severe joint inflammation in the CN-Involved foot that prevented bone

segmentation processing. Demographic data for the 17 remaining CN subjects and the 20

DM+PN subjects are presented in Table 3.1.

Table 3.1: Demographic and physical information for bone strength comparison.

	DM+PN	*CN*
N	20	17
Sex (F/M)	11/9	9/8
Ethnicity	13 White 7 African-American	12 White 4 African-American 1 Hispanic
Age (years)	57.6 ± 10.8	54.9 ± 9.7
Height (cm)	171.7 ± 8.4	174.2 ± 7.5
Mass (kg)	94.9 ± 25.7	109.6 ± 26.0
Body mass index (kg/m^2)	32.0 ± 8.1	36.0 ± 7.7
Diabetes Type (Type1/Type2)	2/18	3/14
HbA1c (%)	7.8 ± 1.4	7.8 ± 1.8
DM duration (years)	13.9 ± 12.6	17.4 ± 10.8
PN duration (years)	5.2 ± 3.5	7.4 ± 4.8
Met2 length (mm)	79.4 ± 4.2	78.7 ± 5.7
Met5 length (mm)	75.4 ± 3.7	73.8 ± 4.5

3.3.2 vQCT Scans and Bone Segmentation Processing

Volumetric QCT scans were taken at the Center for Clinical Imaging and

Research at the Washington University School of Medicine using a Siemens SOMATOM

Definition CT scanner (Siemens Medical Systems, Malvern, PA, USA) with acquisition

parameters of 220 mA·s, 120 kVp, pitch = 1, rotation time 0.33s, and a 512x512 matrix.

A B70f reconstruction kernel was used to create vQCT images at 0.6mm slice interval

with in-plane resolution of 0.4-0.55mm (Commean *et al.*, 2011; Smith *et al.*, 2011). A

bone calibration phantom (Image Analysis Inc., Columbia, KY, USA) was included with

each scan to allow conversion from X-ray absorptiometry in HU to equivalent calcium

HA concentration in mg/cm^3. The bone segmentation process, which leads to a series of

bone object maps (Figure 3.1), has been described in detail elsewhere (Liu *et al.*, 2008;

Commean *et al.*, 2011). In brief, a density-based filtering algorithm was used to

distinguish bone tissue from surrounding soft tissue using ImageJ (NIH Research

Services Branch, Bethesda, MD), then bones were segmented from each other at their

articulating surfaces using Analyze software (Biomedical Imaging Resource, Mayo

Clinic, Rochester, MN) and a custom graph-cut software tool (Liu *et al.*, 2008).
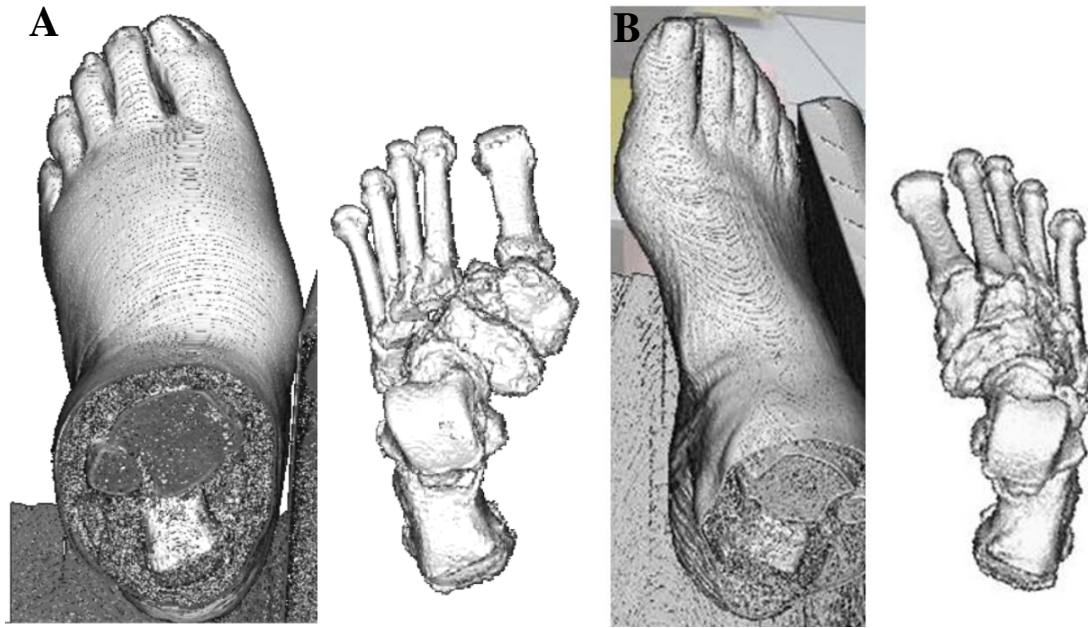
Figure 3.1: Bone segmentation processing. Raw vQCT image and filtered, segmented, filled bone object maps for tarsals and metatarsals for (A) CN-Involved foot and (B) CN-Uninvolved foot.

3.3.3   Bone Mineral Density and Geometric Strength Indices

Full methods for bone geometric strength processing are provided in Chapter 2 and in the literature (Gutekunst *et al.*, 2012). In brief, the segmented bone object maps were overlaid on the raw grayscale voxel data, and the resulting voxel datasets (XYZ position and HU values) were transformed along each bone's longitudinal axis using the BoneJ plug-in (Doube *et al.*, 2010) within ImageJ. Realigned voxel data were interpolated to isotropic voxels (0.5mm dimension) in Analyze® software, then exported to custom Excel (Microsoft) macros. In the processing macros, HU values were converted to equivalent BMD (mg/cm^3) using scan-specific HA calibration phantoms.

Calculations of bone geometric strength indices were modeled after guidelines for μCT (Bouxsein *et al.*, 2010). For each realigned slice, BMD (mg/cm^3) was computed by

first summing the total equivalent bone mineral content (mg), i.e. the product of all positive voxel BMD values and each voxel's volume, then dividing the bone mineral content by the total volume within the periosteal window. Thus the BMD values reported here represent the average BMD over the total tissue volume within each diaphyseal region. S_{min} (mg*mm), which is inversely proportional to bending stress within the bone (Turner and Burr, 1993). S_{min} was measured by computing the density-weighted minimum cross-sectional I_{min} (mg*mm^2) and dividing by the distance from the density-weighted center of mass to the periosteal edge, as described in Chapter 2 and in the literature (Gutekunst *et al.*, 2012). Tt.Ar was computed by summing total cross-sectional area within the periosteal envelope, including the medullary cavity, whereas Ct.Ar was computing by summing the cross-sectional area of voxels exceeding a threshold of 300 mg/cm^3. The spatial resolution of the vQCT scans prevented direct measurement of Ct.Th, and instead the average Ct.Th was computed using Tt.Ar and Ct.Ar with the assumption that the metatarsal diaphysis is roughly a circular annulus. Bone length was computed by multiplying the slice thickness (0.5 mm) by the total number of slices. Proximal, central, and distal diaphyseal regions were defined as 33%, 50%, and 67%, respectively, of the distance from the most proximal slice to the most distal slice of the realigned bones (Figure 3.2). For each region, BMD and geometric strength indices were averaged over five slices (2.5 mm) to reduce noise.
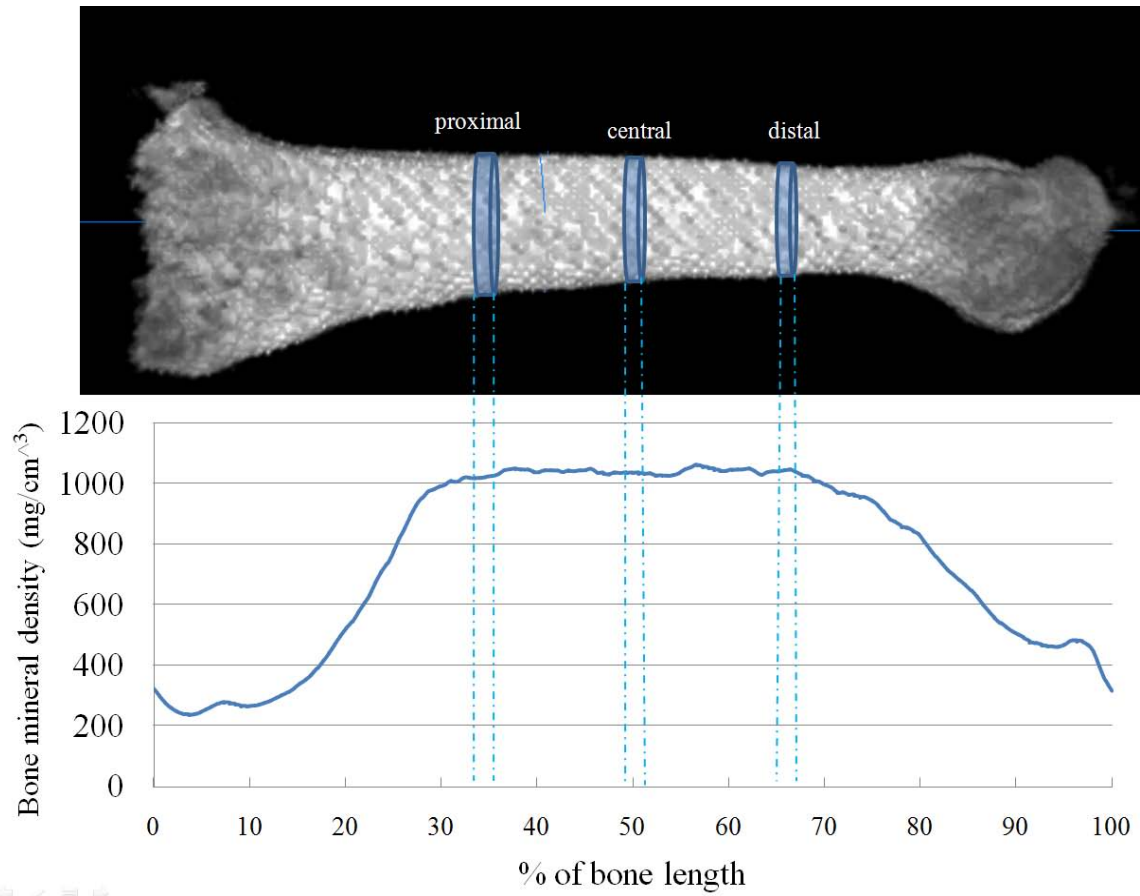
Figure 3.2: Exemplar sample of a segmented second metatarsal showing diaphyseal regions (top) and associated bone mineral density profile along the bone's longitudinal axis (bottom)

3.3.4   Statistical Analyses

Subject sex, ethnicity, and DM type were compared between groups using chi-square tests. Age, height, weight, body mass index, DM duration, and PN duration were compared using the Student's t-test. Additionally, a two-way ANOVA (Group * Foot) was used to compare the lengths of Met2 and Met5 to ensure that any differences in bone geometric strength indices (especially Tt.Ar, Ct.Ar and S_{min}) were not due to differences in overall bone size. For each dependent variable (BMD, S_{min}, Tt.Ar, Ct.Ar, and Ct.Th), a three-way analysis of variance was used to test the effects of Group, Foot, and Region.

For CN subjects, foot was coded as Involved or Uninvolved. For DM+PN subjects, neither foot was affected by CN, but for statistical comparisons between the two groups it was necessary to designate one foot per subject as "involved." We arbitrarily chose the right feet of DM+PN subjects as "involved" and then tested the hypothesis that there would be no side-to-side differences in DM+PN subjects. Planned comparisons at each bone region included (a) group comparisons for matched feet (CN-Involved versus DM+PN Right), and (b) side-to-side comparisons within Group (Involved versus Uninvolved for CN subjects and Right versus Left for DM+PN subjects). The significance level was set at $\alpha \leq 0.05$, with Bonferroni adjustments for multiple post-hoc comparisons. All statistical analyses were completed in SPSS version 20.0 (IBM Corp., Chicago, IL, USA).

3.4   RESULTS

The two groups did not differ in any demographic or physical characteristics (Table 3.1). Table 3.2 shows the mean and standard deviation for each combination of group and foot, averaged across the three diaphyseal regions. Control DM+PN subjects had no side-to-side differences for BMD or any bone geometric strength measure. BMD showed a significant main effect of group, as CN subjects had 14% lower BMD in Met2 ($p = 0.002$) and 11% lower BMD in Met5 ($p = 0.019$). The CN subjects had significantly lower BMD in the Involved foot compared to the Uninvolved foot, roughly 7% lower for both Met2 and Met5. Both Tt.Ar and Ct.Ar were nominally higher (roughly 10-15%) in CN subjects compared to DM+PN, though neither reached statistical significance for

either Met2 or Met5, and there were no side-to-side differences in either areal measure in the CN subjects. S_{min} was not different between CN and DM+PN, though in Met2 there was a trend for lower S_{min} in the CN-Involved foot compared to CN-Uninvolved (9% lower, $p = 0.06$) and in Met5 there was a significant 14% reduction in CN-Involved compared to CN-Uninvolved ($p = 0.004$).

Table 3.2: Bone mineral density and bone geometric strength indices, averaged across diaphyseal regions

	Diabetes Mellitus Peripheral Neuropathy (DM+PN)			Charcot Neuroarthropathy (CN)			Main effect:
	Left (L)	**Right (R)**	*L vs R*	**Uninvolved (U)**	**Involved (I)**	*U vs I*	**DM+PN vs CN**
BMD (mg/cm³)							
Met2	1117 ± 141	1105 ± 134	*p* = 0.60	997 ± 157	923 ± 155	*p* = 0.005	*p* = 0.002
Met5	946 ± 147	962 ± 137	*p* = 0.54	877 ± 131	814 ± 162	*p* = 0.026	*p* = 0.019
Tt.Ar (mm²)							
Met2	62.1 ± 10.2	64.1 ± 12.7	*p* = 0.20	73.7 ± 19.8	72.8 ± 25.0	*p* = 0.79	*p* = 0.07
Met5	86.2 ± 19.2	86.5 ± 18.0	*p* = 0.83	95.1 ± 26.7	95.8 ± 24.7	*p* = 0.80	*p* = 0.21
Ct.Ar (mm²)							
Met2	43.6 ± 7.1	45.0 ± 9.4	*p* = 0.52	51.6 ± 13.1	51.1 ± 21.3	*p* = 0.83	*p* = 0.10
Met5	53.2 ± 10.5	54.6 ± 10.7	*p* = 0.36	61.8 ± 17.0	59.4 ± 15.4	*p* = 0.17	*p* = 0.13
*S_min (mg*mm)*							
Met2	28.5 ± 5.8	29.6 ± 7.7	*p* = 0.36	31.4 ± 10.7	28.8 ± 11.6	*p* = 0.061	*p* = 0.72
Met5	31.1 ± 11.6	32.7 ± 10.7	*p* = 0.31	37.3 ± 16.7	32.0 ± 14.6	*p* = 0.004	*p* = 0.52
Ct.Th (mm)							
Met2	2.05 ± 0.28	2.06 ± 0.33	*p* = 0.80	2.17 ± 0.37	2.15 ± 0.62	*p* = 0.86	*p* = 0.51
Met5	2.02 ± 0.27	2.08 ± 0.28	*p* = 0.29	2.23 ± 0.40	2.14 ± 0.39	*p* = 0.22	*p* = 0.19

When the proximal, central, and distal regions were considered individually, there were no side-to-side differences in DM+PN subjects for BMD or bone geometric strength indices in any region. Thus, DM+PN values are averaged across left and right feet in Figures 3.3 – 3.7. As shown in Figure 3.3, BMD was significantly lower in CN individuals than DM+PN controls at all regions in both Met2 and Met5. In Met2, the CN-Involved feet had 20% lower BMD than the DM+PN subjects at the proximal region ($p < 0.001$), 16% lower BMD in the central region ($p = 0.001$), and 14% in the distal region ($p = 0.006$). The CN-Involved feet also had 9% lower BMD compared to the CN-Uninvolved feet in the proximal region and central regions (both $p < 0.01$). In Met5, the CN-Involved feet had 16% lower BMD than the DM+PN subjects at the proximal region, 11% lower in the central region, and 20% lower in the distal region. DM+PN controls showed no side-to-side differences, whereas CN individuals had 8% lower BMD in their involved feet compared to uninvolved feet. Regional comparisons showed 5-6% lower BMD in the proximal and central regions of CN-Involved feet compared to Uninvolved ($p > 0.05$), and 14% lower BMD in the distal region ($p = 0.008$).

(A)

(B)
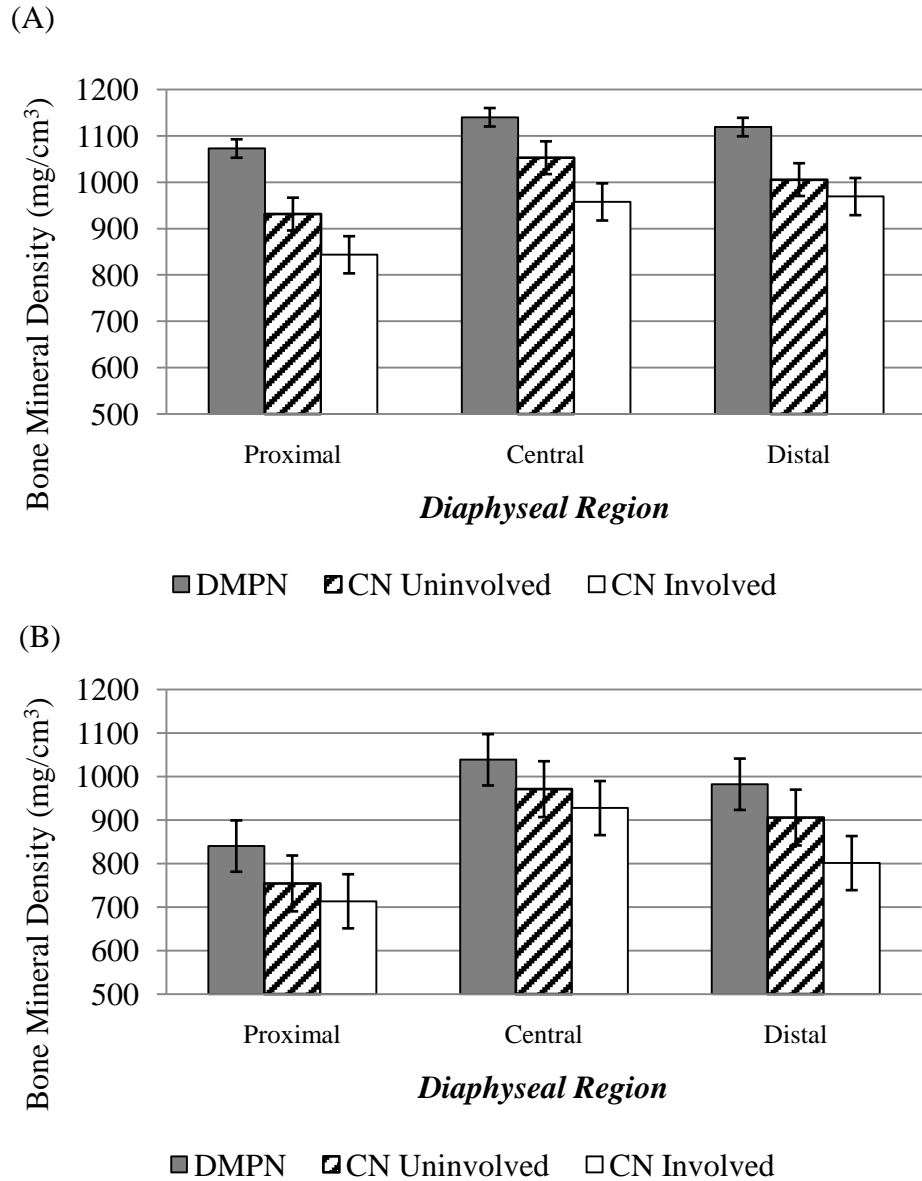
Figure 3.3: Group mean ± standard error for bone mineral density (mg/cm^3) in the proximal, central, and distal diaphyseal regions of (A) Metatarsal 2, and (B) Metatarsal 5. * $p \leq 0.01$ for CN foot compared to DM PN feet. †† $p \leq 0.01$ for CN-Involved compared to CN-Uninvolved.

As shown in Figures 3.4 and 3.5, compared to DM+PN subjects, the CN subjects had nominally larger ($p > 0.05$) cross-sectional Tt.Ar and Ct.Ar across all regions. The CN subjects had 11-18% higher Tt.Ar in Met2 and 8-20% higher Tt.Ar in Met5, though

only the proximal region of Met2 and the distal region of Met5 showed a trend toward statistical significance, with 20% larger Tt.Ar in the proximal region of Met2 (82 mm^2 versus 98 mm^2, $p = 0.055$) and 18% larger Tt.Ar in the distal region of Met5, (62 mm^2 versus 73 mm^2, $p = 0.095$).

(A)

(B)
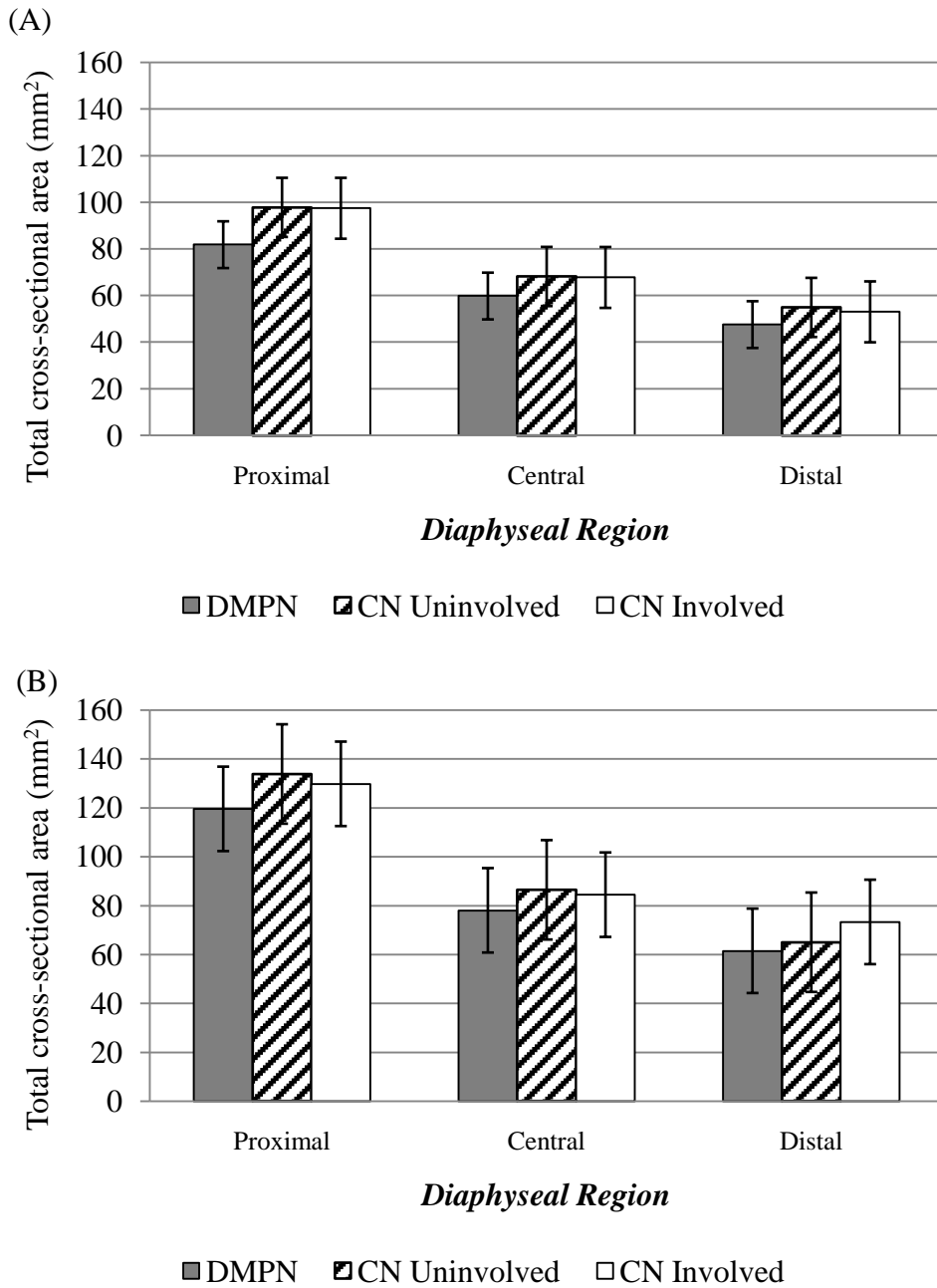
Figure 3.4: Group mean ± standard error for total cross-sectional area, Tt.Ar (mm^2) in the proximal, central, and distal diaphyseal regions of (A) Metatarsal 2, and (B) Metatarsal 5.

(A)

Diaphyseal Region

☐ DMPN ☒ CN Uninvolved ☐ CN Involved

(B

Shaft Region

☐ DMPN ☒ CN Uninvolved ☐ CN Involved
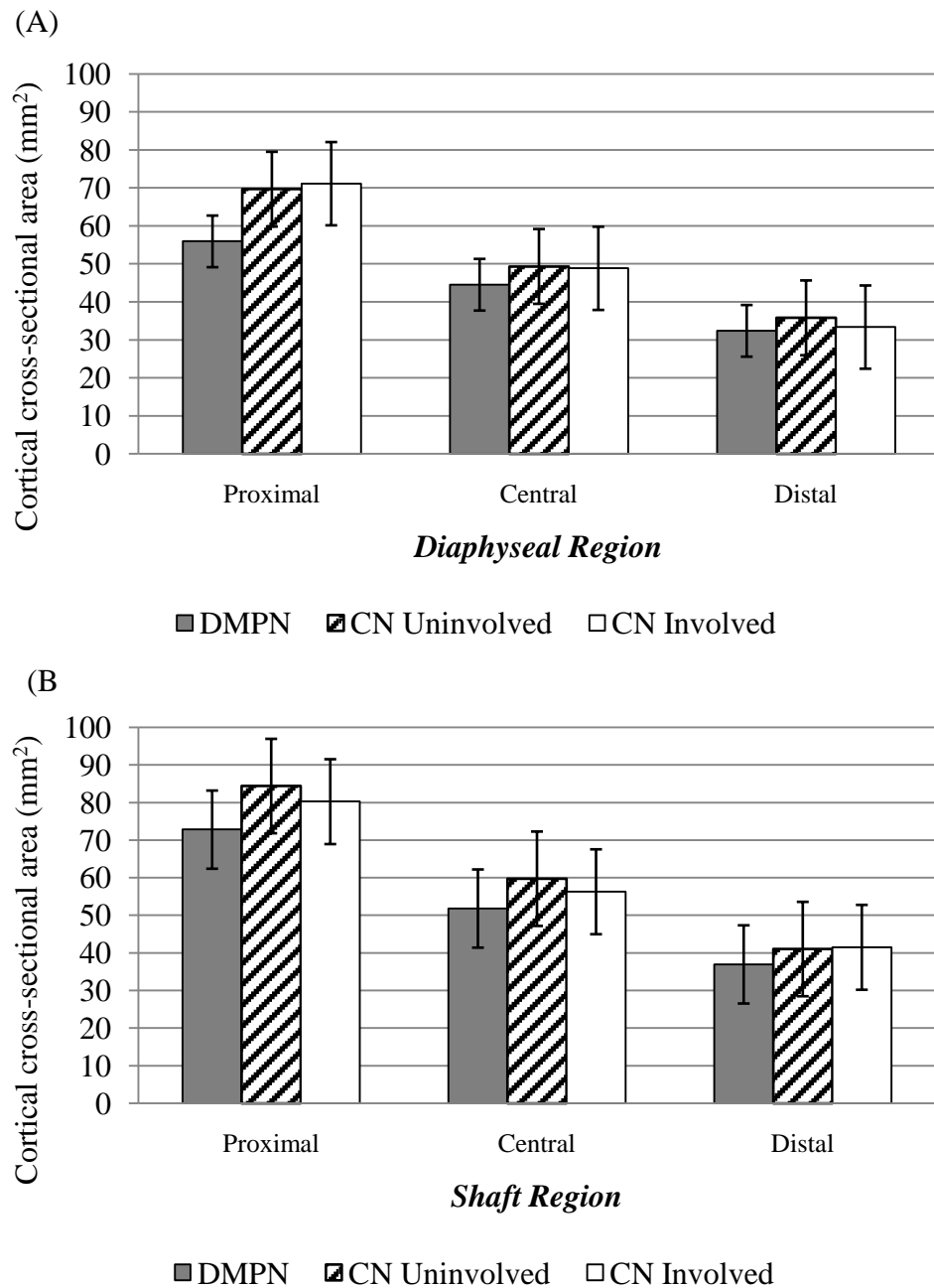
Figure 3.5: Group mean ± standard error for cortical cross-sectional area, Ct.Ar (mm^2) in the proximal, central, and distal diaphyseal regions of (A) Metatarsal 2, and (B) Metatarsal 5.

There were no group differences at any region for S_{min} in either Met2 or Met5 (Figure 3.6). The DM+PN subjects showed no side-to-side differences, but the CN-Involved feet had lower values of S_{min} than CN-Uninvolved at multiple regions: 11%

lower for the proximal region of Met2 ($p = 0.029$), 14% lower for the proximal region of

Met5 ($p = 0.008$), 13% lower in the central region of Met5 ($p = 0.010$), and 17% lower in

the distal region of Met5 ($p = 0.010$). There were no group differences or side-to-side

differences for Ct.Th in any region (Figure 3.7).

(A)

(B)
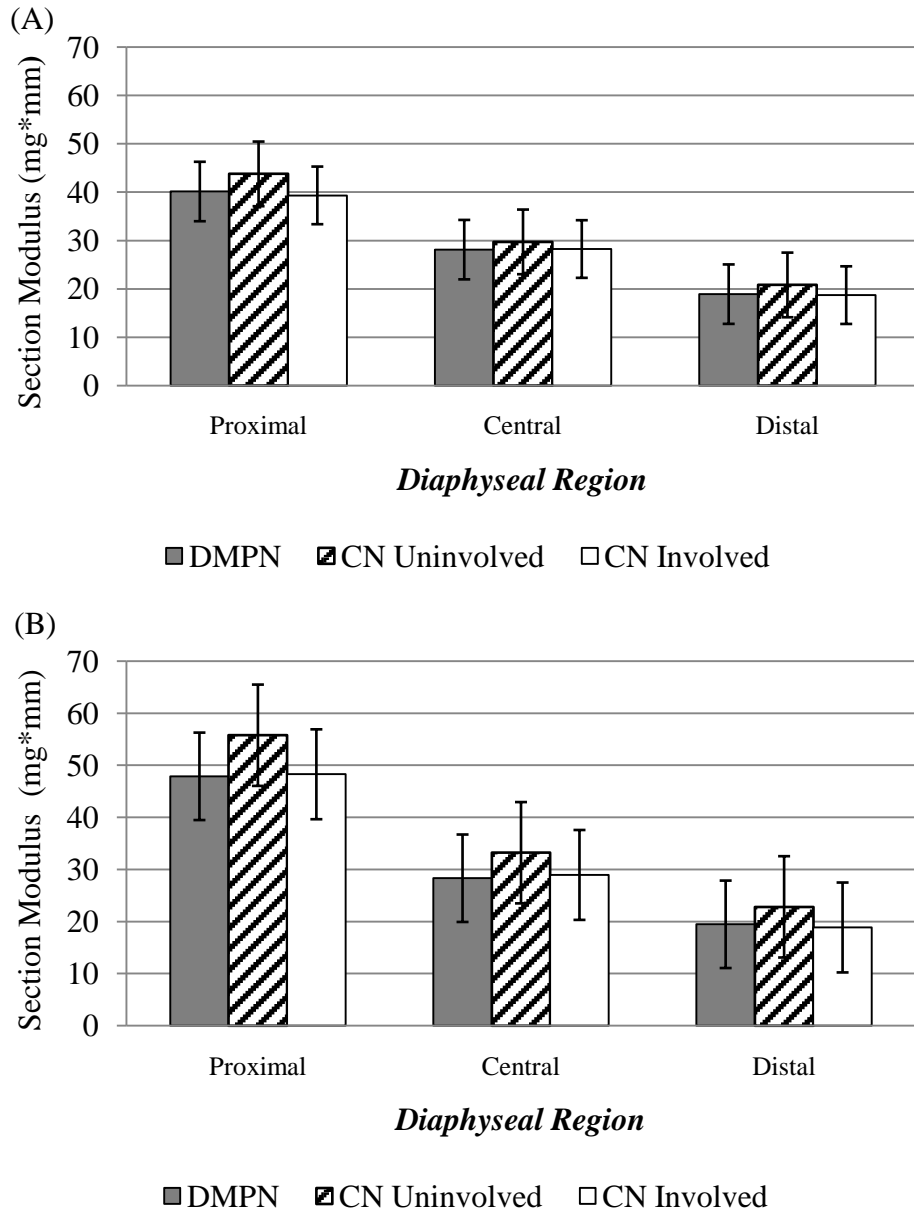
Figure 3.6: Group mean ± standard error for minimum section modulus, S_{min} (mg*mm^2) in the proximal, central, and distal diaphyseal regions of (A) Metatarsal 2, and (B) Metatarsal 5. † $p \leq$ 0.05 for CN-Involved compared to CN-Uninvolved; †† $p \leq 0.01$ for CN-Involved compared to CN-Uninvolved.

(A)
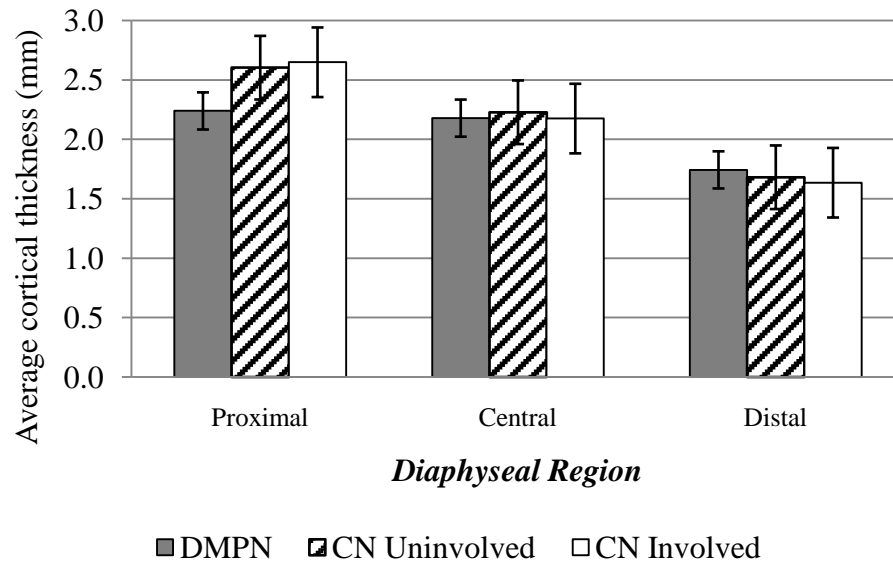
(B)
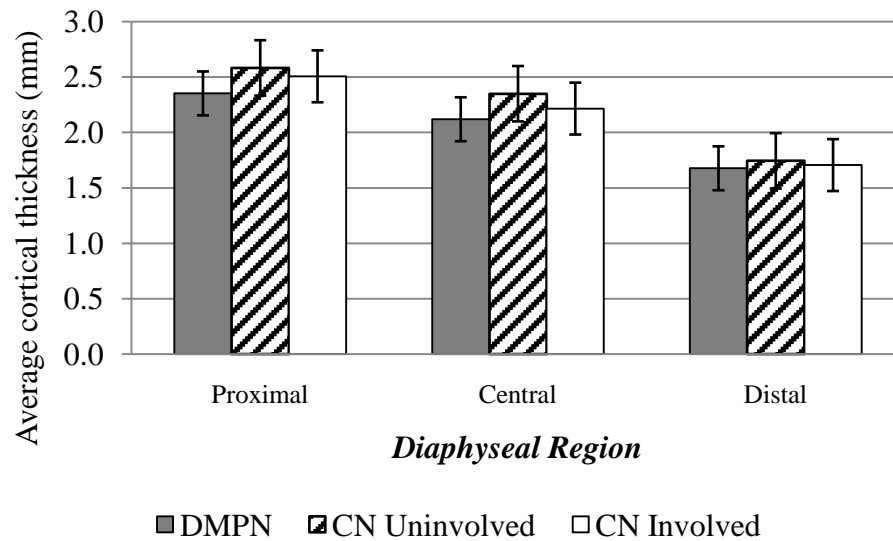
Figure 3.7: Group mean ± standard error for average cortical thickness, Ct.Th (mm) in the proximal, central, and distal diaphyseal regions of (A) Metatarsal 2, and (B) Metatarsal 5.

3.5   DISCUSSION

This is the first study to quantify the effects of acute CN on BMD and bone

strength-related indices in the metatarsals using vQCT. In both Met2 and Met5, which are

common sites of foot fracture (Wolf, 1998; Weinfeld *et al.*, 1997), we report decreased

BMD throughout the diaphysis. The lower BMD in the CN uninvolved feet compared to

DM+PN controls suggests a systemic effect of inflammation, with an additional focal

effect of inflammation in the CN involved foot. These results reinforce and clarify a

previous finding of significant reductions in calcaneal BMD (estimated by QUS) in

involved CN feet compared to uninvolved CN feet, with both lower than matched non-

DM controls (Sinacore *et al.*, 2008). The observed reduction in calcaneal BMD was

related to inflammation, assessed via pedal skin temperature measurements that showed a

4°C elevation in the involved CN feet (Sinacore *et al.*, 2008).

Elevation of pedal temperature provides a clinically observable sign of

inflammation and reflects upregulation of inflammatory pathways in the circulation.

Jeffcoate, Game, and Cavanagh (Jeffcoate *et al.*, 2005) first proposed that acute CN is

initiated by a minor injury (often undetected) that triggers a cascade of proinflammatory

cytokines, including tumor necrosis factor alpha (TNF-α) and interleukin beta (IL-β).

Increased levels of proinflammatory cytokines in turn lead to increased expression of NF-

κB and a resulting increase in osteoclastogenesis, which further weakens the bone and

leads to neuropathic fracture if loading continues on an insensate foot. This proposed

inflammatory mechanism has been corroborated by a recent study comparing peripheral

monocytes from acute CN to monocytes from DM+PN controls. Individuals with acute

CN had increased levels of proinflammatory cytokines TNF-α, IL-β, and IL-6, as well as

decreased levels of anti-inflammatory cytokines IL-4 and IL-10 (Uccioli *et al.*, 2010). These results support earlier findings that osteoclast activity is elevated in CN, with no significant change in osteoblast activity (Gough *et al.*, 1997).

There is strong epidemiological evidence of increased fracture risk in individuals with both Type 1 and Type 2 DM. In Type 1 DM, the high fracture risk is often attributed to lower BMD (Herbst *et al.*, 2004), though an increased risk of foot and ankle fracture persists even in Type 2 DM individuals with high BMD(Schwartz *et al.*, 2001) or when the effects of BMD have been accounted for statistically(Bonds *et al.*, 2006; Melton, III *et al.*, 2008). Previous research at other anatomical sites would suggest that the increased fracture risk observed in individuals with DM, PN, and CN would be associated with decreased geometric strength indices such as S_{min}, Tt.Ar, Ct.Ar, and Ct.Th, which have been predictive of fracture risk in the tibia (Brudvig *et al.*, 1983; Evans *et al.*, 2008; Beck *et al.*, 2000), femur (Kaptoge *et al.*, 2008; Beck *et al.*, 2000; Melton, III *et al.*, 2005), and metatarsals (Muehleman *et al.*, 2000; Gutekunst *et al.*, 2012). Perhaps most relevant to the current study is the cadaver validation of the vQCT-based techniques to quantify BMD and geometric strength indices presented in Chapter 2 (Gutekunst *et al.*, 2012), in which S_{min} and Ct.Th were the strongest predictors of *ex vivo* bone strength, together accounting for 83-89% of the variance in ultimate force measured during three-point bending tests.

Results from the present analysis are mixed: we report reduced BMD in both Met2 and Met5 at all regions within involved and uninvolved CN feet, but with a maintenance of Ct.Th and non-significant elevation of Tt.Ar, Ct.Ar, and S_{min}. Based on previous research, these geometric results would suggest that CN metatarsal strength

would be maintained or even enhanced, which is unexpected given the known fracture risk in CN metatarsals. One explanation for the reduction in BMD with maintained geometric strength indices is that the CN bones are responding functionally by increasing resistance to bending and buckling loads, and that any increased fracture risk in CN is due primarily to elevated biomechanical loading rather than a reduction in bone strength.

Another explanation for the Tt.Ar and Ct.Ar findings may be that the inflammatory process associated with CN leads to increased osteoclast activity and bone turnover, which at the periosteal border may lead to a hypertrophic response and an expanded, less dense region of bone callus. This would be consistent with the findings of reduced BMD in the CN group. Current vQCT technology does not permit precise quantification of parameters such as cortical porosity or woven bone formation. Thus the observed non-significant increase in Ct.Ar may reflect the metatarsals' response to injury rather than a true cortical expansion that would impart greater mechanical strength in compression and bending. The spatial resolution used in this analysis (0.5 mm isotropic voxels), while near the current limits of clinical vQCT capabilities, leads to spatial averaging of bone and non-bone material. As a result, it is more difficult to set a precise threshold to distinguish bone from marrow, or trabecular bone from cortical bone. Choosing a threshold that is too low can lead to inclusion of voxels that are not predominantly cortical bone and an overestimation of Ct.Ar and Ct.Th, but choosing a threshold that is too high can lead to erroneous discontinuities in the thinning cortical shell. Others have encountered similar issues with spatial averaging and have chosen the same threshold (300 mg/cm^2) to define bone and non-bone material (Borggrefe *et al.*, 2010). A recent study using HR-pQCT in the radius and tibia of Type 2 DM patients

reported higher values for geometric indices of bone strength, as we have shown here, but inefficient redistribution of bone mass that could result in impaired bending strength (Burghardt *et al.*, 2010). Future imaging studies of CN foot bones with improved spatial resolution, such as *in vivo* HR-pQCT or cadaver studies using μCT, will limit the effects of spatial averaging, permit a more precise threshold to be applied, and provide a clearer understanding of what is occurring at the structural level of CN bone.

In conclusion, this study presents a novel techniques to assess region-specific BMD and bone geometric strength indices in the neuropathic foot using clinical vQCT. In individuals with acute CN, reduced BMD was found at all regions in both the involved and uninvolved CN feet, with significantly greater bone reductions in the involved foot compared to uninvolved. There were non-significant elevations in CN subjects for indices of bone strength in compressive loading (Ct.Ar), bending (S_{min}), and cortical buckling (Ct.Th), though these findings may reflect an incomplete hypertrophic response to injury (Burghardt *et al.*, 2010) rather than a true improvement in fracture resistance. Future research using the methodologies presented here will assess changes in BMD and geometric indices as CN progresses from the acute stage, as well as identify bone properties that may predict which individuals with DM and PN will go on to develop CN. Finally, future imaging studies may help elucidate the pathophysiological links between inflammation, altered bone morphology, and fracture risk in Charcot neuroarthropathy.

CHAPTER 4

Development and measurement precision of anatomically relevant three-dimensional foot bone-to-bone orientation angles derived from quantitative computed tomography

Authors: David J. Gutekunst, Lu Liu, Tao Ju, Fred W. Prior, and David R. Sinacore

4.1 ABSTRACT:

Surgical treatment and clinical management of foot pathology require accurate, reliable assessment of foot deformities. Foot and ankle deformities are multi-planar and therefore difficult to quantify by standard uni-planar radiographs. Three-dimensional (3D) imaging modalities have defined bone axes based solely on bone dimensions, which limits biomechanical relevance. Defining 3D bone orientations using bone surface landmarks ensures biomechanical relevance, though quantifying measurement precision in bone-to-bone orientations is necessary to establish minimum clinically-relevant differences. Automated landmark placement method may lessen subjectivity in foot deformity assessment. The goal of this study was to assess measurement precision of landmark-based, 3D bone-to-bone orientations of hindfoot bones for expert testers and a template-based automated method.

Two testers completed two repetitions each for twenty feet (10 right, 10 left), placing anatomic landmarks on the surfaces of calcaneus, talus, cuboid, and navicular. Landmarks were also recorded using the automated method. 3D bone axes were computed from landmark positions, and Cardan sequences produced sagittal, frontal, and transverse plane angles of hindfoot bone-to-bone orientations. Angular precision was assessed as root mean square standard deviations (RMS-SD) for intra-tester, inter-tester, and tester versus automated.

RMS-SD intra-tester precision ranged from 1.4-3.6° and 2.4-6.1°, respectively, for the two testers, which compares favorably to uni-planar radiographic precision. Greatest variability was in Navicular:Talus sagittal plane angle and Cuboid:Calcaneus

frontal plane angle. Inter-tester reliability was comparable to intra-tester reliability of the less reliable tester. Precision of the automated method versus the testers was comparable to each tester's internal precision, suggesting the automated method is a valid, time-saving technique for foot deformity assessment.

4.2   *INTRODUCTION*

The task of describing foot deformities accurately and reliably presents a challenge to orthopedic surgeons, podiatrists, and rehabilitation specialists. Bony deformities in the foot and ankle are multi-planar and therefore difficult to quantify by standard uni-planar radiographic measures. Much research has focused on developing and validating multi-segment foot and ankle models using optoelectronic motion capture based on skin-mounted reflective markers placed on palpable anatomic landmarks (Stebbins *et al.*, 2006; Simon *et al.*, 2006). Three-dimensional (3D) imaging techniques such as magnetic resonance imaging (MRI) (Woodburn *et al.*, 2002; Stindel *et al.*, 1999a; Stindel *et al.*, 1999b) and quantitative computed tomography (QCT) (Ledoux *et al.*, 2006; Beimers *et al.*, 2008) have been used to quantify 3D bone-to-bone orientation angles *in vivo*, though these studies use the principal components method to define bone coordinate axes, meaning that the bone orientation axes reflect solely the bones' shape and may therefore lack anatomic relevance. A recent *in vitro* analysis utilized embedded bone pins to define and track 3D bone orientation axes using anatomically-relevant bone surface features (Whittaker *et al.*, 2011), and others have proposed anatomy-based axes to track morphological differences in the subtalar and talocrural joints (Parr *et al.*, 2012). To our

knowledge, no previous research has described methods and established bone-to-bone angular precision for *in vivo* imaging using anatomically-relevant definitions of foot bone axes.

The purposes of this study were to (1) describe an anatomic landmark-based method of defining 3D bone orientation axes for foot bones using bone atlases derived from segmented vQCT surface images; (2) determine intra-tester and inter-tester angular precision for select hind foot angles; and (3) assess the agreement between expert testers and a template-based automated landmarking method.

4.3   METHODS

4.3.1   vQCT Processing and Bone Atlases

Ten subjects underwent bilateral vQCT scans of the foot and ankle. Bones were segmented from surrounding soft tissues and from each other using ImageJ filtering plug-ins, Analyze® software (Biomedical Imaging Resource, Mayo Clinic, Rochester, MN), and custom semi-automated graph cut software (Liu *et al.*, 2008; Commean *et al.*, 2011; Commean *et al.*, 2009). The end result of segmentation is a set of binary, filled object maps which define the vQCT voxel coordinates for each bone. The segmented object maps and grayscale voxel data were imported into a custom Bone Measurement Tool, a fully automated pipeline for registering subdivision-based anatomical atlases (Liu *et al.*, 2012). The Bone Measurement Tool allows either manual placement of user-defined anatomic landmarks on the bone surfaces in a graphical user interface, or automated

landmark placement based on a template set of landmarks embedded in the underlying

bone atlas (Liu *et al.*, 2012).

4.3.2   *Selection of Anatomical Landmarks*

All 7 tarsal and 5 metatarsal bones were included in the atlas-based landmark

template, but in the current analysis only the calcaneus, talus, cuboid, and navicular were

assessed for intra-tester and inter-tester precision of landmark placement and for

agreement between manual and automated landmarking methods. The two hindfoot

(calcaneus, talus) and two lesser tarsal (navicular, cuboid) bones were chosen for

precision analysis because of their importance in foot deformities associated with

rheumatoid arthritis (Woodburn *et al.*, 2002) and Charcot neuroarthropathy (Schon *et al.*,

1998; Hastings *et al.*, 2011). Moreover, these four bones influence arch height and foot

function, and subtalar and mid-tarsal joint deformities frequently lead to mal-alignments

in the tarso-metatarsal joints and in hindfoot:forefoot coupling (Stebbins *et al.*, 2010).

Finally, pilot testing of our landmark-based methods suggested that angular

measurements of hindfoot bones were least reliable, both within and between testers,

largely because mimicking anatomically-based orientation axes used in radiographic

measures (Hastings *et al.*, 2011) necessitates identifying bone surface features that are not

located at bony edges. For example, replicating lateral X-ray measures of talo-calcaneal

angle or Meary's angle (Schwend and Drennan, 2003) require placing a landmark on the

curved surfaces of the calcaneus and talus, which can be challenging to reliably replicate

on volume-rendered bone surfaces from vQCT. The placement of surface landmarks on

planar radiographs is very dependent on the technician positioning the foot and ankle

relative to the X-ray beam during image acquisition. Therefore, foot positioning influences X-ray measures.

4.3.3   Bone Orientation Axes

Each bone's 3D axes were defined based on the locations of 3-4 anatomic landmarks. Landmarks were chosen by expert consensus to ensure anatomic relevance and consistency with established planar bone axis designations from the orthopedics literature (Schon *et al.*, 1998; Steel, III *et al.*, 1980) to produce bone axes in clinically relevant anatomical planes. Anatomical landmarks and their spatial precision are presented in Table 4.1. The resulting +X axis for each bone was directed roughly to the right (medial for left feet and lateral for right feet), +Y was defined as pointing axially (primarily anterior), and +Z was directed in a quasi-vertical direction. For all bones except navicular, the Y axis was the first axis defined, as the unit vector connecting two anatomical landmarks representing the proximal and distal termini of the main longitudinal axis of the bone. The second axis was defined as the cross-product of the first axis and a temporary ('dummy') axis, and the third axis was defined by crossing the first and second axes. Bone axis computations for each bone are provided in Table 4.2, and a schematic showing landmark placement and bone axes is shown in Figure 4.1.

Table 4.1: Anatomic landmarks and marker placement precision

Bone	Landmarks	Description
Calcaneus	1. Posterior calcaneus	Midpoint of calcaneus posterior facet, centered both medial-laterally and vertically.
	2. Anterior calcaneus	Center of the anterior surface of calcaneus, where calcaneus articulates with cuboid.
	3. Inferior calcaneus	Medial-lateral midline of calcaneus posterior facet, along the inferior border.
	4. Superior calcaneus	Medial-lateral midline of the calcaneus posterior facet, along the superior border.
Talus	5. Posterior talus	At medial-lateral midline of the posterior aspect of talus
	6. Anterior talus	Center of talar head (i.e. centered both medial-laterally and vertically)
	7. Medial talus	Medial edge of dorsum of talus, centered anterior-posteriorly
	8. Lateral talus	Lateral edge of the dorsum of talus, centered anterior-posteriorly
Cuboid	9. Posterior cuboid	Center of proximal cuboid articular surface (articulation with calcaneus)
	10. Anterior cuboid	Center of distal cuboid articular surface (articulation with fifth metatarsal)
	11. Inferior cuboid	Inferior-lateral edge of the tuberosity of cuboid
	12. Superior cuboid	Superior "point" of cuboid, at intersection of lateral, medial, & posterior facets
Navicular	13. Medial navicular	Medial aspect of navicular, centered in the anterior-posterior direction
	14. Lateral navicular	Lateral aspect of navicular; centered in the anterior-poster direction
	15. Superior navicular	Superior surface of navicular; in line with medial-lateral center of the head of talus

Table 4.2: Hindfoot bone orientation definitions based on anatomical landmarks (right foot).

Bone	First axis	Temporary axis	Second axis	Third axis
Calcaneus	$\mathbf{Y_{calc}} = \vert\, 1 \rightarrow 2 \,\vert$	$\mathbf{t_{calc}} = \vert\, 3 \rightarrow 4 \,\vert$	$\mathbf{X_{calc}} = \mathbf{Y_{calc}} \times \mathbf{t_{calc}}$	$\mathbf{Z_{calc}} = \mathbf{X_{calc}} \times \mathbf{Y_{calc}}$
Talus	$\mathbf{Y_{tal}} = \vert\, 5 \rightarrow 6 \,\vert$	$\mathbf{t_{tal}} = \vert\, 7 \rightarrow 8 \,\vert$	$\mathbf{Z_{tal}} = \mathbf{t_{tal}} \times \mathbf{Y_{tal}}$	$\mathbf{X_{tal}} = \mathbf{Y_{tal}} \times \mathbf{Z_{tal}}$
Cuboid	$\mathbf{Y_{cub}} = \vert\, 9 \rightarrow 10 \,\vert$	$\mathbf{t_{cub}} = \vert\, 11 \rightarrow 12 \,\vert$	$\mathbf{X_{cub}} = \mathbf{Y_{cub}} \times \mathbf{t_{cub}}$	$\mathbf{Z_{cub}} = \mathbf{X_{cub}} \times \mathbf{Y_{cub}}$
Navicular	$\mathbf{X_{nav}} = \vert\, 13 \rightarrow 14 \,\vert$	$\mathbf{t_{nav}} = \vert\, 13 \rightarrow 15 \,\vert$	$\mathbf{Y_{nav}} = \mathbf{t_{nav}} \times \mathbf{X_{nav}}$	$\mathbf{Z_{nav}} = \mathbf{X_{nav}} \times \mathbf{Y_{nav}}$
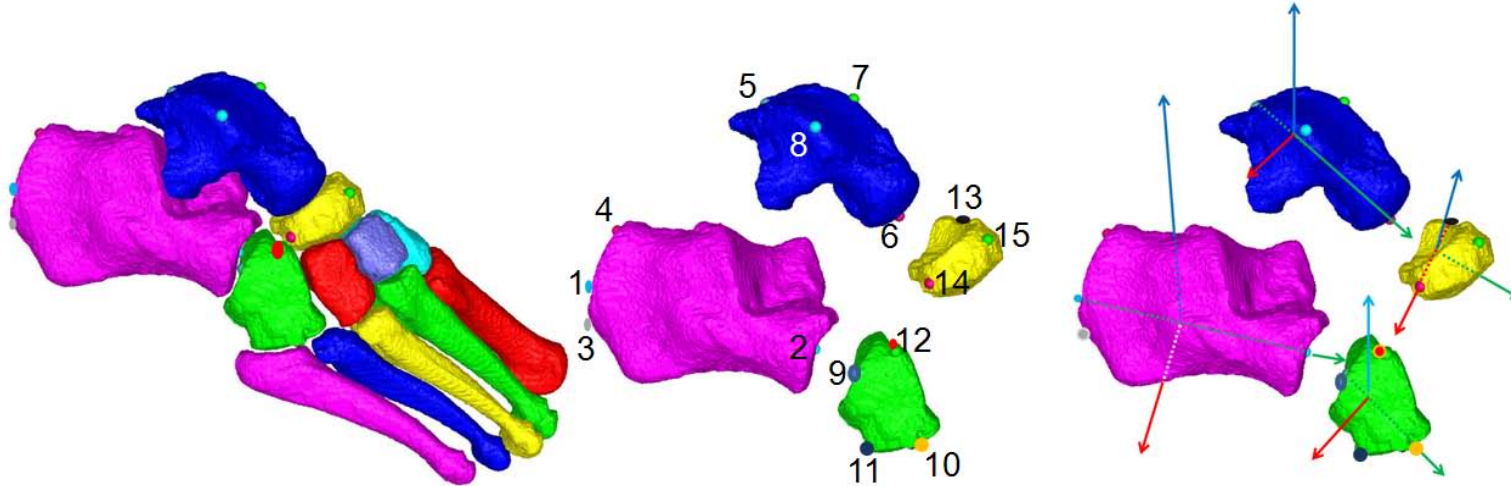
Figure 4.1: Atlas-based vQCT surface maps showing (a) all 7 tarsal and 5 metatarsal bones; (b) expanded view of hindfoot bones with labeled anatomic landmarks; (c) bone orientation axes derived from anatomical landmarks.

4.3.4 Angular Precision Assessment

Two expert testers completed two repetitions each for twenty feet, placing anatomic landmarks on the atlas-derived surfaces of calcaneus, talus, cuboid, and navicular. Landmarks were also recorded using the automated method based on a landmark template embedded within the bone atlases (Liu *et al.*, 2012). Cardan rotation sequences (XY'Z") of bone axes were used to produce sagittal (α), frontal (β), and transverse (γ) plane angles of the cuboid with respect to the calcaneus (Cub:Calc), talus with respect to the calcaneus (Tal:Calc), navicular with respect to the talus (Nav:Tal), and navicular with respect to calcaneus (Nav:Calc). Angular precision for each bone-to-bone angular rotation was assessed as root mean square standard deviations (RMS-SD) for intra-tester, inter-tester, and each tester versus the automated method.

4.4   RESULTS

Across sagittal, frontal, and transverse angles for the four bone-to-bone orientations analyzed, Tester 1 had lower RMS-SD than Tester 2 (Table 4.3). The single highest intra-tester RMS-SD for Tester 2 (Cub:Calc frontal plane angle) was 6.1°, and the highest average angular RMS-SD (for Nav:Calc) was 4.9°. Averaged across all planes and bone-to-bone orientations, intra-tester precision was 2.3° for Tester 1 and 4.1° for Tester 2. Inter-tester precision was slightly lower than the intra-tester precision for Tester 2, with highest inter-tester variability in the frontal plane angle of Cub:Calc (7.1° RMS-SD) and the frontal plane angle of Nav:Tal (6.1° RMS-SD). For both testers, precision values between manual placement of landmarks and the atlas-based automated method of

landmark placement were comparable to intra-tester precision. The average RMS-SD

values between Tester 1 and the automated method (2.7°) were lower than the average

RMS-SD values between Tester 1 and Tester 2 (3.7°).

Table 4.3: Root-mean square standard deviations (degrees) in sagittal (α), frontal (β), and transverse (γ) bone-to-bone orientation angles for manual and automated anatomical landmark placement.

	Intra-tester RMS-SD (°)		Inter-tester RMS-SD (°)		
	Tester 1	**Tester 2**	**Tester 1 *vs* Tester 2**	**Tester 1 *vs* Auto**	**Tester 2 *vs* Auto**
Sagittal plane (α)					
Cuboid:Calcaneus	1.9°	3.4°	2.0°	2.1°	2.4°
Talus:Calcaneus	3.3°	3.7°	4.4°	2.3°	5.9°
Navicular:Talus	3.6°	5.7°	3.5°	3.5°	3.3°
Navicular:Calcaneus	2.4°	5.9°	5.1°	2.3°	4.9°
Frontal plane (β)					
Cuboid:Calcaneus	2.9°	6.1°	7.1°	4.4°	6.4°
Talus:Calcaneus	1.9°	3.1°	2.7°	3.0°	3.3°
Navicular:Talus	2.3°	4.7°	6.1°	1.3°	6.2°
Navicular:Calcaneus	2.7°	5.6°	4.9°	3.3°	6.0°
Transverse plane (γ)					
Cuboid:Calcaneus	1.7°	2.7°	1.6°	2.9°	3.9°
Talus:Calcaneus	1.4°	2.4°	1.5°	2.7°	2.9°
Navicular:Talus	1.6°	2.9°	2.4°	2.4°	3.8°
Navicular:Calcaneus	2.1°	3.1°	2.8°	2.7°	3.8°

4.5   DISCUSSION

In this study, 3D angular precision was computed for two expert testers and an automated template method to determine anatomically-relevant bone orientations from vQCT scans of the foot. In contrast to previous 3D imaging methods to define foot bone orientation axes using the shape-dependent bone inertial axes (Woodburn *et al.*, 2002; Ledoux *et al.*, 2006), the methods presented here define 3D bone axes using anatomical landmarks, which provides added clinical relevance.

Intra-tester angular precision averaged 2.3° and 4.1° for the two expert testers, and inter-tester angular precision averaged 3.7°. Thus, the present study suggests that atlas-based automated landmark methods can replicate landmark locations with equivalent precision as an expert tester. Moreover, these precision results are comparable to uni-planar radiographic precision (Hastings *et al.*, 2011) and have the advantage of providing a full 3D representation of static bone-to-bone angles, especially in the frontal plane and for bone-to-bone angles that are obscured during planar X-rays. To achieve the level of intra-tester and inter-tester precision observed in this study, the testers required roughly 6-8 minutes *per bone* in order to manipulate bone surface maps within the graphical user interface and place landmarks. The automated method results in equivalent angular precision with negligible processing time, thus an additional advantage of the atlas-based automated method is a significant time savings.

The variability observed in bone-to-bone orientation angles can likely be improved by assessing which individual landmarks had the highest spatial variability (Brown *et al.*, 2009). Results from the present study would suggest that the atlas-based automated landmark method can replicate landmarks with equivalent or superior

precision as an expert tester, and future studies are readily adaptable to using different definitions of bone axes, especially if a landmark position with higher test-retest precision can be adopted. A possible long-term improvement may follow techniques of optoelectronic motion capture by choosing the most reliable anatomical landmarks, then creating virtual landmarks to define bone axes in the most anatomically relevant manner. Doing so could maximize both angular precision and clinical relevance.

One potential limitation of the present study is that the 3D bone-to-bone orientation methods utilize vQCT, which imparts a low amount of radiation to the subject. Future research may replicate these methods using non-radiating 3D imaging modalities such as MRI, which would help extend the technique's utility to pediatric populations with foot deformities such as club foot in individuals with cerebral palsy. Additionally, future application of these methods may extend to clinical populations who experience foot and ankle deformity, such as rheumatoid arthritis, diabetic neuropathy (including Charcot neuroarthropathy), and Charcot-Marie-Tooth disease, or to quantify joint motions using vQCT-derived bone orientations co-registered to multi-plane fluoroscopy.

CHAPTER 5

Effects of Charcot neuropathic osteoarthropathy on three-dimensional foot bone-to-bone orientation angles measured using quantitative computed tomography

Authors: David J. Gutekunst, Lu Liu, Tao Ju, Fred W. Prior, Mary K. Hastings, and David R. Sinacore

5.1   INTRODUCTION

As noted in Chapters 1 and 3, the etiology of Charcot neuropathic osteoarthropathy (CN) remains incompletely understood, but is likely due to focal bone loss and pedal joint mal-alignment (Sinacore *et al.*, 2008; Armstrong *et al.*, 1997) which, in the presence of peripheral neuropathy, can lead to repetitive unperceived trauma during weight-bearing. Bone injury and subtle articular damage characteristic of incipient CN are difficult to visualize with planar radiographs (Yu and Hudson, 2002). As a result, CN often progresses until more serious, clinically obvious events occur. Even when CN is diagnosed early, X-ray measures such as cuboid height, calcaneal pitch, and Meary's angle are abnormal at baseline and continue to worsen over time (Hastings *et al.*, 2012).

Increasingly, 3D imaging has been used to measure foot morphology in neuropathy and overcome inherent limitations of X-ray, such as obscured views and out-of-plane rotations. Hammer toe deformity of the first three rays has been shown to predict high peak plantar pressures under the metatarsal heads (Mueller *et al.*, 2003; Robertson *et al.*, 2002), though it should be noted that these studies utilized uni-planar reconstructions of vQCT images, and it is unknown whether full volume-rendered vQCT images will yield even more diagnostic information. Techniques such as those described in the previous chapter utilize the full ability of vQCT to measure joint angles and quantify structural morphology in all three anatomical planes, including the frontal plane (Ledoux *et al.*, 2006).

Early recognition and quantification of evolving foot mal-alignments is important because if left unchecked, CN mal-alignments may consolidate into fixed foot deformities as the initial inflammatory phase of CN subsides. Fixed foot deformities lead

to elevated peak plantar pressure (Armstrong and Lavery, 1998) , which has been linked to neuropathic foot ulcers retrospectively (Stokes *et al.*, 1975; Boulton *et al.*, 1983; Armstrong *et al.*, 1998b) and prospectively (Lavery *et al.*, 2003; Veves *et al.*, 1992). Elevated plantar pressure has also been identified as a factor contributing to prolonged healing time and higher risk of re-ulceration (Armstrong *et al.*, 1998a). Applying 3D techniques to measure foot bone and joint orientations in individuals with neuropathic foot deformities may aid in diagnosis, surgical treatment, and rehabilitation.

The purpose of this study was to use the atlas-based, automated vQCT methods described in the previous chapter to characterize 3D bone and joint mal-alignments in subjects with acute CN compared to two control cohorts: a matched group of non-CN individuals with DM and PN, and a unimpaired control (UC) group without DM, PN, or any pathology of the foot and ankle. Primary hypotheses were that the atlas-based, automated vQCT technique would confirm mal-alignments observed in CN using uni-planar (lateral) X-rays. Specifically, it was hypothesized that the sagittal plane bone orientation angles of CN subjects would have decreased cuboid height, decreased calcaneal pitch (i.e. a less dorsiflexed calcaneus), increased talar declination angle (i.e. a more plantarflexed talus), and decreased Meary's angle (i.e., increased dorsiflexion of Met1 with respect to Talus). The secondary hypothesis was that there would be additional group differences in hindfoot and lesser tarsal bones and hindfoot:forefoot coupling, including frontal plane mal-alignments that are undetectable using X-rays.

5.2   MATERIALS AND METHODS

5.2.1   Subjects

Subjects recruited into the CN and DM+PN groups were identical to those studied in the project described in Chapter 3. Additionally, 16 UC individuals without DM or PN agreed to participate and provided written informed consent in accordance with the guidelines of the Institutional Review Board and the Human Research Protection Office at Washington University School of Medicine. Six individuals in the CN group (2 females, 4 males) were excluded from the analysis due to severe joint inflammation and bone resorption in the CN-Involved foot that prevented bone segmentation processing and assessment of foot bone orientations. Demographic data for the 14 remaining CN subjects, 20 DM+PN subjects, and 16 UC subjects are presented in Table 5.1.

Table 5.1: Demographic and physical information for bone orientation comparisons.

	DM+PN	*CN*	*UC*
N	20	14	16
Sex (F/M)	11/9	8/6	8/8
Ethnicity	13 White 7 African-American	11 White 3 African-American	12 White 1 African-American 1 Indian-American 2 Asian-American
Age (years)	57.6 ± 10.8	55.1 ± 10.3	27 ± 5.0
Height (cm)	171.7 ± 8.4	174.4 ± 7.8	173.0 ± 11.0
Mass (kg)	94.9 ± 25.7	108.9 ± 26.0	76.5 ± 18.1
Body mass index (kg/m^2)	32.0 ± 8.1	35.6 ± 8.0	25.3 ± 4.4
Diabetes Type (Type1/Type2)	2/18	1/13	n/a
HbA1c (%)	7.8 ± 1.4	7.7 ± 1.6	n/a
DM duration (years)	13.9 ± 12.6	18.4 ± 11.1	n/a
PN duration (years)	5.2 ± 3.5	7.3 ± 4.6	n/a

5.2.2   Bone-to-bone 3D orientation angles

vQCT scan parameters and bone segmentation processing were completed as summarized in Section 3.3.2 and described in detail in previous publications (Liu *et al.*, 2008; Commean *et al.*, 2011; Commean *et al.*, 2009). The resulting segmented bone object maps and grayscale voxel datasets were imported into the custom Bone Measurement Tool (Liu *et al.*, 2012). Anatomical landmarks used to define the bone orientation axes for the calcaneus, talus, cuboid, and navicular followed the conventions

described in Section 4.3.3 and shown in Table 4.1, Table 4.2, and Figure 4.1.

Additionally, the embedded template bone atlas was expanded to include anatomical

landmarks for the remaining 3 tarsals (the cuneiform bones) and the 5 metatarsals. This

expanded landmark template included a total of 47 anatomical landmarks to describe the

3D orientations of all 7 tarsal and 5 metatarsal bones, as shown in Figure 5.1 below.
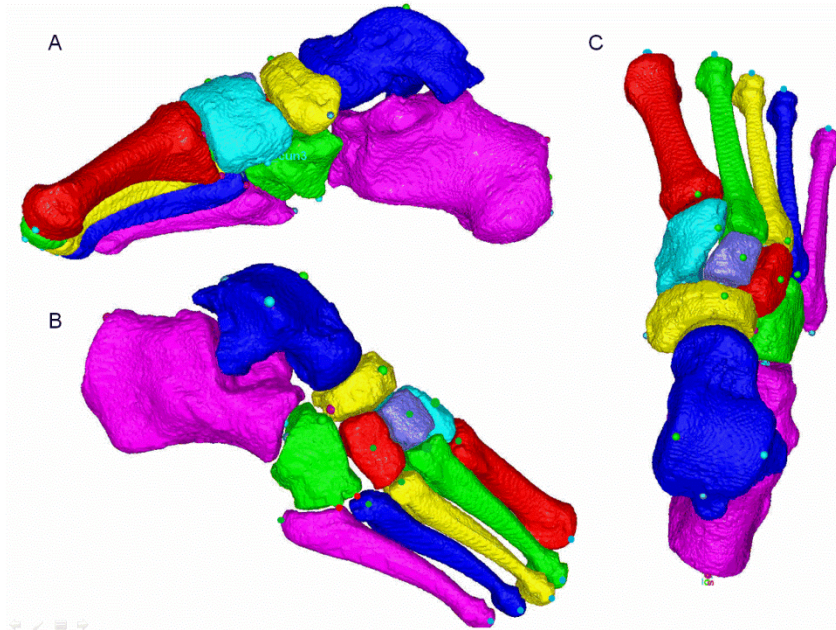
Figure 5.1: Atlas-based automated anatomical landmarks for all 7 tarsal and 5 metatarsal bones in (A) medial view, (B) oblique view, and (C) anterior-posterior view

Anatomical landmarks on the calcaneus, Met5, and Met2 were used to define

orientation axes for the foot as a whole. Whereas sagittal plane weight-bearing X-rays

allow measurement of bone positions and angles with respect to the horizontal axis

(Figure 5.2), the non-weight-bearing vQCT scans do not provide a true set of reference

coordinate axes.
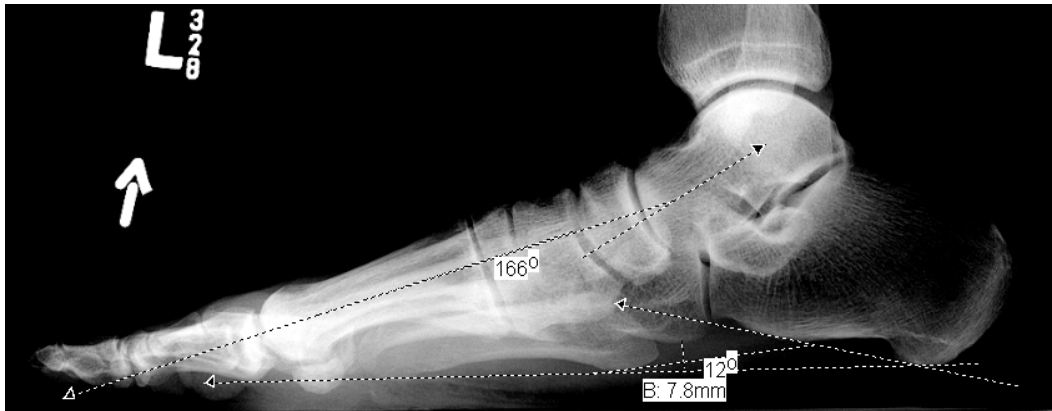
Figure 5.2: Sagittal plane X-ray showing cuboid height, calcaneal pitch, talar declination, Meary's angle, and Hibbs' angle. *(X-ray measurements courtesy of Mary Hastings, PT, DPT)*

To replicate X-ray measures such as cuboid height, calcaneal pitch, or talar declination, as well as bone-to-bone X-ray measures of Meary's angle (Met1 with respect to talus) or Hibbs' angle (Met1 with respect to calcaneus), a non-weight-bearing vQCT method requires the definition of local coordinate axes for the foot as a whole, including a definition of the horizontal plane beneath the plantar surface of the foot. The coordinate axes defined by the inferior calcaneus landmark and the anterior landmarks on Met2 and Met5 were used to create a 3D frame of reference to replicate X-ray measures such as cuboid height (Figure 5.3) and calcaneal pitch, talar declination, Meary's angle, and Hibbs' angle (Figure 5.4). The anatomical landmarks used to define the coordinate axes of Met1, Met5, and the foot segment are shown in Figure 5.4. Landmark descriptions are in Table 5.2; bone orientation definitions are in Table 5.3. An added benefit of the 3D vQCT method is the ability to make angular measurements of these bones in the frontal and transverse planes.
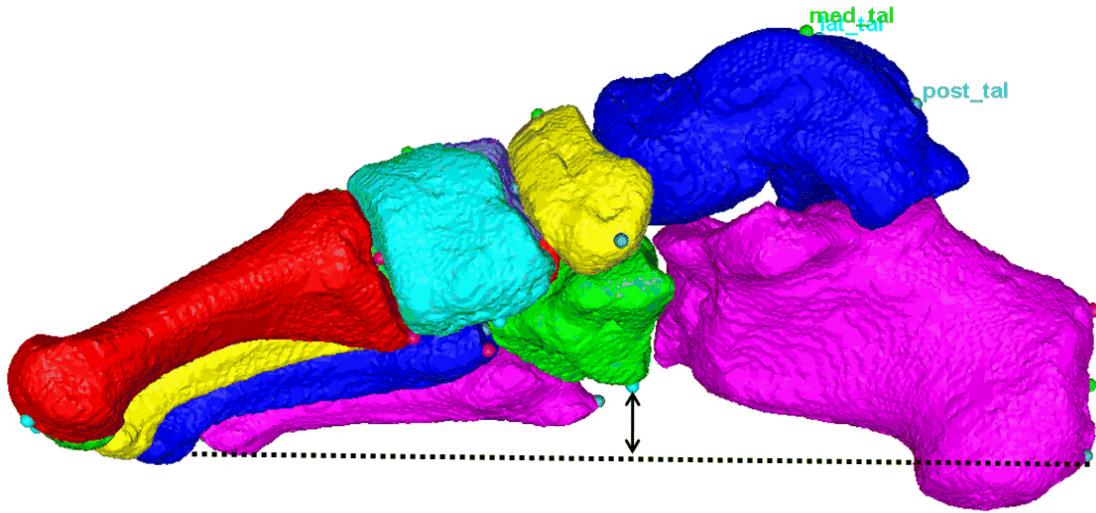
Figure 5.3: Landmark-based definition of the foot segment axes to measure cuboid height.
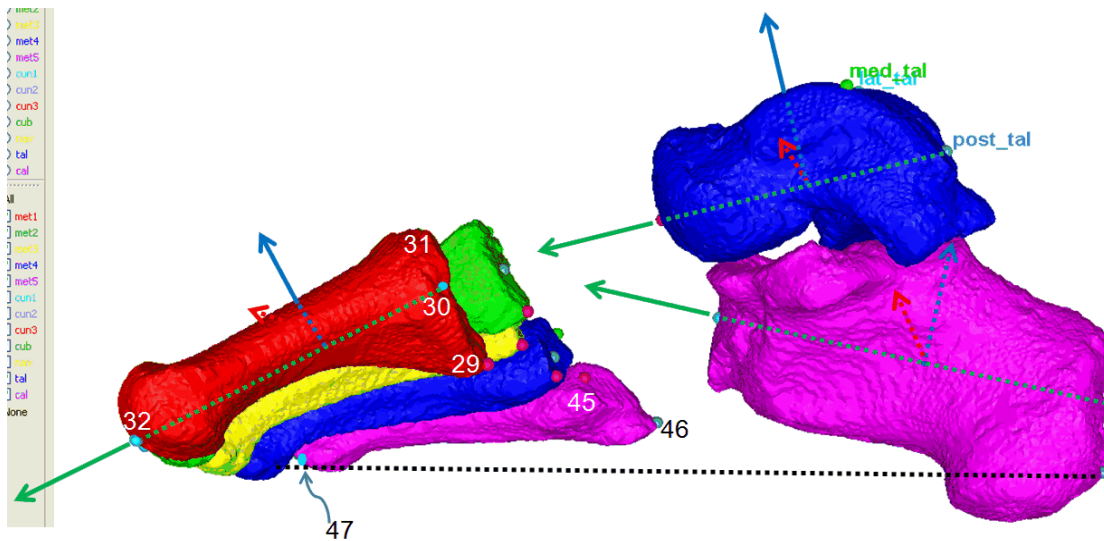
Figure 5.4: Landmark-based definition of the foot segment axes to measure calcaneal pitch, talar declination, Meary's angle, and Hibbs' angle.

Table 5.2: Anatomic landmarks for Met1, Met5, and the foot segment.

Bone	Landmarks	Description
Met1	29. Inferior	Medial-lateral midline of Metatarsal 1, along inferior edge of base
	30. Posterior	Medial-lateral midline of Metatarsal 1 base, bisecting shaft in sagittal plane when connected to anterior landmark
	31. Superior	Medial-lateral midline of Metatarsal 1, along superior edge of base
	32. Anterior	Central aspect of distal head of Metatarsal 1
Met5	45. Medial	Medial edge of the base of Metatarsal 5
	46. Lateral	Lateral edge of the base of Metatarsal 5
	47. Anterior	Central aspect of distal head of Metatarsal 5
Foot segment	3. Inferior calcaneus	Medial-lateral midline of calcaneus posterior facet, along the inferior border.
	36. Anterior Met2	Central aspect of distal head of Metatarsal 2
	47. Anterior Met5	Central aspect of distal head of Metatarsal 5

Table 5.3: Metatarsal and foot orientation definitions based on anatomical landmarks (right foot).

Bone	First axis	Temporary axis	Second axis	Third axis
Metatarsal 1	$Y_{Met1} = \lvert 30 \rightarrow 32 \rvert$	$t_{Met1} = \lvert 29 \rightarrow 31 \rvert$	$X_{Met1} = Y_{Met1} \times t_{Met1}$	$Z_{Met1} = X_{Met1} \times Y_{Met1}$
Metatarsal 5	$Y_{Met5} = \lvert 45 \rightarrow 46 \rvert$	$t_{Met5} = \lvert 45 \rightarrow 47 \rvert$	$Z_{Met5} = t_{Met5} \times Y_{Met5}$	$X_{Met5} = Y_{Met5} \times Z_{Met5}$
Foot segment	$Y_{foot} = \lvert 3 \rightarrow 36 \rvert$	$t_{foot} = \lvert 3 \rightarrow 47 \rvert$	$Z_{Foot} = t_{foot} \times Y_{foot}$	$X_{foot} = Y_{foot} \times Z_{foot}$

The following bone-to-bone and bone-to-foot orientation angles were compared between the CN, DM+PN, and UC groups:

Hindfoot and lesser tarsal bone-to-bone angles:

- Cuboid with respect to calcaneus (Cub:Calc)

- Talus with respect to calcaneus (Tal:Calc)

- Navicular with respect to calcaneus (Nav:Calc)

- Navicular with respect to talus (Nav:Tal)

Hindfoot:forefoot angles:

- First metatarsal with respect to talus (Met1:Tal)

- First metatarsal with respect to calcaneus (Met1:Calc)

Hindfoot:foot segment angles:

- Calcaneus with respect to whole-foot segment (Calc:Foot)

- Talus with respect to whole-foot segment (Tal:Foot)

For all bone-to-bone and bone-to-foot angles, a Cardan rotation sequence of XY'Z" was computed to reflect the sagittal (α), frontal (β), and transverse (γ) plane rotations of the distal segment with respect to the proximal segment. Additionally, cuboid height was measured as the distance between the XY plane of the whole-foot segment and the position of the inferior cuboid anatomical landmark (Figure 5.3). (Mathematically, cuboid height was computed as the dot product between the Z-axis unit vector of the whole-foot segment and the vector connecting the inferior calcaneus landmark to the inferior cuboid landmark.)

5.2.3 Statistical Analyses

Subject sex, ethnicity, and DM type were compared among the groups using chi-square tests. Age, height, weight, body mass index, DM duration, and PN duration were compared using the Student's t-test. For each bone-to-bone orientation angle, a two-way ANOVA was used to test the effects of Group and Foot. For CN subjects, foot was coded as involved (CN-Inv) or uninvolved (CN-Uninv). In DM+PN and UC subjects, neither foot was affected by CN, but for statistical comparisons between the two groups it was necessary to designate one foot per subject as "involved." The right feet of DM+PN and UC subjects were arbitrarily designated as "involved." The hypothesis was that there would be no side-to-side differences in DM+PN or UC subjects, while the CN-Inv feet were hypothesized to have significantly different bone orientation angles compared to CN-Uninv; The significance level was set at $\alpha \leq 0.05$. All statistical analyses were completed in SPSS version 20.0 (IBM Corp., Chicago, IL).

5.3 RESULTS

The CN and DM+PN groups did not differ in any demographic or physical characteristics, though the UC group was significantly younger and had lower mass and BMI (Table 5.1). Control DM+PN and UC subjects had no side-to-side differences for any bone-to-bone orientation angle, thus in Table 5.4 and Table 5.5 the results show these groups averaged across sides.

5.3.1 *Bone-to-bone orientations in the hindfoot and lesser tarsals*

There were no group differences or CN side-to-side differences in any of the bone-to-bone orientation angles in the hindfoot and lesser tarsals. Group averages for the relative angle of Cub:Calc ranged from 40-46° of cuboid plantarflexion with respect to calcaneus, 4-6° of relative eversion, and from 3° of adduction to 3° of abduction. Tal:Calc angles showed low variability across groups: 34-37° of talar plantarflexion, 2-7° of eversion, and 12-14° of adduction with respect to calcaneus.

5.3.2 *Orientations of hindfoot bones to the whole-foot segment*

The sagittal plane rotation of Calc:Foot, which represents the 3D Cardan equivalent of calcaneal pitch measured using lateral X-ray, showed a 7° reduction in calcaneal dorsiflexion in the CN-Inv feet compared to DM+PN controls (p=0.023), and a 9° reduction compared to the UC group (p<0.01) (Table 5.4). The control subjects had no side-to-side differences in sagittal Calc:Foot angle, with a mean difference of 0.3° in UC and 0.4° in DM+PN. The CN-Inv feet had significantly lower calcaneal pitch than the CN-Uninv feet (mean difference = 3.4°, p<0.01). In the frontal plane, the calcaneus was more everted in the CN-Inv feet compared to the CN-Uninv (p=0.015) and DM+PN (p=0.040) feet, with a trend toward significantly greater eversion in CN-Inv feet compared to UC (p=0.065).

In the CN-Inv feet, the talus showed significantly greater talar declination (plantarflexion) angle, as measured by the sagittal plane rotation between talus and the whole-foot segment. The CN-Inv feet had roughly 3° more relative talar plantarflexion compared to the CN-Uninv feet (p=0.015), whereas in the DM+PN and UC subjects the

mean side-to-side differences were 0.5° and 0.8°, respectively (both non-significant). The CN-Inv feet had roughly 5° more relative talar plantarflexion compared to the DM+PN group (p=0.010) and 4° more talar plantarflexion than the UC group (p=0.037). There were no group or CN side-to-side differences in the frontal plane or transverse plane angles of Tal:Foot.

Cuboid height was significantly lower in CN-Inv feet compared to UC feet, with a mean difference of almost 6mm (p=0.019). There was a trend for lower cuboid height in CN-Inv compared to DM+PN and compared to CN-Uninv feet (both p=0.08).

5.3.3   *Hindfoot to forefoot bone orientation angles*

CN-Inv feet had a less dorsiflexed, more inverted orientation of the first metatarsal with respect to talus (Met1:Tal). The UC, DM+PN, and CN-Uninv feet had 12-14° of Met1 plantarflexion with respect to talus, whereas the CN-Inv feet had 5° of plantarflexion (Table 5.4). The CN-Inv feet had significantly lower plantarflexion of Met1 compared to the UC feet (p=0.025) with a trend towards lower plantarflexion compared to DM+PN (p=0.053). There were no side-to-side differences in the UC and DM+PN groups, whereas in CN subjects there was a roughly 7° reduction in relative Met1 plantarflexion in the CN-Inv feet compared to the CN-Uninv feet (p<0.01). In the frontal plane, the CN-Inv feet had roughly 6° of Met1:Tal inversion compared to 0-2° of eversion in the CN-Uninv, DM+PN, and UC feet. The Met1:Tal angles CN-Inv feet were roughly 7.8° more inverted than he UC feet (p<0.01), 6.5° more inverted than DM+PN (p=0.022), and 7.2° more inverted than CN-Uninv feet (p<0.001).

The 3D Cardan equivalent of Hibbs' angle – the sagittal plane angle of Met1:Calc showed a significant reduction in the plantarflexion of Met1 with respect to calcaneus in the CN-Inv feet. Compared to the UC feet, the CN-Inv feet had 8° less Met1 plantarflexion (p=0.039). There was no side-to-side difference in either the DM+PN or UC groups, but there was a 6.4° difference between the CN-Inv and CN-Uninv feet (p<0.01). As in the Met1:Tal orientations, the Met1:Calc frontal plane angle showed a more inverted relative orientation of Met1, with approximately 9° more inversion in CN-Inv compared to CN-Uninv (p<0.001) and 10° more Met1 inversion compared to UC (p=0.003) and 11° more Met1 inversion compared to DM+PN (p<0.001).

Table 5.4: Group means ± standard deviations (degrees) for hindfoot sagittal (α), frontal (β), and transverse (γ) bone-to-bone orientation angles. Sign convention: +α = dorsiflexion of distal segment, +β = inversion of distal segment, +γ = adduction of distal segment.

	UC	DM+PN	CN-Uninvolved	CN-Involved
Cuboid:Calcaneus				
Sagittal plane (α)	-42.4 ± 5.9°	-40.3 ± 10.3°	-46.3 ± 5.9°	-44.2 ± 10.1°
Frontal plane (β)	-4.5 ± 5.7°	-6.0 ± 7.4°	-4.9 ± 7.4°	-5.3 ± 6.2°
Transverse plane (γ)	-3.1 ± 5.4°	-3.0 ± 6.4°	-1.4 ± 8.5°	3.3 ± 20.1°
Talus:Calcaneus				
Sagittal plane (α)	-36.7 ± 4.0°	-34.0 ± 6.7°	-35.9 ± 4.2°	-35.1 ± 7.0°
Frontal plane (β)	-3.2 ± 5.0°	-6.7 ± 5.8°	-2.3 ± 6.0°	-1.6 ± 7.3°
Transverse plane (γ)	11.7 ± 3.1°	12.3 ± 4.8°	12.8 ± 3.6°	14.1 ± 7.1°
Navicular:Talus				
Sagittal plane (α)	-19.6 ± 4.5°	-18.5 ± 6.4°	-21.1 ± 4.4°	-16.5 ± 11.2°
Frontal plane (β)	-10.6 ± 4.5°	-8.8 ± 7.8°	-10.3 ± 7.3°	-9.6 ± 9.4°
Transverse plane (γ)	0.5 ± 5.1°	2.4 ± 9.4°	3.1 ± 9.6°	-0.7 ± 11.5°
Navicular:Calcaneus				
Sagittal plane (α)	-54.2 ± 5.1°	-50.6 ± 9.0°	-54.2 ± 5.8°	-49.0 ± 12.7°
Frontal plane (β)	-17.3 ± 5.6°	-18.3 ± 7.4°	-16.9 ± 4.7°	-14.5 ± 11.2°
Transverse plane (γ)	10.9 ± 6.1°	12.6 ± 6.8°	14.9 ± 8.2°	12.5 ± 9.5°

Table 5.5: Mean ± standard deviation (degrees) for sagittal (α), frontal (β), and transverse (γ) bone-to-bone orientation angles. Sign convention: +α = dorsiflexion of distal segment, +β = inversion of distal segment, +γ = adduction of distal segment. For CN-Involved data, *a* = significant difference from UC group; *b* = significant difference from DM+PN group, and *c* = significant difference from CN-Uninvolved feet.

	UC	**DM+PN**	**CN-Uninvolved**	**CN-Involved**
Cuboid Height (mm)	9.6 ± 4.2	8.2 ± 6.5	6.1 ± 7.7	3.8 ± 8.2 *a*
Calc:Foot angle				
Sagittal plane (α) *(Calcaneal pitch)*	21.3 ± 3.0°	20.1 ± 5.9°	18.6 ± 5.8°	15.1 ± 7.6° *a,b,c*
Frontal plane (β)	-10.6 ± 6.5°	-10.9 ± 5.0°	-11.6 ± 5.9°	-16.7 ± 6.8° *b,c*
Transverse plane (γ)	-11.5 ±3.2 °	-12.0 ± 3.8°	-14.3 ± 6.7°	-12.4 ± 5.3°
Met1:Talus angle				
Sagittal plane (α) *(Meary's Angle)*	-13.7 ± 5.7°	-12.4 ± 8.1°	-12.2 ± 9.4°	-5.1 ± 12.1° *a,b,c*
Frontal plane (β)	-1.9 ± 6.2°	0.2 ± 7.0°	-1.6 ± 9.2°	5.6 ± 10.9° *a,b,c*
Transverse plane (γ)	14.1 ± 6.7°	14.4 ± 8.2°	17.7 ± 11.6°	14.9 ± 11.4°
Met1:Calc angle				
Sagittal plane (α) *(Hibbs' angle)*	-49.6 ± 6.2°	-46.0 ± 9.8°	-47.2 ± 9.7°	-40.8 ± 13.7° *a,c*
Frontal plane (β)	-7.7 ± 7.0°	-8.2 ± 6.9°	-6.4 ± 7.3°	2.5 ± 11.9° *a,b,c*
Transverse plane (γ)	24.8 ± 6.6°	25.3 ± 5.9°	29.6 ± 10.8°	28.1 ± 10.4°
Talus:Foot angle				
Sagittal plane (α)	-15.4 ± 3.0°	-14.8 ± 5.0°	-16.6 ± 5.7°	-19.4 ± 5.5° *a,b,c*
Frontal plane (β)	-4.8 ± 5.8°	-8.5 ± 6.8°	-3.4 ± 7.7°	-7.2 ± 8.8°
Transverse plane (γ)	-3.9 ± 5.1 °	-3.8 ± 6.7°	-5.6 ± 6.7°	-4.6 ± 7.1°

5.4 DISCUSSION

This study sought to quantify the effects of acute CN on 3D foot bone-to-bone orientation angles using a novel vQCT, atlas-based, anatomical landmarking method. In contrast to X-ray methods to assess foot deformities, the vQCT permits full description of bone-to-bone orientations in all 3 dimensions; in contrast to previous 3D imaging methods to define foot bone orientation axes, the results presented here are based on anatomically-relevant 3D bone axes rather than shape-dependent inertial axes (Woodburn *et al.*, 2002; Ledoux *et al.*, 2006).

As hypothesized, there were numerous findings using the atlas-based anatomical landmark method that confirm recent results from an X-ray analysis of CN foot deformities (Hastings *et al.*, 2012). As in the X-ray analyses, the 3D vQCT results show a reduction in the calcaneal pitch in CN-Inv feet (Hastings *et al.*, 2012), though the present study also presents the novel finding of increased calcaneal eversion in CN-Inv feet, which is consistent with a collapse of the medial longitudinal arch. Similarly, the vQCT method confirmed X-ray findings of increased talar declination, decreased cuboid height, and increased dorsiflexion of Met1 with respect to talus (Hastings *et al.*, 2012), while also showing that Met1 is more inverted with respect to talus. This increased Met1 inversion is a frontal plane rotation that cannot be detected using X-ray methods. The vQCT method also produced the novel finding of a reduction in the 3D equivalent of Hibbs' angle (the sagittal plane angle of Met1:Calc), which further supports the interpretation of the CN-Inv feet having a general, multi-joint collapse of the medial longitudinal arch. In the frontal plane, Met1 was more inverted in the CN-Inv feet than the matched CN-Uninv feet or either control group, which could not be measured using

uni-planar X-rays. The increased relative dorsiflexion and inversion of Met1 with respect to both talus and calcaneus may also lead to hallux valgus, which has been shown to be related to increased plantar pressure under the first metatarsal head (Mueller *et al.*, 2003). However, the current vQCT method did not include the phalanges, which would allow assessment of hallux valgus and also hammer toe deformity. Future atlas-based vQCT foot deformity assessment may include the phalanges to further expand the ability to detect deformities leading to plantar ulceration and/or Charcot progression.

The atlas-based vQCT method is not without limitations. The vQCT scans were recorded with subjects in a non-weight-bearing posture, thus the results presented here may not represent the bone orientation angles that would be observed during standing. However, it is likely that the deformities shown in non-weight-bearing would only be more pronounced during weight-bearing, meaning that it is unlikely that the significant findings presented here would persist. Future research using the atlas-based vQCT method will include partial weight-bearing as performed previously by our lab (Smith *et al.*, 2000; Smith *et al.*, 2001) with modifications of the foot loading fixture to allow simultaneous measurement of BMD and bone strength indices such as those described in Chapters 2 and 3. Future investigations may also utilize MRI scans to produce segmented bone object maps, which could be used in a similar manner in the atlas-based Bone Measurement Tool to produce anatomically-relevant bone orientation angles.

In conclusion, this study has presented results showing foot deformities in three dimensions, defined using anatomically-relevant bone orientation axes that mimic established orthopedic measures used previously in uni-planar X-rays. This study has the potential to improve the ability of surgeons, podiatrists, and rehabilitation specialists to

diagnose and quantify evolving foot mal-alignments in individuals at risk of developing more serious fixed foot deformities. Future work will assess the time course of foot morphological changes in the Charcot foot, and attempt to identify deformity-based biomarkers that may identify individuals with DM and PN who are at risk of developing CN.

CHAPTER 6

Summary and Conclusions

The goal of this dissertation research has been to use vQCT to assess foot bone strength and foot deformity as indices of CN development and progression. In the process of developing and validating these measures of bone strength and foot deformity, we have built tools that will be used in future research spanning orthopedic biomechanics, physical therapy, and radiology.

A key finding of Aim 1 (Chapter 2) was that metatarsal BMD and bone geometric strength indices derived from vQCT scans are highly correlated to ultimate loading in *ex vivo* materials testing. The methods we utilized to measure BMD and the strength indices were directly applicable to *in vivo* testing, as we performed vQCT scanning using intact cadaver lower-extremity specimens before excising the metatarsals and performing maximal monotonic loading. Previously, all studies of metatarsal bone strength (Courtney *et al.*, 1997; Fleischli *et al.*, 1998; Lidtke *et al.*, 2000; Muehleman *et al.*, 2000) have utilized methods that are not applicable to *in vivo* testing. In addition, the methods developed in Aim 1 showed that a novel density-weighting procedure may result in bone geometric strength indices that have greater predictive capacity for ultimate bone strength. Current vQCT technology invariably leads to some spatial averaging of bone and non-bone material, meaning that previous assessments may have inherent imprecision in their estimates of geometric strength parameters. Our method provides improved *density resolution* to help counteract the limitations in vQCT *spatial resolution*.

Having shown strong correlations between vQCT-derived geometric strength indices and *ex vivo* ultimate loads in Aim 1, we then applied the vQCT methods to individuals with acute CN in order to test whether these individuals have reduced geometric strength indices. Surprisingly, we found that while BMD was significantly lower in CN individuals throughout the diaphysis of the Met2 and Met5 compared to matched subjects with DM and PN, bone geometric strength indices such as Ct.Ar, S_{min}, and Ct.Th were maintained or increased in CN subjects. While unexpected, this finding may reflect inflammatory damage to CN bones rather than a true maintenance of bone strength. The work done in Aims 1 and 2 contributed directly to a successful grant application (NICHD R03 HD068660) that will allow future investigation with µCT to assess whether the periosteal expansion observed using vQCT reflects apposition of cortical bone, or if it may reflect incompletely mineralized woven bone that was deposited in response to bone injury.

Aim 3 (Chapter 4) involved methodological development and reliability assessment of novel 3D methods to assess foot deformities. We sought to mimic established X-ray measures of deformity by producing anatomically-relevant 3D foot bone orientation axes. Intra- and inter-tester reliability was comparable to uni-planar measures from X-ray, and agreement between expert testers and a fully automated method of placing anatomical landmarks using an atlas-based landmark template. Aim 4 (Chapter 5) then applied the atlas-based automated method to compare 3D foot bone orientations in subjects with acute CN to control groups of matched DM+PN subjects and unmatched, unimpaired subjects. The results confirmed recent X-ray findings of foot deformities in acute CN, and also provided novel information regarding bone deformities

in the frontal plane. These 3D foot deformity measures may provide important indices of CN development, progression, and future risk of ulceration and neuropathic fracture, and in particular the frontal plane orientation angles are not possible to measure using X-ray.

An example of possible future directions utilizing the techniques described in this dissertation is provided in Appendix B. Two case reports over a 12-month period are presented of subjects in the CN group who experienced mid-diaphyseal fracture of Met5 between 6 and 12 months after enrollment in our study. At enrollment and 3, 6, and 12 months post-enrollment, the subjects underwent vQCT scans and plantar pressure assessment. Our results showed that while both subjects presented with low values for metatarsal BMD and bone geometric strength indices, between enrollment and the 6 month follow-up test their BMD and geometric indices declined slightly at 3 months and then rebounded to baseline levels by 6 months. Thus, the fractures that occurred between 6 months and 12 months post-enrollment were not preceded by further reductions in our measures of bone strength. However, during the period preceding fracture, both subjects experienced increases in peak plantar pressure and maximum force recorded during barefoot walking in their lateral midfoot region (including the base and head of Met5). Thus, while BMD and bone strength indices did not decrease, the loads applied to the lateral column bones did increase. Furthermore, our measures of foot deformity – specifically, bone-to-bone orientation angles of the lateral metatarsals with respect to the calcaneus – showed evidence of evolving equinovarus foot deformity which help explain the higher biomechanical loads. So, in summary, the tools developed during this dissertation have immediate utility in understanding risk for deleterious sequelae of CN, such as metatarsal fracture.

In conclusion, the research presented in this dissertation, undertaken as an interdisciplinary effort among physical therapists, biomedical engineers, radiologists, and orthopedic surgeons, provides new information regarding bone strength and foot deformities in Charcot neuropathic osteoarthropathy. Moreover, the tools developed to conduct this research will lead to future research and new insights on the pathophysiological pathways linking diabetes, peripheral neuropathy, foot deformities, and the development and progression of Charcot neuropathic osteoarthropathy.

Appendix A: Calculations for areal and density-weighted bending strength indices: moment of inertia (I_{min}, I_{max}) and section modulus (S_{min}, S_{max}).

Step 1: determine center of mass (COM) positions for each cross-sectional

slice. <u>Areal bending strength indices:</u>   <u>Density-weighted bending strength indices:</u>

$$X_{COM} = \frac{\sum_i (x_i * A_i)}{\sum_i A_i} \qquad\qquad X_{COM} = \frac{\sum_i (x_i * BMD_i * A_i)}{\sum_i BMD_i * A_i}$$

$$Y_{COM} = \frac{\sum_i (y_i * A_i)}{\sum_i A_i} \qquad\qquad Y_{COM} = \frac{\sum_i (y_i * BMD_i * A_i)}{\sum_i BMD_i * A_i}$$

Step 2: determine moments of inertia (I) using the X-Y axes for each cross-sectional slice.

<u>Areal bending strength indices:</u>   <u>Density-weighted bending strength indices:</u>

$$I_{xx} = \sum (Y_i - Y_{COM})^2 * A_i \qquad\qquad I_{xx} = \sum_i (Y_i - Y_{COM})^2 * BMD_i * A_i$$

$$I_{yy} = \sum_i (X_i - X_{COM})^2 * A_i \qquad\qquad I_{yy} = \sum_i (X_i - X_{COM})^2 * BMD_i * A_i$$

$$I_{xy} = \sum_i (X_i - X_{COM})(Y_i - Y_{COM}) * A_i \qquad I_{xy}I_{xy} = \sum_i (X_i - X_{COM})(Y_i - Y_{COM}) * BMD_i * A_i$$

Step 3: compute minimum (I_{min}) and maximum (I_{max}) moments of inertia from I_{xx}, I_{yy}, and I_{xy}:

$$I_{max,min} = \frac{I_{xx} + I_{yy}}{2} \pm \sqrt{\left(\frac{I_{xx} - I_{yy}}{2}\right)^2 + I_{xy}^2}$$

Step 4: calculate the minimum (S_{min}) and maximum (S_{max}) section moduli from I_{min}, I_{max}, and the periosteal radius (R_o).

$$S_{min} = \frac{I_{min}}{R_o} \qquad\qquad\qquad S_{max} = \frac{I_{max}}{R_o}$$

Appendix B.

Two case reports of pedal bone quantity, geometric strength

indices, bone-to-bone orientations, and plantar loads preceding

incipient metatarsal fracture

Authors: David J. Gutekunst and David R. Sinacore

Abstract

Study Design: case reports (2)

Background: Charcot neuroarthropathy (CN) is a progressive, non-infective, inflammatory destruction of bones and joints that can lead to progressive foot deformities and plantar ulceration. Though individuals with CN typically have low BMD, little is known regarding changes in BMD, bone quality, joint mal-alignment, and biomechanics preceding fracture.

Case Description: Two females, aged 45 and 54 years at the onset of an acute non-fracture CN event, received regular physical therapy with wound care and off-loading treatment (total contact casting). Both enrolled in a larger research study that included plantar pressure assessment and quantitative computed tomography at enrollment and 3, 6, and 12 months later. Both women sustained new mid-diaphyseal Met5 fracture between 6 and 12 months. Image processing techniques were used to measure BMD, geometric strength indices, and three-dimensional bone-to-bone orientation angles.

Outcomes: Met5 BMD decreased during off-loading treatment from 0-3 months, then rebounded by 6 months. All geometric strength indices improved from baseline through 6 months. Plantar loading in the lateral midfoot increased preceding fracture, concomitant with alterations in bone orientation angles which suggest progressive development of metatarsus adductus and equinovarus foot deformity.

Discussion: Fractures may occur when bone strength decreases or when biomechanical loading increases. Though bone quality was low at baseline, incipient fracture was preceded by increased loading in the lateral midfoot, but not by reductions in BMD or geometric strength indices, suggests that loading played a central role in fracture. Moreover, the progression of foot deformities may be causally linked to the increased plantar loading.

1.   Background

Charcot neuropathic osteoarthropathy (CN) is a progressive, inflammation-mediated destruction of bones and joints leading to fracture, subluxation, and dislocation, which in turn result in progressive foot deformities that increase the risk of plantar ulceration (Frykberg and Belczyk, 2008; Rogers *et al.*, 2011; Thompson, Jr. and Clohisy, 1993). Diabetes mellitus (DM) and peripheral neuropathy (PN) are the most common precursors of CN (Lee *et al.*, 2003). The etiology of CN remains incompletely understood, but is likely due to a combination of repetitive unperceived trauma during weight-bearing, focal bone loss, and pedal joint mal-alignment (Sinacore *et al.*, 2008; Armstrong *et al.*, 1997). Bone injury and subtle articular damage characteristic of incipient CN are difficult to visualize with planar radiographs (Yu and Hudson, 2002). As a result, CN progresses until more serious, clinically obvious events occur.

Previous cross-sectional studies reinforce the importance of bone loss (Sinacore *et al.*, 2008; Bem *et al.*, 2010; Chantelau, 2005), foot deformity (Chantelau, 2005; Cavanagh *et al.*, 1994), and elevated biomechanical loading (Armstrong and Lavery, 1998) in the development and progression of CN. Individuals with acute CN have lower calcaneal BMD than matched non-CN subjects with DM and PN (Sinacore *et al.*, 2008). Moreover, the clinical manifestation of CN may depend upon BMD: pedal fractures predominate in individuals with osteopenia (as measured by dual-energy X-ray absorptiometry at the hip), whereas pedal subluxations and dislocations are more common in those with normal or high BMD (Herbst *et al.*, 2004). Recent advances in vQCT image processing allow direct quantitative measurement of BMD in foot bones. Commean *et al* developed a semi-automated bone segmentation technique to compute bone volumes and BMD for the 7 tarsals and 5 metatarsals with high precision

(Commean *et al.*, 2009; Commean *et al.*, 2011). Still, the importance of BMD as a prospective risk factor for incipient fracture is unclear. At other anatomical sites, bone geometric strength indices have been more highly correlated to fracture risk than has BMD alone (Evans *et al.*, 2008; Brudvig *et al.*, 1983; Kontulainen *et al.*, 2008; Liu *et al.*, 2007; Manske *et al.*, 2006). The *ex vivo* validation of cadaver metatarsals described in Chapter 2 showed that mid-diaphyseal indices of bending strength (minimum moment of inertia, I_{min}, and section modulus, S_{min}) and cortical integrity (Ct.Th and BR) were more highly correlated than BMD to metatarsal breaking loads (Gutekunst *et al.*, 2012). Ultimate force was directly related to I_{min}, S_{min}, and Ct.Th, and inversely related to BR (where BR = periosteal radius divided by Ct.Th).

vQCT has been used increasingly to measure foot morphology in neuropathy. vQCT can overcome inherent limitations of X-ray, such as obscured views and out-of-plane rotations. Hammer toe deformity of the first three rays has been shown to predict high peak plantar pressures under the metatarsal heads (Mueller *et al.*, 2003; Robertson *et al.*, 2002), though these studies utilized planar reconstructions of vQCT images. New techniques take full advantage of the ability of vQCT to measure joint angles and quantify structural morphology in all three anatomical planes, including the frontal plane (Ledoux *et al.*, 2006), but no vQCT study has measured three dimensional (3D) foot bone and joint orientations in individuals with DM, PN, or CN.

Elevated plantar pressure has been linked to neuropathic foot ulcers retrospectively (Stokes *et al.*, 1975; Boulton *et al.*, 1983; Armstrong *et al.*, 1998b) and prospectively (Lavery *et al.*, 2003; Veves *et al.*, 1992), and has been identified as a factor contributing to prolonged healing time and higher risk of re-ulceration (Armstrong *et al.*,

1998a). Fixed foot deformities resulting from CN play a role in many neuropathic ulcers, but even in the absence of ulceration, CN is associated with elevated peak pressure (Armstrong and Lavery, 1998). No previous research has assessed plantar loads over time following an acute CN event, or assessed the relationship between plantar loads and incipient fracture risk.

As part of a prospective study of individuals with acute CN, we assessed plantar pressure and acquired vQCT scans at enrollment and 3, 6, and 12 months later. Image processing techniques were used to measure BMD, bone geometric strength indices, and 3D bone-to-bone orientation angles. Two of the volunteers incidentally experienced mid-diaphyseal fractures of Met5 between 6 and 12 months after study enrollment. These serial data collections allowed a unique prospective assessment of changes in bone strength, foot deformity, and applied loads leading to eventual metatarsal fracture.

2. Description of Cases

Volunteer A is a Caucasian 45 year-old female who was diagnosed with Type 1 DM at age 21. She was diagnosed with PN at age 38 based on clinical evidence of impaired sensation to pressure, vibration, and light touch, and reported regular tingling and numbness in her feet. She had palpable pulses bilaterally in the dorsal pedal and posterior tibial regions. At the time of enrollment, she had plantar flexed first rays and prominent first metatarsal heads bilaterally, and a bunion on the head of the right-side Met5. She had sustained CN-related fractures to Met3, Met4, and Met5 of her left foot one year prior to enrollment in the present study (which prevents use of the left foot as a comparison in this case report). She had prior history of plantar ulceration at the right Met5 and right great toe sulcus, and was receiving offloading and wound care treatments

to heal a plantar ulcer at the base of the left Met5 when a diagnosis was made of an acute CN event located at the right first cuneiform with possible secondary CN in the proximal region of the right Met5.

Volunteer B is a Caucasian 54 year-old female with no prior diagnosis of DM. However, based on her HbAlc values of 5.8%, she would have been identified as pre-diabetic using updated criteria by the American Diabetes Association (2012), and furthermore, she was diagnosed as diabetic at follow-up. Following a fracture of her right cuboid at age 50, she was diagnosed with idiopathic PN based on clinical evidence of bilateral impaired sensation to pressure, vibration, and light touch. She reported painful neuropathy bilaterally in the digits and fore foot region, had palpable pulses bilaterally in the dorsal pedal and posterior tibial regions, and had no history of plantar ulceration. She had a complete hysterectomy at age 37, and had received estrogen replacement therapy from age 37 to 50. Volunteer B was diagnosed with an acute CN event located at the junction of the right cuboid and the base of the right Met5. Detailed demographic characteristics are provided in Table 1.

Both women were treated with total contact casting (TCC) that was changed weekly, until the acute CN event had subsided. The involved foot was cleaned, dried, and covered in a seamless antimicrobial stocking. A layer of low-density foam padding was used to cover the toes prior to applying the plaster and fiberglass wrapping of the TCC. Upon agreeing to participate in the research study of CN, both volunteers gave written informed consent in accordance with the guidelines put forth by the Institutional Review Board and the Human Research Protection Office at Washington University in St. Louis, MO.

Table 1: Baseline demographic characteristics

	Volunteer A	Volunteer B
Age (yrs)	45	54
Height (cm)	167.6	175.3
Mass (kg)	101.8	83.7
BMI (kg/m^2)	36.2	27.2
Diabetes status	Type 1	None
Diabetes duration (yrs)	24	n/a
HbA1c	8.1	5.8
Peripheral neuropathy (yrs)	7 (secondary to DM)	4 (idiopathic)

Quantitative Computed Tomography scans

vQCT scans were taken at the Center for Clinical Imaging and Research (CCIR) at the Washington University School of Medicine using a Siemens SOMATOM Definition CT scanner (Siemens Medical Systems, Malvern, PA, USA) with acquisition parameters of 220 mA·s, 120 kVp, pitch = 1, rotation time 0.33s, and a 512x512 matrix. Positioning was standardized across scans, with the ankle in a neutral position. Raw data were reconstructed at 0.6mm slice reconstruction intervals using a B70f kernel to create vQCT images with in-plane resolution of 0.4-0.55mm (Commean *et al.*, 2011; Smith *et al.*, 2011).

Bone Segmentation Processing

The bone segmentation process has been described in detail elsewhere (Liu *et al.*, 2008; Commean *et al.*, 2011). In brief, a custom ImageJ (NIH Research Services Branch, Bethesda, MD) density-based filtering plugin was used to distinguish bone tissue from surrounding soft tissue, then Analyze (Biomedical Imaging Resource, Mayo Clinic, Rochester, MN) and a custom graph-cut software tool were used to segment bones from each other at their articulating surfaces. The end result of segmentation is a series of bone

object maps (Liu *et al.*, 2008) as shown in Figure 2, which are then used to assess bone

geometric strength indices or bone-to-bone orientation angles.
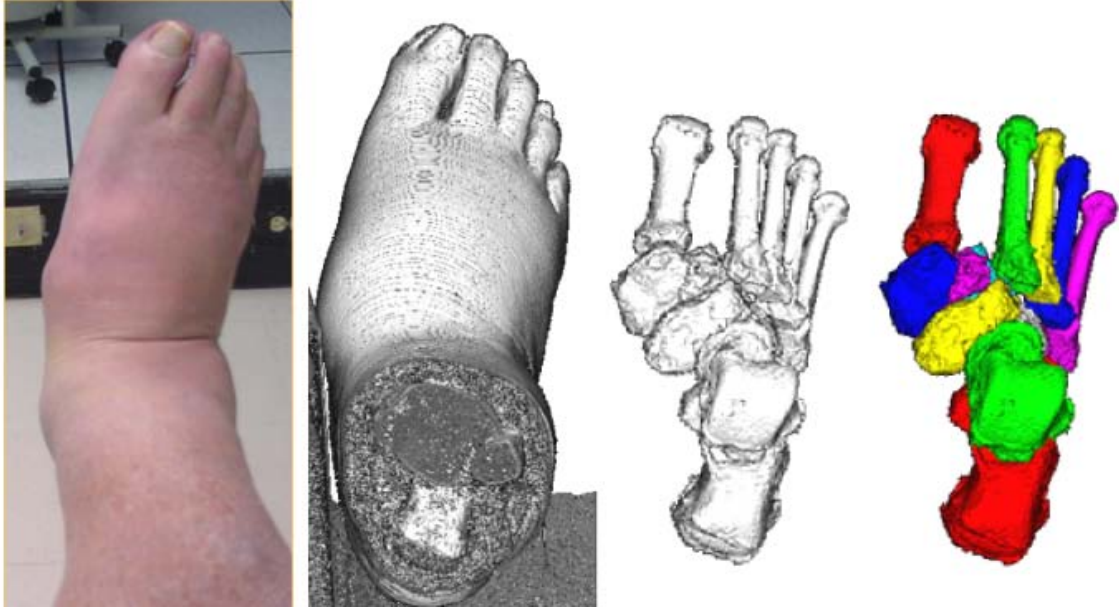
Figure 2: Bone segmentation processing. (A) photograph of an individual with acute Charcot; (B) raw QCT image; (C) filtered QCT image to remove soft tissue; (D) segmented, filled bone object maps for tarsals and metatarsals.

Bone Mineral Density and Geometric Strength Indices

For each bone, segmented bone object maps were overlaid on the raw grayscale

voxel data, and the average X-ray absorptiometry in HU was computed for each bone

volume. The average HU values for each bone were then converted to equivalent BMD

(mg/cm^3) using scan-specific HA calibration phantoms.

Full methods for bone geometric strength processing are provided in Chapter 2

and in the literature (Gutekunst *et al.*, 2012). In brief, the segmented bone object maps

were overlaid on the raw grayscale voxel data, and the resulting Met5 voxel datasets

(XYZ position and HU values) were transformed along each bone's longitudinal axis

using the BoneJ program (Doube *et al.*, 2010) in ImageJ. Realigned voxel data were interpolated to isotropic voxels (0.5mm dimension) using a cubic spline function in Analyze® software, then exported to custom Excel (Microsoft) macros for computation of regional BMD and cross-sectional I_{min}, S_{min}, average Ct.Th and BR in the central 3mm of the mid diaphysis. These bone geometric strength variables have been shown in Chapter 2 to predict *ex vivo* ultimate bending loads using identical image processing methods in cadaver samples (Gutekunst *et al.*, 2012).

Bone-to-bone orientations

Segmented bone object maps for all 12 tarsal and metatarsal bones were imported into an in-house software tool (Liu *et al.*, 2008) which allows placement of user-defined anatomic landmarks on volume-rendered surface meshes. These landmarks were chosen to produce anatomically-relevant 3D coordinate axes for each bone, with X directed laterally, Y directed axially (primarily anterior), and Z directed vertically. Bone-to-bone orientations were computed using XY'Z" Cardan rotation sequences, corresponding respectively to sagittal (α), frontal (β) and transverse (γ) angles. As the vQCT scans did not include an external frame of reference, individual bone angles were expressed with respect to calcaneus. Additionally, a number of other bone-to-bone angles were considered as relevant indices of deformity in the CN foot:

- Orientation of navicular with respect to talus (Nav:Tal)
- Orientation of first metatarsal with respect to talus (Met1:Tal)
- Orientation of Met5 with respect to cuboid (Met5:Cub)

Plantar loading assessment

Plantar pressure data were not recorded at enrollment due to the inflammation and injury risk associated with acute CN, but were recorded at 3, 6, and 12 months post-enrollment. Barefoot walking trials were collected using a two-step method (Meyers-Rice *et al.*, 1994) using an EMED-ST P2 pressure platform (Novel Inc., Munich, Germany) with a spatial resolution of 2 sensors/cm^2 and sampling frequency of 50 Hz. Each walking trial yielded a plantar pressure map that was divided into five regions using Novel Percent Mask software. The hind foot region was defined as the posterior 33% of the anterior-posterior foot length, the mid foot region was defined from 33% to 63%, and the forefoot (including the toes) comprised the remaining area. An additional dividing line was placed at 50% of the medial-lateral axis for the mid foot and forefoot regions. Plantar pressure maps and foot regions at 3, 6, and 12 months are shown in Figure 3. Pressure-derived variables were averaged over 2-3 right steps using Novel Groupmask software. We report the peak pressure (kPa) and maximum force (N) for the lateral midfoot.
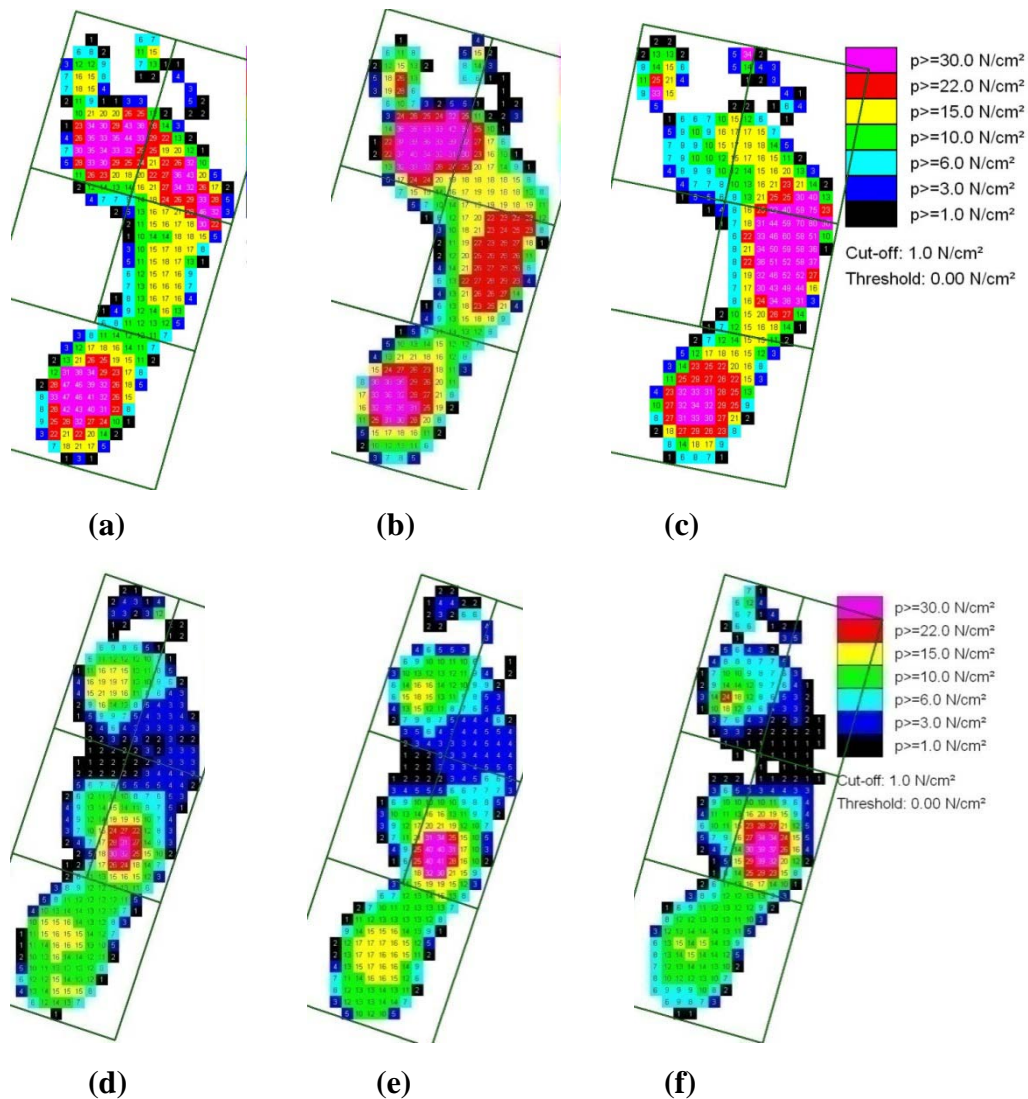
Figure 3. Peak plantar pressure maps for right foot at T2, T3, and T4: (a) – (c) represent Volunteer A, (d) – (f) represent Volunteer B.

3. Outcomes

BMD and geometric strength indices

For both women, whole-bone BMD of Met5 decreased during the off-loading TCC period from baseline to 3 months (losing 4% and 8% of baseline BMD respectively), as shown in Table 2. Both women's whole-bone BMD rebounded by 6 months, then decreased after Met5 fracture by 13% and 18%, respectively, at the 12-

month follow-up measurement. Mid-diaphyseal BMD showed a similar trend, decreasing slightly below baseline values after TCC off-loading, rebounding to slightly above baseline values by the 6 month scan, then falling to roughly a quarter below baseline after the fracture event.

Mid-diaphyseal resistance to bending loads (I_{min} and S_{min}), changed differently over time in the two volunteers. In Volunteer A, I_{min} and S_{min} increased progressively from baseline through 6 months, whereas Volunteer B exhibited minor reductions at 3 months that rebounded to slightly above baseline by 6 months. At 12 months, both volunteers showed large losses in bending strength following fracture and another prolonged period of off-loading. Mid-diaphyseal Ct.Th increased from baseline to 6 months in both volunteers by 8-9%; this thickening of cortical shell is also reflected in the 6-10% reduction of BR.

Plantar loading

While barefoot plantar pressure was not measured at baseline, the measurements at 3 months and 6 months post-enrollment showed increased peak pressure and maximum force in the lateral midfoot (representing the lateral metatarsals). See Table 3 for plantar loading results and Figure 4 for peak plantar pressure maps. Volunteer A showed greater load increases, with a rough doubling of peak plantar pressure between 3 and 6 months and an approximately 60% increase in maximum force, with further load increases at 12 months following fracture. Volunteer B began with higher peak plantar pressure and maximum force in the lateral midfoot than Volunteer A and experienced smaller increases at 6 month and 12 month follow-up.

Table 2: BMD and geometric strength indices of Met5

	T_1	T_2	T_3	T_4
Whole bone BMD (mg/cm^3)				
Volunteer A	440	423 (-4%)	444 (+1%)	368 (-23%)
Volunteer B	446	411 (-8%)	433 (-3%)	344 (-23%)
Mid-shaft BMD (mg/cm^3)				
Volunteer A	642	631 (-1.7%)	668 (+4.0%)	475 (-26%)
Volunteer B	735	695 (-5.4%)	747 (+1.6%)	567 (-23%)
Mid-shaft I_{min} (mg*mm)				
Volunteer A	212	222 (+5%)	250 (+18%)	161 (-24%)
Volunteer B	86	84 (-2%)	88 (+2%)	71 (-17%)
Mid-shaft S_{min} (mg*mm)				
Volunteer A	36.8	37.7 (+2%)	42.5 (+16%)	26.6 (+-28%)
Volunteer B	18.1	17.7 (-2%)	18.9 (+4%)	14.6 (-19%)
Mid-shaft Ct.Th (mm)				
Volunteer A	2.06	2.17 (+5%)	2.23 (+8%)	2.13 (+3%)
Volunteer B	1.97	2.09 (+6%)	2.14 (+9%)	2.01 (+2%)
Mid-shaft BR (unitless)				
Volunteer A	2.80	2.70 (-4%)	2.64 (-6%)	2.85 (+2%)
Volunteer B	2.41	2.27 (-6%)	2.17 (-10%)	2.44 (+1%)

Table 3: Plantar loading in the lateral midfoot of involved foot

	T2	T3	T4
Peak Pressure (kPa)			
Volunteer A	203	382 (+94%)	568 (+182%)
Volunteer B	355	401 (+13%)	393 (+11%)
Maximum Force (N)			
Volunteer A	358	568 (+59%)	691 (+93%)
Volunteer B	465	504 (+9%)	535 (+15%)

Bone and joint orientations

In the sagittal plane, both volunteers showed progressive increases in the relative plantar flexion of the metatarsals with respect to the calcaneus, as shown in Table 4. Moreover, increases in metatarsal plantar flexion were generally larger in the lateral metatarsals: Met1 plantar flexion increased by 3-6°, Met2 increased by 4-7°, Met3 increased by 6-11°, Met4 increased by 10-11°, and Met5 increased by 11-13°. No obvious trends occurred for the metatarsals in the frontal plane. In the transverse plane, the metatarsals showed greater adduction with respect to the calcaneus from baseline to 6 months. For the other bone-to-bone orientation angles that were assessed, only a greater adduction of Met1 with respect to the talus (13° in Volunteer A and 9° in Volunteer B) showed consistent alteration preceding the new fracture.

Table 4: 3D bone-to-bone orientation angles derived from vQCT scans.

	Sagittal angle (α) (positive = plantarflexion)				Frontal angle (β) (positive = inversion)				Transverse angle (γ) (positive = adduction)			
	T_1	T_2	T_3	T_4	T_1	T_2	T_3	T_4	T_1	T_2	T_3	T_4
Met1:Calcaneus												
Volunteer A	48	50	56	43	-15	-17	-23	-16	39	45	43	47
Volunteer B	43	42	45	41	5	15	11	15	41	47	45	49
Met2:Calcaneus												
Volunteer A	66	69	73	66	12	11	3	12	31	33	38	40
Volunteer B	56	60	59	61	27	36	32	38	38	43	48	51
Met3:Calcaneus												
Volunteer A	70	78	81	73	32	33	30	33	33	36	41	41
Volunteer B	64	69	70	73	45	51	48	51	43	53	50	59
Met4:Calcaneus												
Volunteer A	56	66	67	52	42	46	38	36	26	30	34	32
Volunteer B	58	63	68	63	56	60	59	58	39	49	49	53
Met5:Calcaneus												
Volunteer A	44	48	55	43	49	47	46	68	18	22	22	16
Volunteer B	52	63	65	64	57	62	62	62	30	43	44	48
Cuboid:Calcaneus												
Volunteer A	50	51	53	49	-10	-9	-11	-11	-1	2	-1	-5
Volunteer B	59	57	57	55	0	1	1	2	13	18	17	18
Met5:Cuboid												
Volunteer A	59	56	57	79	59	55	57	79	18	17	24	37
Volunteer B	56	60	60	60	53	58	59	58	8	9	8	12
Met1:Talus												
Volunteer A	9	10	16	3	-7	-10	-8	-12	13	17	26	18
Volunteer B	1	-1	2	-2	-2	10	5	11	24	33	26	33
Navicular:Talus												
Volunteer A	20	22	23	19	-9	-8	-7	-9	-21	-18	-6	-22
Volunteer B	26	22	22	20	-24	-20	-22	-22	1	11	6	10

4. Discussion

The prospective design of these case reports has allowed a unique opportunity to assess changes in BMD, bone geometric strength indices, foot deformities, and biomechanical loads preceding incipient mid-diaphyseal fractures of Met5. Specifically, comparing the biomechanical loading to correlates of bone strength allows a determination of the *factor of risk* for fracture (Hayes and Myers, 1995):

$$Factor\ of\ risk\ (\Phi) = \frac{applied\ load}{fracture\ load}$$

Several of the bone variables reported here (BMD, I_{min}, S_{min}, Ct.Th, BR) provide indices of fracture load, based on previous cadaver studies by our group and others (Courtney *et al.*, 1997; Muehleman *et al.*, 2000; Gutekunst *et al.*, 2012). Using identical vQCT methods as in the current case series, Gutekunst *et al* found S_{min} and Ct.Th to be the highest correlates of *ex vivo* ultimate loading of cadaver metatarsals (Gutekunst *et al.*, 2012). Similarly, the pressure-derived load variables provide indices of the applied loads responsible for the observed metatarsal fractures. Thus, this case series has permitted an assessment of whether proposed fracture mechanisms – namely, an increase in applied load or decrease in fracture load – preceded incipient Met5 fracture after CN.

Our results suggest that in these two women studied, a reduction in fracture load was not the likely causal mechanism for the observed Met5 fractures. Preceding fracture, BMD had actually rebounded to above baseline values for both women, and changes in bone geometric strength indices all indicate that fracture load did not decrease and in fact would be predicted to increase based on the findings reported in Chapter 2 (Gutekunst *et al.*, 2012). Conversely, applied load began high and rose further in the lateral midfoot in

both women: peak plantar pressure at baseline was 203 and 355 kPa for the two women, which far exceed the upper limit of the 99% confidence interval (120 kPa) for control subjects from a previous analysis (Sinacore *et al.*, 2007).

One possible explanation for the observed results is that the increased values of BMD and geometric strength indices – especially in Volunteer A – reflect a response to increased loading. Of course, causality cannot be determined from the concomitant increases in plantar loading and indices of bone strength; nor can the likely role of weak bones (Herbst *et al.*, 2004) in neuropathic fracture be refuted by these data. Rather, we report only that the increases observed in BMD and geometric strength indices do not support the hypothesis that CN-related reductions in bone quality are a necessary precursor to metatarsal fracture. Furthermore, the findings reported here suggest that altered bone-to-bone orientation angles may help explain the link between acute CN and increased biomechanical loading. Increased plantar flexion and adduction of the metatarsals (particularly the lateral metatarsals) are consistent with the progression of a varus hindfoot with metatarsus adductus deformity. Hindfoot varus (Raikin *et al.*, 2008) and metatarsus adductus (Theodorou *et al.*, 1999; van der Vlies *et al.*, 2007) have been previously implicated in lateral metatarsal fractures.

One variable that may increase fracture risk is the patient's activity level. We cannot rule out the role of load-bearing volume in the observed fractures, though neither volunteer reported an increase in walking or other load-bearing activity preceding incipient fracture. Future studies may utilize activity monitoring to help assess the role of activity on neuropathic fracture. Additionally, we recognize that our measures of barefoot plantar loading present an incomplete description of biomechanical loads that may

106

influence fracture. It would be most physiologically relevant to use plantar pressure data in conjunction with motion capture data and vQCT-derived estimates of bone strength to compute bending stresses applied to the metatarsals throughout a range of weight bearing activites. Nonetheless, we consider peak pressure and maximum force to be adequate qualitative measures of biomechanical loading.

In conclusion, we assessed two individuals with CN before and after mid-diaphyseal fracture of Met5 using plantar pressure measurement and novel vQCT techniques to quantify bone strength and 3D bone-to-bone orientation angles. We find that BMD and geometric strength indices increased mildly to moderately preceding fracture, which does not completely explain the possible link between weakening bone material properties and incident fractures. Plantar loads were high at enrollment and increased before incipient metatarsal fracture, which lends support to the possible causal role of biomechanical loading on metatarsal fractures. Finally, our results suggest that the progression of metatarsus adductus and equinovarus foot deformities that have been previously associated with lateral metatarsal fractures may lead to increased metatarsal loading.

REFERENCES

(2012) Diagnosis and classification of diabetes mellitus. *Diabetes Care* **35 Suppl 1,** S64-S71.

Armstrong,D.G. and Lavery,L.A. (1998) Elevated peak plantar pressures in patients who have Charcot arthropathy. *J.Bone Joint Surg.Am.* **80,** 365-369.

Armstrong,D.G., Lavery,L.A., and Bushman,T.R. (1998a) Peak foot pressures influence the healing time of diabetic foot ulcers treated with total contact casts. *J.Rehabil.Res.Dev.* **35,** 1-5.

Armstrong,D.G., Peters,E.J., Athanasiou,K.A., and Lavery,L.A. (1998b) Is there a critical level of plantar foot pressure to identify patients at risk for neuropathic foot ulceration? *J.Foot Ankle Surg.* **37,** 303-307.

Armstrong,D.G., Todd,W.F., Lavery,L.A., Harkless,L.B., and Bushman,T.R. (1997) The natural history of acute Charcot's arthropathy in a diabetic foot specialty clinic. *J.Am.Podiatr.Med.Assoc.* **87,** 272-278.

Arndt,A., Ekenman,I., Westblad,P., and Lundberg,A. (2002) Effects of fatigue and load variation on metatarsal deformation measured in vivo during barefoot walking. *J Biomech.* **35,** 621-628.

Beck,T.J. (2007) Extending DXA beyond bone mineral density: understanding hip structure analysis. *Curr.Osteoporos.Rep.* **5,** 49-55.

Beck,T.J., Ruff,C.B., Mourtada,F.A., Shaffer,R.A., Maxwell-Williams,K., Kao,G.L., Sartoris,D.J., and Brodine,S. (1996) Dual-energy X-ray absorptiometry derived structural geometry for stress fracture prediction in male U.S. Marine Corps recruits. *J Bone Miner.Res.* **11,** 645-653.

Beck,T.J., Ruff,C.B., Shaffer,R.A., Betsinger,K., Trone,D.W., and Brodine,S.K. (2000) Stress fracture in military recruits: gender differences in muscle and bone susceptibility factors. *Bone* **27,** 437-444.

Beimers,L., Tuijthof,G.J., Blankevoort,L., Jonges,R., Maas,M., and van Dijk,C.N. (2008) In-vivo range of motion of the subtalar joint using computed tomography. *J Biomech.* **41,** 1390-1397.

Bem,R., Jirkovska,A., Dubsky,M., Fejfarova,V., Buncova,M., Skibova,J., and Jude,E.B. (2010) Role of quantitative bone scanning in the assessment of bone turnover in patients with Charcot foot. *Diabetes Care* **33,** 348-349.

Bonds,D.E., Larson,J.C., Schwartz,A.V., Strotmeyer,E.S., Robbins,J., Rodriguez,B.L., Johnson,K.C., and Margolis,K.L. (2006) Risk of fracture in women with type 2 diabetes: the Women's Health Initiative Observational Study. *J Clin.Endocrinol.Metab* **91,** 3404-3410.

Borggrefe,J., Graeff,C., Nickelsen,T.N., Marin,F., and Gluer,C.C. (2010) Quantitative computed tomographic assessment of the effects of 24 months of teriparatide treatment on 3D femoral neck bone distribution, geometry, and bone strength: results from the EUROFORS study. *J Bone Miner.Res.* **25,** 472-481.

Boulton,A.J., Hardisty,C.A., Betts,R.P., Franks,C.I., Worth,R.C., Ward,J.D., and Duckworth,T. (1983) Dynamic foot pressure and other studies as diagnostic and management aids in diabetic neuropathy. *Diabetes Care* **6,** 26-33.

Bouxsein,M.L., Boyd,S.K., Christiansen,B.A., Guldberg,R.E., Jepsen,K.J., and Muller,R. (2010) Guidelines for assessment of bone microstructure in rodents using micro-computed tomography. *J Bone Miner.Res.* **25,** 1468-1486.

Brown,K.M., Bursey,D.E., Arneson,L.J., Andrews,C.A., Ludewig,P.M., and Glasoe,W.M. (2009) Consideration of digitization precision when building local coordinate axes for a foot model. *J Biomech.* **42,** 1263-1269.

Brudvig,T.J., Gudger,T.D., and Obermeyer,L. (1983) Stress fractures in 295 trainees: a one-year study of incidence as related to age, sex, and race. *Mil.Med.* **148,** 666-667.

Burghardt,A.J., Issever,A.S., Schwartz,A.V., Davis,K.A., Masharani,U., Majumdar,S., and Link,T.M. (2010) High-resolution peripheral quantitative computed tomographic imaging of cortical and trabecular bone microarchitecture in patients with type 2 diabetes mellitus. *J Clin.Endocrinol.Metab* **95,** 5045-5055.

Camacho,D.L., Ledoux,W.R., Rohr,E.S., Sangeorzan,B.J., and Ching,R.P. (2002) A three-dimensional, anatomically detailed foot model: a foundation for a finite element simulation and means of quantifying foot-bone position. *J Rehabil.Res.Dev.* **39,** 401-410.

Cavanagh,P.R., Young,M.J., Adams,J.E., Vickers,K.L., and Boulton,A.J. (1994) Radiographic abnormalities in the feet of patients with diabetic neuropathy. *Diabetes Care* **17,** 201-209.

Centers for Disease Control . National Diabetes Fact Sheet, 2011. http://www.cdc.gov/diabetes/pubs/pdf/ndfs_2011.pdf . 2011. 7-15-2012.
Ref Type: Electronic Citation

Chantelau,E. (2005) The perils of procrastination: effects of early vs. delayed detection and treatment of incipient Charcot fracture. *Diabet.Med.* **22,** 1707-1712.

Chantelau,E., Richter,A., Ghassem-Zadeh,N., and Poll,L.W. (2007) "Silent" bone stress injuries in the feet of diabetic patients with polyneuropathy: a report on 12 cases. *Arch.Orthop.Trauma Surg.* **127,** 171-177.

Cofield,R.H., Morrison,M.J., and Beabout,J.W. (1983) Diabetic neuroarthropathy in the foot: patient characteristics and patterns of radiographic change. *Foot Ankle* **4,** 15-22.

Commean,P.K., Ju,T., Liu,L., Sinacore,D.R., Hastings,M.K., and Mueller,M.J. (2009) Tarsal and metatarsal bone mineral density measurement using volumetric quantitative computed tomography. *J Digit.Imaging* **22,** 492-502.

Commean,P.K., Kennedy,J.A., Bahow,K.A., Hildebolt,C.F., Liu,L., Smith,K.E., Hastings,M.K., Ju,T., Prior,F.W., and Sinacore,D.R. (2011) Volumetric Quantitative Computed Tomography Measurement Precision for Volumes and Densities of Tarsal and Metatarsal Bones. *J Clin.Densitom.* **14,** 313-320.

Courtney,A.C., Davis,B.L., Manning,T., and Kambic,H.E. (1997) Effects of age, density, and geometry on the bending strength of human metatarsals. *Foot Ankle Int.* **18,** 216-221.

Crews,R.T. and Wrobel,J.S. (2008) Physical management of the Charcot foot. *Clin.Podiatr.Med.Surg.* **25,** 71-9, vii.

Crossley,K., Bennell,K.L., Wrigley,T., and Oakes,B.W. (1999) Ground reaction forces, bone characteristics, and tibial stress fracture in male runners. *Med.Sci Sports Exerc.* **31,** 1088-1093.

Cundy,T.F., Edmonds,M.E., and Watkins,P.J. (1985) Osteopenia and metatarsal fractures in diabetic neuropathy. *Diabet.Med.* **2,** 461-464.

Diederichs,G., Link,T.M., Kentenich,M., Schwieger,K., Huber,M.B., Burghardt,A.J., Majumdar,S., Rogalla,P., and Issever,A.S. (2009) Assessment of trabecular bone structure of the calcaneus using multi-detector CT: correlation with microCT and biomechanical testing. *Bone* **44,** 976-983.

Donahue,S.W. and Sharkey,N.A. (1999) Strains in the metatarsals during the stance phase of gait: implications for stress fractures. *J Bone Joint Surg.Am.* **81,** 1236-1244.

Doube,M., Klosowski,M.M., Arganda-Carreras,I., Cordelieres,F.P., Dougherty,R.P., Jackson,J.S., Schmid,B., Hutchinson,J.R., and Shefelbine,S.J. (2010) BoneJ: Free and extensible bone image analysis in ImageJ. *Bone* **47,** 1076-1079.

Evans,R.K., Negus,C., Antczak,A.J., Yanovich,R., Israeli,E., and Moran,D.S. (2008) Sex differences in parameters of bone strength in new recruits: beyond bone density. *Med.Sci Sports Exerc.* **40,** S645-S653.

Fleischli,J.G., Laughlin,T.J., Lavery,L.A., Shah,B., Lanctot,D., Agrawal,C.M., and Athanasiou,K. (1998) The effects of diabetes mellitus on the material properties of human metatarsal bones. *J Foot Ankle Surg.* **37,** 195-198.

Frykberg,R.G. and Belczyk,R. (2008) Epidemiology of the Charcot foot. *Clin.Podiatr.Med.Surg.* **25,** 17-28.

Giladi,M., Milgrom,C., Simkin,A., Stein,M., Kashtan,H., Margulies,J., Rand,N., Chisin,R., Steinberg,R., Aharonson,Z., and . (1987) Stress fractures and tibial bone width. A risk factor. *J Bone Joint Surg.Br.* **69,** 326-329.

Gill,G., Benbow,S., Tesfaye,S., Kaczmarczyk,E., and Kaye,L. (1997) Painless stress fractures in diabetic neuropathic feet. *Postgrad.Med.J* **73,** 241-242.

Gough,A., Abraha,H., Li,F., Purewal,T.S., Foster,A.V., Watkins,P.J., Moniz,C., and Edmonds,M.E. (1997) Measurement of markers of osteoclast and osteoblast activity in patients with acute and chronic diabetic Charcot neuroarthropathy. *Diabet.Med.* **14,** 527-531.

Gutekunst,D.J., Patel,T.K., Commean,P.K., Smith,K.E., Silva,M., and Sinacore DR (2012) Predicting ex vivo failure loads in human metatarsals using bone strength indices derived from volumetric quantitative computed tomography. *In review submitted to Journal of Biomechanics*.

Hangartner,T.N. (2007) Thresholding technique for accurate analysis of density and geometry in QCT, pQCT and microCT images. *J Musculoskelet.Neuronal.Interact.* **7,** 9-16.

Hastings,M.K., Gelber,J., Commean,P.K., Prior,F., and Sinacore,D.R. (2008) Bone Mineral Density of the Tarsals and Metatarsals With Reloading. *Phys Ther* **88,** 766-779.

Hastings,M.K., Johnson,J.E., Strube,M.J., Hildebolt,C.F., Bohnert,K.L., Prior F.W., and Sinacore D.R. (2012) Progressive foot deformity is evident in neuropathic (Charcot) arthropathy at one and two years. *(in review) submitted to Journal of Bone and Joint Surgery (Am)*.

Hastings,M.K., Sinacore,D.R., Mercer-Bolton,N., McCormick,J.J., Hildebolt,C.F., Prior,F.W., and Johnson,J.E. (2011) Precision of foot alignment measures in Charcot arthropathy. *Foot Ankle Int.* **32,** 867-872.

Hayes,W.C. and Myers,E.R. (1995) Biomechanics of fractures. In *Osteoporosis: etiology, diagnosis, management.* (Edited by Riggs,B.L. and Melton III,L.) Pp. 93-114. Lippincott-Raven Publishers, Philadelphia.

Herbst,S.A., Jones,K.B., and Saltzman,C.L. (2004) Pattern of diabetic neuropathic arthropathy associated with the peripheral bone mineral density. *J.Bone Joint Surg.Br.* **86,** 378-383.

Hulkko,A. and Orava,S. (1987) Stress fractures in athletes. *Int.J Sports Med.* **8,** 221-226.

Jeffcoate,W.J., Game,F., and Cavanagh,P.R. (2005) The role of proinflammatory cytokines in the cause of neuropathic osteoarthropathy (acute Charcot foot) in diabetes. *Lancet* **366,** 2058-2061.

Kaptoge,S., Beck,T.J., Reeve,J., Stone,K.L., Hillier,T.A., Cauley,J.A., and Cummings,S.R. (2008) Prediction of incident hip fracture risk by femur geometry variables measured by hip structural analysis in the study of osteoporotic fractures. *J Bone Miner.Res.* **23,** 1892-1904.

Kontulainen,S.A., Johnston,J.D., Liu,D., Leung,C., Oxland,T.R., and McKay,H.A. (2008) Strength indices from pQCT imaging predict up to 85% of variance in bone failure properties at tibial epiphysis and diaphysis. *J Musculoskelet.Neuronal.Interact.* **8,** 401-409.

LaCroix,A.Z., Beck,T.J., Cauley,J.A., Lewis,C.E., Bassford,T., Jackson,R., Wu,G., and Chen,Z. (2010) Hip structural geometry and incidence of hip fracture in postmenopausal women: what does it add to conventional bone mineral density? *Osteoporos.Int.* **21,** 919-929.

Largey,A., Bonnel,F., Canovas,F., Subsol,G., Chemouny,S., and Banegas,F. (2007) Three-dimensional analysis of the intrinsic anatomy of the metatarsal bones. *J Foot Ankle Surg.* **46,** 434-441.

Lavery,L.A., Armstrong,D.G., Wunderlich,R.P., Tredwell,J., and Boulton,A.J. (2003) Predictive value of foot pressure assessment as part of a population-based diabetes disease management program. *Diabetes Care* **26,** 1069-1073.

Ledoux,W.R., Rohr,E.S., Ching,R.P., and Sangeorzan,B.J. (2006) Effect of foot shape on the three-dimensional position of foot bones. *J Orthop.Res.* **24,** 2176-2186.

Lee,L., Blume,P.A., and Sumpio,B. (2003) Charcot joint disease in diabetes mellitus. *Ann.Vasc.Surg.* **17,** 571-580.

Lidtke,R.H., Patel,D., and Muehleman,C. (2000) Calcaneal bone mineral density and mechanical strength of the metatarsals. *J Am.Podiatr.Med.Assoc.* **90,** 435-440.

Liu,D., Manske,S.L., Kontulainen,S.A., Tang,C., Guy,P., Oxland,T.R., and McKay,H.A. (2007) Tibial geometry is associated with failure load ex vivo: a MRI, pQCT and DXA study. *Osteoporos.Int.* **18,** 991-997.

Liu,L., Commean,P.K., Hildebolt,C.F., Sinacore D.R., Prior F.W., Carson,J.P., Kakadiaris,I., and Ju T . Automated foot-bone registration using subdivision-embedded atlases for spatial mapping of bone mineral density. J Digit.Imaging . 2012.
Ref Type: In Press

Liu,L., Raber,D., Nopachai,D., Commean,P., Sinacore,D., Prior,F., Pless,R., and Ju,T. (2008) Interactive separation of segmented bones in CT volumes using graph cut. *Med.Image Comput.Comput.Assist.Interv.* **11,** 296-304.

Manske,S.L., Liu-Ambrose,T., de Bakker,P.M., Liu,D., Kontulainen,S., Guy,P., Oxland,T.R., and McKay,H.A. (2006) Femoral neck cortical geometry measured with magnetic resonance imaging is associated with proximal femur strength. *Osteoporos.Int.* **17,** 1539-1545.

McBryde,A.M., Jr. (1985) Stress fractures in runners. *Clin.Sports Med.* **4,** 737-752.

Melton,L.J., III, Beck,T.J., Amin,S., Khosla,S., Achenbach,S.J., Oberg,A.L., and Riggs,B.L. (2005) Contributions of bone density and structure to fracture risk assessment in men and women. *Osteoporos.Int.* **16,** 460-467.

Melton,L.J., III, Leibson,C.L., Achenbach,S.J., Therneau,T.M., and Khosla,S. (2008) Fracture risk in type 2 diabetes: update of a population-based study. *J Bone Miner.Res.* **23,** 1334-1342.

Meyers-Rice,B., Sugars,L., McPoil,T., and Cornwall,M.W. (1994) Comparison of three methods for obtaining plantar pressures in nonpathologic subjects. *J Am.Podiatr.Med Assoc.* **84,** 499-504.

Milgrom,C., Giladi,M., Simkin,A., Rand,N., Kedem,R., Kashtan,H., Stein,M., and Gomori,M. (1989) The area moment of inertia of the tibia: a risk factor for stress fractures. *J Biomech.* **22,** 1243-1248.

Muehleman,C., Lidtke,R., Berzins,A., Becker,J.H., Shott,S., and Sumner,D.R. (2000) Contributions of bone density and geometry to the strength of the human second metatarsal. *Bone* **27,** 709-714.

Mueller,M.J., Hastings,M., Commean,P.K., Smith,K.E., Pilgram,T.K., Robertson,D., and Johnson,J. (2003) Forefoot structural predictors of plantar pressures during walking in people with diabetes and peripheral neuropathy. *J Biomech.* **36,** 1009-1017.

Otsu,N. (1979) A threshold selection method from gray-level histograms. *IEEE Trans Syst Man Cybern* **8,** 62-66.

Parr,W.C., Chatterjee,H.J., and Soligo,C. (2012) Calculating the axes of rotation for the subtalar and talocrural joints using 3D bone reconstructions. *J Biomech.* **45,** 1103-1107.

Pester,S. and Smith,P.C. (1992) Stress fractures in the lower extremities of soldiers in basic training. *Orthop.Rev.* **21,** 297-303.

Petrova,N.L., Foster,A.V., and Edmonds,M.E. (2005) Calcaneal bone mineral density in patients with Charcot neuropathic osteoarthropathy: differences between Type 1 and Type 2 diabetes. *Diabet Med* **22,** 756-761.

Raikin,S.M., Slenker,N., and Ratigan,B. (2008) The association of a varus hindfoot and fracture of the fifth metatarsal metaphyseal-diaphyseal junction: the Jones fracture. *Am.J Sports Med.* **36,** 1367-1372.

Robertson,D.D., Mueller,M.J., Smith,K.E., Commean,P.K., Pilgram,T., and Johnson,J.E. (2002) Structural changes in the forefoot of individuals with diabetes and a prior plantar ulcer. *J Bone Joint Surg.Am.* **84-A,** 1395-1404.

Robling,A.G., Hinant,F.M., Burr,D.B., and Turner,C.H. (2002) Improved bone structure and strength after long-term mechanical loading is greatest if loading is separated into short bouts. *J Bone Miner.Res.* **17,** 1545-1554.

Rogers,L.C., Frykberg,R.G., Armstrong,D.G., Boulton,A.J., Edmonds,M., Van,G.H., Hartemann,A., Game,F., Jeffcoate,W., Jirkovska,A., Jude,E., Morbach,S., Morrison,W.B., Pinzur,M., Pitocco,D., Sanders,L., Wukich,D.K., and Uccioli,L. (2011) The Charcot foot in diabetes. *Diabetes Care* **34,** 2123-2129.

Sanders,L.J. and Fryberg,R.G. (2005) Charcot Neuroarthropathy of the Foot. In *Evaluation Techniques and Nonsurgical Management* Pp. 439-466.

Schon,L.C., Weinfeld,S.B., Horton,G.A., and Resch,S. (1998) Radiographic and clinical classification of acquired midtarsus deformities. *Foot Ankle Int.* **19,** 394-404.

Schwartz,A.V., Sellmeyer,D.E., Ensrud,K.E., Cauley,J.A., Tabor,H.K., Schreiner,P.J., Jamal,S.A., Black,D.M., and Cummings,S.R. (2001) Older women with diabetes have an increased risk of fracture: a prospective study. *J.Clin.Endocrinol.Metab* **86,** 32-38.

Schwend,R.M. and Drennan,J.C. (2003) Cavus foot deformity in children. *J Am.Acad.Orthop.Surg.* **11,** 201-211.

Sigurdsson,G., Aspelund,T., Chang,M., Jonsdottir,B., Sigurdsson,S., Eiriksdottir,G., Gudmundsson,A., Harris,T.B., Gudnason,V., and Lang,T.F. (2006) Increasing sex difference in bone strength in old age: The Age, Gene/Environment Susceptibility-Reykjavik study (AGES-REYKJAVIK). *Bone* **39,** 644-651.

Silva,M.J., Brodt,M.D., Lynch,M.A., McKenzie,J.A., Tanouye,K.M., Nyman,J.S., and Wang,X. (2009) Type 1 diabetes in young rats leads to progressive trabecular bone loss, cessation of cortical bone growth, and diminished whole bone strength and fatigue life. *J Bone Miner.Res.* **24,** 1618-1627.

Simon,J., Doederlein,L., McIntosh,A.S., Metaxiotis,D., Bock,H.G., and Wolf,S.I. (2006) The Heidelberg foot measurement method: development, description and assessment. *Gait Posture* **23,** 411-424.

Sinacore,D.R., Bohnert,K.L., Hastings,M.K., and Johnson,J.E. (2007) Mid foot kinetics characterize structural polymorphism in diabetic foot disease. *Clinical Biomechanics* **23,** 653-661.

Sinacore,D.R., Hastings,M.K., Bohnert,K.L., Fielder,F.A., Villareal,D.T., Blair,V.P., III, and Johnson,J.E. (2008) Inflammatory osteolysis in diabetic neuropathic (charcot) arthropathies of the foot. *Phys Ther* **88,** 1399-1407.

Sinha,S., Munichoodappa,C.S., and Kozak,G.P. (1972) Neuro-arthropathy (Charcot joints) in diabetes mellitus (clinical study of 101 cases). *Medicine (Baltimore)* **51,** 191-210.

Smith,K.E., Commean,P.K., Mueller,M.J., Robertson,D.D., Pilgram,T., and Johnson,J. (2000) Assessment of the diabetic foot using spiral computed tomography imaging and plantar pressure measurements: a technical report. *J.Rehabil.Res.Dev.* **37,** 31-40.

Smith,K.E., Commean,P.K., Robertson,D.D., Pilgram,T., and Mueller,M.J. (2001) Precision and accuracy of computed tomography foot measurements. *Arch.Phys.Med.Rehabil.* **82,** 925-929.

Smith,K.E., Whiting,B.R., Reiker,G.G., Commean,P.K., Sinacore,D.R., and Prior,F.W. (2011) Assessment of technical and biological parameters of volumetric quantitative computed tomography of the foot: a phantom study. *Osteoporos.Int.* **23,** 1977-1985.

Stebbins,J., Harrington,M., Thompson,N., Zavatsky,A., and Theologis,T. (2006) Repeatability of a model for measuring multi-segment foot kinematics in children. *Gait Posture* **23,** 401-410.

Stebbins,J., Harrington,M., Thompson,N., Zavatsky,A., and Theologis,T. (2010) Gait compensations caused by foot deformity in cerebral palsy. *Gait Posture* **32,** 226-230.

Steel,M.W., III, Johnson,K.A., DeWitz,M.A., and Ilstrup,D.M. (1980) Radiographic measurements of the normal adult foot. *Foot Ankle* **1,** 151-158.

Stindel,E., Udupa,J.K., Hirsch,B.E., and Odhner,D. (1999a) A characterization of the geometric architecture of the peritalar joint complex via MRI: an aid to the classification of foot type. *IEEE Trans Med.Imaging* **18,** 753-763.

Stindel,E., Udupa,J.K., Hirsch,B.E., Odhner,D., and Couture,C. (1999b) 3D MR image analysis of the morphology of the rear foot: application to classification of bones. *Comput.Med.Imaging Graph.* **23,** 75-83.

Stokes,I.A., Faris,I.B., and Hutton,W.C. (1975) The neuropathic ulcer and loads on the foot in diabetic patients. *Acta Orthop.Scand.* **46,** 839-847.

Stokes,I.A., Hutton,W.C., and Stott,J.R. (1979) Forces acting on the metatarsals during normal walking. *J Anat.* **129,** 579-590.

Szulc,P., Duboeuf,F., Schott,A.M., Dargent-Molina,P., Meunier,P.J., and Delmas,P.D. (2006) Structural determinants of hip fracture in elderly women: re-analysis of the data from the EPIDOS study. *Osteoporos.Int.* **17,** 231-236.

Theodorou,D.J., Theodorou,S.J., Boutin,R.D., Chung,C., Fliszar,E., Kakitsubata,Y., and Resnick,D. (1999) Stress fractures of the lateral metatarsal bones in metatarsus adductus foot deformity: a previously unrecognized association. *Skeletal Radiol* **28,** 679-684.

Thompson,R.C., Jr. and Clohisy,D.R. (1993) Deformity following fracture in diabetic neuropathic osteoarthropathy. Operative management of adults who have type-I diabetes. *J.Bone Joint Surg.Am.* **75,** 1765-1773.

Turner,C.H. and Burr,D.B. (1993) Basic biomechanical measurements of bone: a tutorial. *Bone* **14,** 595-608.

Turner,C.H. and Robling,A.G. (2003) Designing exercise regimens to increase bone strength. *Exerc.Sport Sci Rev.* **31,** 45-50.

Uccioli,L., Sinistro,A., Almerighi,C., Ciaprini,C., Cavazza,A., Giurato,L., Ruotolo,V., Spasaro,F., Vainieri,E., Rocchi,G., and Bergamini,A. (2010) Proinflammatory modulation of the surface and cytokine phenotype of monocytes in patients with acute Charcot foot. *Diabetes Care* **33,** 350-355.

van der Vlies,C.H., Ponsen,K.J., Besselaar,P.P., and Goslings,J.C. (2007) Significant forefoot varus deformity resulting in progressive stress fractures of all lesser metatarsal bones. *J Foot Ankle Surg.* **46,** 394-397.

Veves,A., Murray,H.J., Young,M.J., and Boulton,A.J. (1992) The risk of foot ulceration in diabetic patients with high foot pressure: a prospective study. *Diabetologia* **35,** 660-663.

Ward,K.A., Pye,S.R., Adams,J.E., Boonen,S., Vanderschueren,D., Borghs,H., Gaytant,J., Gielen,E., Bartfai,G., Casanueva,F.F., Finn,J.D., Forti,G., Giwercman,A., Han,T.S., Huhtaniemi,I.T., Kula,K., Labrie,F., Lean,M.E., Pendleton,N., Punab,M., Silman,A.J., Wu,F.C., and O'Neill,T.W. (2011) Influence of age and sex steroids on bone density and geometry in middle-aged and elderly European men. *Osteoporos.Int.* **22,** 1513-1523.

Warden,S.J., Hurst,J.A., Sanders,M.S., Turner,C.H., Burr,D.B., and Li,J. (2005) Bone adaptation to a mechanical loading program significantly increases skeletal fatigue resistance. *J Bone Miner.Res.* **20,** 809-816.

Weinfeld,S.B., Haddad,S.L., and Myerson,M.S. (1997) Metatarsal stress fractures. *Clin.Sports Med.* **16,** 319-338.

Whittaker,E.C., Aubin,P.M., and Ledoux,W.R. (2011) Foot bone kinematics as measured in a cadaveric robotic gait simulator. *Gait Posture* **33,** 645-650.

Wolf,S.K. (1998) Diabetes mellitus and predisposition to athletic pedal fracture. *J Foot Ankle Surg.* **37,** 16-22.

Woodburn,J., Udupa,J.K., Hirsch,B.E., Wakefield,R.J., Helliwell,P.S., Reay,N., O'Connor,P., Budgen,A., and Emery,P. (2002) The geometric architecture of the subtalar and midtarsal joints in rheumatoid arthritis based on magnetic resonance imaging. *Arthritis Rheum.* **46,** 3168-3177.

World Health Organization . World Health Organization Diabetes Fact Sheet. http://www.who.int/mediacentre/factsheets/fs312/en/index.html . 2011. 7-15-2012.
Ref Type: Electronic Citation

Wukich,D.K. and Sung,W. (2009) Charcot arthropathy of the foot and ankle: modern concepts and management review. *J Diabetes Complications* **23,** 409-426.

Wukich,D.K., Sung,W., Wipf,S.A., and Armstrong,D.G. (2011) The consequences of complacency: managing the effects of unrecognized Charcot feet. *Diabet.Med.* **28,** 195-198.

Young,M.J., Marshall,A., Adams,J.E., Selby,P.L., and Boulton,A.J. (1995) Osteopenia, neurological dysfunction, and the development of Charcot neuroarthropathy. *Diabetes Care* **18,** 34-38.

Yu,G.V. and Hudson,J.R. (2002) Evaluation and treatment of stage 0 Charcot's neuroarthropathy of the foot and ankle. *J Am.Podiatr.Med Assoc.* **92,** 210-220.

Zebaze,R.M., Ghasem-Zadeh,A., Bohte,A., Iuliano-Burns,S., Mirams,M., Price,R.I., Mackie,E.J., and Seeman,E. (2010) Intracortical remodelling and porosity in the distal radius and post-mortem femurs of women: a cross-sectional study. *Lancet* **375,** 1729-1736.

Curriculum Vitae

David Joseph Gutekunst

Ph.D. Candidate, Washington University in Saint Louis, USA

Contact Information:
Washington University School of Medicine
Campus Box 8502
4444 Forest Park Boulevard
Saint Louis, MO 63108

Telephone: (314) 482-6819
Fax: (314) 747-0674
Email: djgutekunst@wustl.edu

Education

Washington University School of Medicine, *Saint Louis, Missouri, USA*
Movement Science Program (Biomechanics concentration)
Doctor of Philosophy (Ph.D.) degree completed in September 2012.

Wake Forest University, *Winston-Salem, North Carolina, USA*
Department of Health and Exercise Science (Biomechanics concentration)
Master of Science (M.S.) degree awarded in May 2004.

Washington University, *Saint Louis, Missouri, USA*
Department of Biomedical Engineering, School of Engineering & Applied Sciences
Bachelor of Science (B.S.) degree awarded in May 2002 (minor in Biomedical Physics).

Employment and Academic Research Experience

Applied Kinesiology Laboratory, Washington University   *September 2007 – September 2012*
- Compared plantar pressure off-loading capabilities of treatments to heal plantar ulcers.
- Developed and assessed measurement precision for an anatomic landmark-based method to assess 3D pedal bone orientations using quantitative computed tomography (QCT) scans of the foot.
- Conducted ex-vivo materials testing to validate a novel QCT method to measure geometric indices of pedal bone strength including bone mineral density, cross-sectional area, section modulus, and buckling ratio.
- Assessed the effects of diabetes mellitus, peripheral neuropathy, and neuropathic Charcot arthropathy on 3D foot deformities, bone quantity, and geometric indices of bone quality.

US Army Research Institute of Environmental Medicine   *September 2004 – September 2007*
- Worked on multiple studies to identify overuse injury mechanisms, evaluate novel training programs, and assess physiological effects of protective and assistive military technologies.
- Contributed to study design; subject recruitment; data collection and analysis; and presentation of findings.
- Conducted tests including three-dimensional motion capture, oxygen consumption, gait biomechanics and efficiency, body composition, and physical performance testing.

J.B. Snow Biomechanics Laboratory, Wake Forest University   *August 2002 – June 2004*
- Conducted tests of gait, balance, and strength for a clinical trial studying the effects of an exercise regimen and glucosamine/chondroitin in older adults with knee osteoarthritis.
- Collected, edited, and analyzed data using a six-camera three-dimensional high-speed videography system, six-channel force platform, and isokinetic strength testing equipment.

Publications

1. **Gutekunst DJ;** Hastings MK; Bohnert KL; Strube MJ; and DR Sinacore (2011). Removable cast walker boots yield greater forefoot off-loading than total contact casts. *Clinical Biomechanics* 26(6): 649-654.
2. Gregorczyk KN; Hasselquist L; Schiffman JM; Bensel CK; Obusek JP; and **DJ Gutekunst** (2010). Effects of a lower-body exoskeleton device on metabolic cost and gait biomechanics during load carriage. *Ergonomics*, 53(10):1263-1275.
3. Harman EA; **Gutekunst DJ;** Frykman PN; Sharp MA; Nindl BC; Alemany JA; and RP Mello (2008). Prediction of simulated battlefield physical performance from field-expedient tests. *Military Medicine*, 173(1):36-41.
4. Harman EA; **Gutekunst DJ;** Frykman PN; Nindl BC; Alemany JA; and RP Mello (2008). Effects of a weight lifting based training program on military physical performance. *Journal of Strength and Conditioning Research*, 22(2):524-534.
5. **Gutekunst DJ** (2006). Accounting for resting energy expenditure is necessary when bout durations differ. *Med Sci Sports Exercise*, 38(6):797.
6. Messier SP; **Gutekunst DJ;** Davis C; and P DeVita. (2005). Weight loss reduces knee joint loads in overweight and obese older adults with knee osteoarthritis. Arthritis Rheumatism, 52(7), 2026-2032.

Manuscripts in Preparation and Review

1. **Gutekunst DJ;** Patel TK; Smith KE; Commean PK; Silva MJ; and DR Sinacore (2012). Predicting ex vivo failure loads in human metatarsals using bone strength indices derived from volumetric quantitative computed tomography. In final review, *Journal of Biomechanics.*
2. **Gutekunst DJ** and DR Sinacore (2012). Time course of changes in pedal bone quantity, quality, orientation, and plantar loads preceding metatarsal fracture in individuals with neuropathic Charcot arthropathy. In review, *Journal of Orthopaedic and Sports Physical Therapy*.
3. **Gutekunt DJ;** Smith KE; Commean PK; Bohnert KL; Prior FW; and DR Sinacore (2012). Impact of Charcot neuroarthropathy on metatarsal bone mineral density and geometric strength indices. In review, *Bone.*
4. Sinacore DR; **Gutekunst DJ;** Hastings MK; Strube MJ; Bohnert KL; Prior FW; and JE Johnson (2012). Adult-acquired neuropathic foot deformity: Impact on ankle and subtalar joint motion. In review, *J Foot Ankle Research.*
5. SeayJF; Frykman PN; Sauer SG; and **DJ Gutekunst** (2012). **Lower Extremity Mechanics During Marching at Three Different Cadences for 60 Minutes.** In review, *Journal of Applied Biomechanics.*
6. **Gutekunst DJ;** Lu L; Ju T; Prior FW; and DR Sinacore (2012). Atlas-based, anatomically relevant three-dimensional foot bone-to-bone orientation angles derived from quantitative computed tomography. Submitted, *J Foot Ankle Research.*

Abstracts and Conference Proceedings

1. **Gutekunst DJ** and DR Sinacore (2013). Neuropathic Charcot arthropathy is associated with reduced foot bone mineral density and bone geometric strength indices. Accepted for oral presentation, *APTA Combined Sections Meeting,* Jan 2013, San Diego, CA.
2. **Gutekunst DJ**; Bohnert KL; and DR Sinacore (2013). Buckling ratio, cortical thickness, and section modulus predict *ex vivo* failure loads in human metatarsals. Accepted for oral presentation, *APTA Combined Sections Meeting,* Jan 2013, San Diego, CA.
3. Sinacore DR; **Gutekunst DJ;** Bohnert KL; Mueller MJ; and MK Hastings (2013). Metatarsal buckling ratio as a fracture index in neuropathic (Charcot's) arthropathy. Accepted for oral presentation, *APTA Combined Sections Meeting,* Jan 2013, San Diego, CA.
4. **Gutekunst DJ;** Liu L; Ju T; Hastings MK; and DR Sinacore (2012). A novel CT-based approach for assessing deformity in the diabetic neuropathic foot. *Musculoskeletal Research Conference*, Washington University Department of Orthopaedics.

5. **Gutekunst DJ;** Commean PK; Smith KE; Prior FW; and DR Sinacore (2012). Neuropathic Charcot arthropathy is associated with reduced foot bone mineral density and bone geometric strength indices. *Musculoskeletal Research Conference,* Washington University Department of Orthopaedics.

6. **Gutekunst DJ;** Liu L; Ju T; Commean PK; Smith KE; Hastings MK; and DR Sinacore (2011). Anatomically relevant pedal bone orientation axes using quantitative computed tomography. *Proceedings of the International Society of Biomechanics*, Brussels, Belgium. ***Recipient of ISB Congress Travel Grant award.***

7. Seay JF; Frykman PN; and **DJ Gutekunst** (2011)**.** Constrained cadence marching leads to higher peak tibial accelerations. *Med Sci Sports Exercise* 43(5):s691-s692.

8. **Gutekunst DJ;** Liu L; Ju T; Commean PK; Smith KE; Hastings MK; and DR Sinacore (2010). Structural polymorphisms in midtarsal bone alignment lead to focal midfoot pressures. *Foot and Ankle International* 33(2):335. Presented at *International Foot and Ankle Biomechanics*, Seattle, WA.

9. **Gutekunst DJ;** Bohnert KL; Hastings MK; and DR Sinacore (2010). Cast-boot ankle-foot orthoses yield greater forefoot load reduction than total contact casts. *Proceedings of EMED Scientific Meeting*, Providence, RI, USA. ***Finalist for 2010 Novel "Art in Science" award.***

10. **Gutekunst DJ;** Frykman PN; and JF Seay (2010). Over-striding during "fixed cadence" load carriage leads to increased ground reaction forces. *Proceedings of the American Society of Biomechanics*, Providence, RI.

11. Seay JF; **Gutekunst DJ;** and PN Frykman (2010). Vertical ground reaction forces increase over time during 60 minutes of forced-cadence marching. *Proceedings of the American Society of Biomechanics*, Providence, RI.

12. Schiffman JM; Gregorczyk KN; Hasselquist L; Bensel CK; Obusek JP; **Gutekunst D;** and P Frykman (2010). Ergonomic evaluation of an exoskeleton prototype. *Proceedings of the 3rd International Conference on Applied Human Factors and Ergonomics*, Miami, FL.

13. **Gutekunst DJ;** Hastings MK; Bohnert KL; and DR Sinacore (2010). Off-loading with total contact casting compared to ankle-foot orthoses in individuals with diabetes-related plantar ulcers. *Combined Sections Meeting of the American Physical Therapy Association*, San Diego, CA.

14. **Gutekunst DJ;** Koleini M; Zou D; and RH Deusinger (2009). Inter- and Intra-Observer Variability of Marker Placement. *Proceedings of the Gait and Clinical Movement Analysis Society*, Denver, CO.

15. **Gutekunst DJ;** Harman EA; Frykman PN; and RP Mello (2007). Development of a treadmill-based military initial-entry fitness screening test. *Med Sci Sports Exercise*, 39(5), s202-s203.

16. Harman, EA; Frykman PN; **Gutekunst DJ;** Nindl BC; and JA Alemany (2007). Prediction of military physical performance from basic physical tests. *Med Sci Sports Exercise*, 39(5).

17. Frykman PN; Harman EA; **Gutekunst DJ;** Alemany JA; Nindl BC; and MA Sharp (2007). Predicting obstacle course performance from field expedient tests. *Med Sci Sports Exercise*, 39(5).

18. Gregorczyk K; Obusek JP; Hasselquist L; Schiffman J; Bensel C; **Gutekunst D;** and P Frykman (2006). The effects of a lower body exoskeleton load carriage assistive device on oxygen consumption and kinematics during walking with loads. *Army Science Conference,* Orlando.

19. Zambraski EJ; Frykman PN; **Gutekunst D;** and EA Harman (2006). Biomechanical and metabolic demands associated with load carriage and helmet supported devices. *Shoresh Biomedical Meeting*, Shoresh, Israel.

20. **Gutekunst DJ;** Frykman PN; Nindl BC; Rarick KR; Mello RP; and EA Harman (2006). Training-induced improvements in submaximal gait economy with and without a backpack/military load. *Med Sci Sports Exercise*, 38(5), s170.

21. Frykman PN; Harman EA; **Gutekunst DJ;** and BC Nindl (2006). Effects of U.S. Army standardized physical training and a weight training program on body composition. *Med Sci Sports Exercise*, 38(5), s272.

22. Harman EA; Frykman PN; **Gutekunst DJ;** Nindl BC; and J Alemany (2006). U.S. Army standardized physical training vs. a weightlifting-based program: effects on soldier physical performance. *Med Sci Sports Exercise*, 38(5), s272.

23. **Gutekunst DJ;** Harman EA; and PN Frykman (2005). Determinants of 2 mile (3.2 km) time with and without a 70 pound (32 kg) military load. *Med Sci Sports Exercise*, 37(5), s403.

24. Frykman PN; Harman EA; **Gutekunst DJ;** and BC Nindl (2005). Body-composition effects of the new U.S. Army standardized physical training program and a prototype training program that incorporates weightlifting. *International Congress on Soldiers' Physical Performance*, p. 86, Jyväskylä, Finland.

25. Harman EA; Frykman PN; **Gutekunst DJ;** and BC Nindl (2005). Physical performance effects of the new U.S. Army standardized physical training and an experimental program that incorporates weightlifting. *International Congress on Soldiers' Physical Performance*, p. 87, Jyväskylä, Finland.

26. **Gutekunst DJ;** SP Messier (2004). Association between weight change and knee joint kinetics during gait in overweight and obese older adults with knee osteoarthritis. *Med Sci Sports Exercise* 36(5): s234-5.

Honors and Awards

Dean's Special Recognition for Leadership, Washington University, 2011
Bridging GAPS award, Washington University, 2011
Congress Travel Grant, International Society of Biomechanics, 2011
Finalist, *Art in Science* award, Novel EMED Scientific Meeting, 2010
Graduate Fellowship, Wake Forest University, 2002-2004
Woodward Fellowship, Washington University, 1997-2001
National Merit Scholar, 1997

Professional Memberships

2003 – present	American College of Sports Medicine
2008 – present	Gait & Clinical Movement Analysis Society
2009 – present	American Society of Biomechanics
2010 – present	International Society of Biomechanics
2010 – present	International Foot & Ankle Biomechanics community

Professional and Academic Service

2005-present	Ad-Hoc Manuscript Reviewer, Medicine & Science in Sports & Exercise
2009-present	Reviewer, Conference Proceedings, Gait & Clinical Movement Analysis Society
2010-present	External Scientific Reviewer, U.S. Army Natick Research, Development, and Engineering Center
2011-present	Ad-Hoc Manuscript Reviewer, Medical & Biological Engineering & Computing
2008-2010	Departmental Senator, Graduate Student Senate, Washington University
2010-2011	President, Graduate Student Senate, Washington University
2011	Chair, Graduate Research Symposium, Washington University

Teaching Experience:

Washington University
Kinesiology I – Kinesiomechanics (PT606): Fall semester, 2008, 2009, 2010, 2011
- Prepared and presented lectures on statics, anthropometrics, inverse dynamics, and motion capture

Wake Forest University
Biomechanics (HES 375): Fall 2003
- Teaching Assistant for undergraduate course on human movement and orthopedic biomechanics
- Led laboratory activities, including semester capstone projects using 2-D motion capture.

Advanced Biomechanics (HES 675): Fall 2003
- Laboratory Assistant for first-year graduate course in orthopaedic biomechanics; units included strength assessment, 3-D motion capture, and inverse dynamics.